ABSTRACTS DEL 6° MEETING
DEL CAPITOLO ITALIANO
DELLA EUROPEAN SOCIETY OF BIOMECHANICS

ESB-ITA 2016

NAPOLI, 22 GIUGNO 2016

ORGANIZZATO CONGIUNTAMENTE AL
V CONGRESSO DEL GRUPPO NAZIONALE DI BIOINGEGNERIA (GNB)

Indice

pag.

Numerical comparison of fatigue criteria for NiTi cardiovascular devices

D. Allegretti[1], L. Petrini[2], W. Wu[1], F. Miliavacca[1] and G. Pennati[1]
[1] *Laboratory of Biological Structure Mechanics, Dept. CMIC 'Giulio Natta', Politecnico di Milano, Italy*
[2] *Department of Civil and Environmental Engineering, Politecnico di Milano, Italy*

***Abstract*—NiTi devices are widely used in biomedical fields due to the material flexibility and ability to recovery high strains. However the fatigue behaviour of these devices is still undermined by failure. The particular biomechanical operating environment is characterized by multi-axial cyclic loading transferred to the implanted device. The computational finite elements analysis is a power tool to investigate the state of load imposed from point to point in the devices, but the numerical results have to be correctly analyzed. In this work the fatigue performance of different geometries have been numerically studied and analyzed with different fatigue criteria. The comparison of the results allowed to highlight similarities and differences of the studied approaches and to get some hints for the selection of the most suitable criteria for NiTi cardiovascular devices.**

***Keywords*— Nitinol, stent, peripheral, fatigue.**

I. Introduction

Nickel-Titanium alloys (NiTi) are widely used in biomedical fields. In particular, several cardiovascular minimally-invasive devices exploit NiTi pseudo-elastic behavior. Notwithstanding the high performance of NiTi peripheral stents or cardiovascular valves, due to the material flexibility and ability of recovery high strains, the fatigue behavior is still an open issue[1]. Stents and valve implantation foresees a first step of device crimping, then a partial recovery of the original shape during self-expansion in the site to be treated and finally cyclic loading due to leg or heart movements that may induce multi-axial solicitations [2]. During these three phases, the material response greatly varies from point to point due to the complex geometry of the devices [3]. Accordingly, the material is subjected to elastic cycles in austenitic phase in some zones, while it is partially transformed in martensite in other zones where it may cycle elastically from the lower plateau to the upper one or vice versa. Finally plasticization of martensitic phase may be reached in other areas. Considering also that the interaction of mean and alternate strains on the NiTi fatigue life does not follow the Goodman relation and it is strongly dependent from the specimen production process, it is clear that the prediction of cardiovascular device fatigue resistance is not an easy task. In this work, we numerically analyzed the fatigue performance of two geometries under multiaxial loads using different fatigue criteria.

II. Materials and Methods

Physiological loads acting on NiTi stents may induce axial, bending and torsional cyclic solicitations. Accordingly, fatigue analysis requires criteria able to take into account multiaxial load conditions. In order to compare failure prediction of few multiaxial criteria proposed in the literature, two different geometries and different loading conditions were considered by finite element analyses. A V-shape geometry, resembling the basic element constituting a stent, was used to have a quick and useful view on the performance of the different criteria. Moreover, a stent geometries composed by 6 rings, reproducing a commercial stent (Maris Plus), was analysed to capture in more detail the influence of the complexity of the device geometry on the fatigue behaviour. Maximum and minimum displacement (L) and angle (A) were applied to get the load ratio R = $L_{min}/L_{max}=A_{min}/A_{max}$ equal to 0, -1 and >0 (Fig.1). The corresponding alterante and mean component $\Delta L/A_a = \frac{L/A_{max}-L/A_{min}}{2}; \Delta L/A_m = \frac{L/A_{max}+L/A_{min}}{2}$ considered are reported in Table 1 for the two geometries.

TABLE I
Loading applied in the analysis

	mm | Degree	*V-Shape*	*Stent*
R=0	ΔL_m	10	15
	ΔL_a	10	15
	ΔA_m	/	30°
	ΔA_a	/	30°
R=-1	ΔL_m	0	0
	ΔL_a	15	2,5
	ΔA_m	/	0°
	ΔA_a	/	15°
R>0	ΔL_m	17.5	25
	ΔL_a	2.5	5
	ΔA_m	/	45°
	ΔA_a	/	15°

Different loading conditions imposed in the analysis. The displacement [ΔL] is given in mm, the angle [ΔA] in degree.

In this work 5 different fatigue criteria have been compared: Coffin-Manson (Δε1), Tresca strain (Tresca), Smith-Watson-Trooper (SWT), Brown Miller (BM), Fatemi-Socie (FS).

For each analysis, the results obtained through the different criteria have been compared in terms of the location of the critical nodes in the geometry and the critical nodes damage parameter values.

III. Results

A. V-shape geometry

The results of the different analyses performed on the V-shape geometry indicate that the most critical zone is the peak of the V. The difference between criteria results is in the position of the most critical nodes of the inner zone of the

peak. An example of the results for the load ratio R>0 are reported in figure 2. For each criterion the 5 most critical nodes have been considered: they are reported in Table 2 by the node number and distinguishing the location with respect to the geometry by colour, point positioned at the left of the peak are in black, at the center are in green and the right side are in red.

TABLE II
V-Shape – R>0

Tresca	*BM*	*FS*	*SWT*	Δε1
23093	*23202*	*24510*	24619	23202
24728	*24619*	*24401*	24510	24619
23202	*23093*	*24506*	24401	23093
24619	*24728*	*24619*	24728	24728
22984	*23311*	*24292*	24292	23311

Most critical nodes for each fatigue criteria used in the analysis of the V-shape geometry.

B. Stent geometry

The results of the different analysis performed on the stent geometry have been studied with the 5 different fatigue criteria. An example of the results for the load ratio R>0 are reported in the table 3 and in figure 3. The critical nodes are grouped in five main critical zones. For each criterion the 5 most critical nodes have been considered (Fig.3): they are reported in Table 3 by the node number and distinguishing the critical zones with respect to the geometry by colour.

TABLE II
Stent – R>0

Tresca	*BM*	*FS*	*SWT*	Δε1
111171	*113547*	*111171*	112359	113547
111172	*111172*	*111163*	112360	111172
111163	*113548*	*111172*	112351	113548
107275	*111171*	*111164*	107275	111171
107276	*113539*	*111170*	112362	113539

Most critical nodes for each fatigue criteria used in the analysis of the stent geometry.

IV. CONCLUSION

The comparison of the results allowed to highlight similarities and differences of the studied approaches and to get some hints for the selection of the most suitable criteria for NiTi cardiovascular devices. Finally, the influence of plasticity on the fatigue response was numerically investigated.

These analyses represent a preliminary study and a future development is the comparison of the presented results with planned ad-hoc experimental fatigue tests to validate the predictions.

REFERENCES

[1] Scheinert, D., S. Scheinert, J. Sax, C. Piorkowski, S. Braunlich, M. Ulrich, G. Biamino and A. Schmidt. Prevalence and clinical impact of stent fractures after femoropopliteal stenting. J. Am. Coll. Cardiol. 45(2):312-315, 2005.

[2] Ansari, F., L. Pack, S. Brooks and T. Morrison. Design considerations for studies of the biomechanical environment of the femoropopliteal arteries. J. Vasc. Surg. 58:804-813, 2013.

[3] Meoli, A., E. Dordoni, L. Petrini, F. Migliavacca, G. Dubini and G. Pennati. Computational study of axial fatigue for peripheral Nitinol stens. J. Mater. Eng. Perform. 23:2606-2613, 2014.

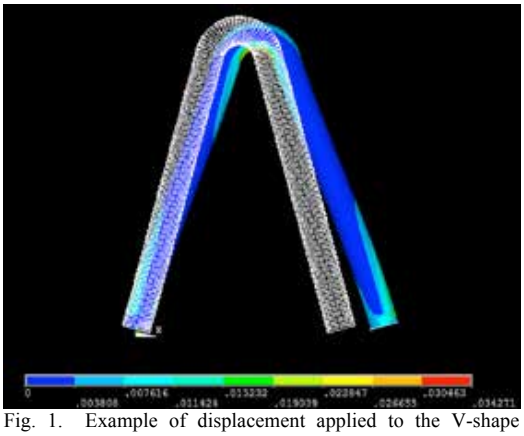

Fig. 1. Example of displacement applied to the V-shape geometry. The deformed (colour map image) and the underformed shapes (dashed image) are reported.

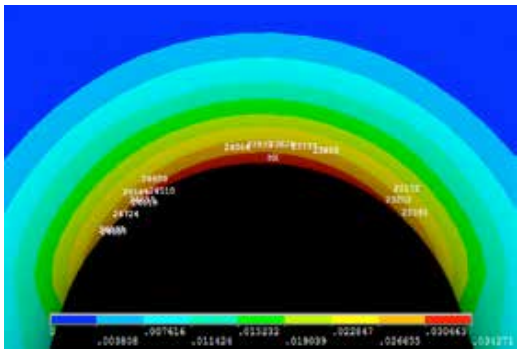

Fig. 2. Results of the V-shape geometry for the load ratio R>0. The inner zone of the peak are highlighted. The most critical nodes resulted by the analysis done with the different fatigue criteria are reported.

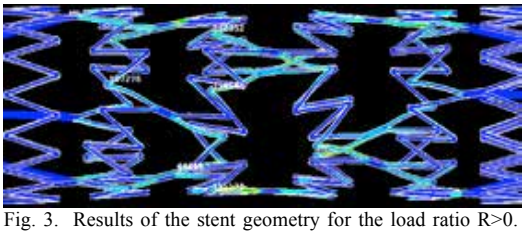

Fig. 3. Results of the stent geometry for the load ratio R>0. The most critical nodes resulted with the different fatigue criteria are highlighted.

Comparison of mechanical properties of neat, decellularized and coated thacheal tissues

S. Montesanto, O. Fici, M. Cammarata, V. Brucato, V. La Carrubba, G. Baratta, and M. Zingales
[1] *Department of Civil, Environmental, Aerospace, Materials Engineering (DICAM)- University of Palermo, Viale delle Scienze Ed. 8, 90128 Palermo, Italy*

***Abstract*— Tracheal tissue is a complex multi-layer structure. Accurate information on its mechanical properties are essential for a reliable prediction of tracheal deformation, which has a significant clinic relevance. The use of a decellularized trachea does not ensure stable mechanical properties of the construct. A coating process with a porous synthetic membrane based on PLLA allowed a precise control of the mechanical proprieties.**

***Keywords*—Decellularization, mechanical proprieties, hybrid tissues, tracheal tissue.**

I. Introduction

Decellularized tissues and organs have been successfully used in a variety of tissue engineering/regenerative medicine applications, and the decellularization methods used vary as widely as the tissues and organs of interest [1]. The efficiency of cell removal from a tissue is dependent on the origin of the tissue and the specific physical, chemical, and enzymatic methods that are used. Each of these treatments affect the biochemical composition, tissue ultrastructure, and mechanical behaviour of the remaining extracellular matrix (ECM) scaffold, which in turn, affect the host response to the material [2]. Tracheal tissue is a multi-layer structure composed of cartilage, trachealis muscle, mucosa, submucosa membrane and adventitial membrane. An accurate knowledge of its mechanical properties is essential for a reliable prediction of tracheal deformation, which has a significant clinic relevance [3, 4].

The use of a decellularized trachea (natural scaffold), as a matter of fact, dose not ensure stable mechanical properties of the construct, does not guarantee a reproducibility of the internal and external structure and, eventually, does not allow a precise control of its biodegradation kinetics.

In this work, a coating process with a porous synthetic membrane via a combination of Dip-coating and Diffusion Induced Phase Separation (DIPS) was designed and carried out. Experimental results show that coating with the synthetic material helps to recover the mechanical properties lost, owing to decellularization of porcine trachea rings [5].

II. Materials and Methods

The porcine trachea used in this study were supplied from Villabate slaughterhouse.

A. Decellularization methods

Sodium Dodecyl Sulfate (SDS) was used as detergent for the decellularization. The porcine trachea was soaked into SDS bath for 24 h at room temperature. THereafter, the sample was maintained in a box containing PBS 1X at 4°C until it was analysed.

B. Tracheal tissue coating

Dip coating consists in the immersion of a biological tissue in a PLLA-dioxane viscous solution (with 8% wt/wt of dioxane) with subsequent extraction at a controlled constant rate. Via this technique it is possible to control the thickness of the coating layer by varying tissue extraction rate, solution temperature and polymer concentration (see fig. 1).

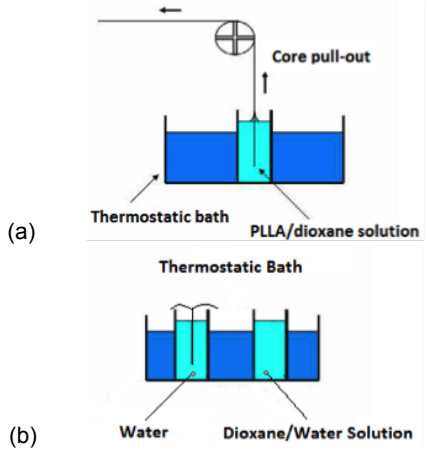

Fig. 1. Schematic of the Dip-coating (a) and DIPS (b) processes.

The subsequent pool immersion of the tissue, covered by a continuous layer of a viscous polymer solution, into a coagulation bath, represents the Diffusion Induced Phase Separation (DIPS) step.

The bath contains pure water. Via DIPS, the simultaneous solvent (dioxane) diffusion out of the polymeric film and counterdiffusion of the nonsolvent (water) from the coagulation bath towards the polymeric film will induce the phase separation process. Fig. 1 reports a schematic of the two processes. In this study, extraction rate, polymer solution concentration and process temperature were taken constant in all experiments: the extraction velocity was set to 3cm/min, the polymer solution concentration to 8 wt% PLLA and the temperature to 30 °C [6].

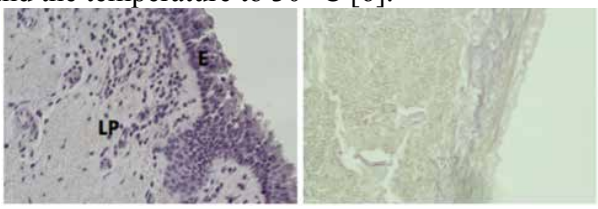

Fig. 2. Comparison between a native tissue (right side) and a decellularized tissue (lef side).

C. Mechanical characterization

Tensile tests were performed to investigate the mechanical behaviour of trachea rings obtained using porcine tracheas. A force speed of 0.1 g/s was set, while the temperature was taken constant at the value of 30°C. Bose biaxial instrument was utilized in uniaxial mode to determine the stress/strain behaviour.

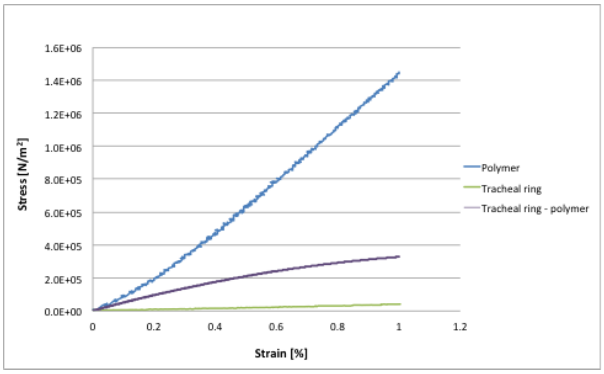

Fig. 3. Comparison of tensile mechanical properties of polymer, hybrid tissue and tracheal ring.

III. Results and Discussion

A. Tissue decellularizzation

SDS is very effective in removal of cellular components from tissue (see figure 2). On the other hand, however, it tends to disrupt the native tissue structure, and it causes a partial loss of tissue integrity. However, it does not appear that SDS severely removes collagen and/or cartilage from the tissue.

B. Tensile behaviour

By coupling dip coating and DIPS it is possible to produce a 3D biohybrid synthetic/natural scaffold able to guarantee enhancement of the mechanical properties lost during decellularization of the native tissue.

Mechanical tensile tests on the native trachea, ofn the neat polymeric film and on the bioengineered (hybrid) tissue are reported in fig. 3, to show the recovery of the mechanical properties attained via coating with PLLA. The improvement of the mechanical performance is evident up to strains as high as 1%, comparable with the physiological deformations of the examined tissue.

IV. Conclusions

A biohybrid material has been prepared via coating of a decellularization tracheal tissue with a PLLA membrane. Mechanical preliminary tests show that the biohybrid material exhibit performances similar to those of native tracheal tissue, thus allowing one to recover the property loss due to the decellurarization protocol.

Acknowledgement

This study has been supported by the Italian Ministry of University and Research (PRIN 2010–2011 - prot. 20109PLMH2_008). The experimental facility at the BNM2- LAB of the CHAB Center of Palermo University is gratefully appreciated.

References

[1] T.W. Gilbert, T.L. Sellaro, S.F. Badylak, “Decellularization of tissues and organs,” *Biomaterials*, vol.27, pp.3675-3683, 2006.

[2] R.W. Grauss, M.G. Hazekamp, F. Oppenhuizen, C.J. van Munsteren, A.C. Gittenbergerde Groot, M.C. DeRuiter, “Histological evaluation of decellularised porcine aortic valves: matrix changes due to different decellularisation methods”, *Eur J Cardiothorac Surg*, vol. 27, pp. 566-571, 2005.

[3] R.B. Hirschi, R. Tooley, A. Parent, K. Johnson, R.H. Bartlett, “Evaluation of gas exchange, pulmonary compliance, and lung injury during total and partial liquid ventilation in the acute respiratory distress syndrome”, *Crit. Care Med*., vol. 24 pp. 1001-1008, 1996.

[4] O. Trabelsi, A.P. del Palomar, J.L. Lopez-Villalobos, A. Ginel, M. Doblare, “Experimental characterization and constitutive modeling of the mechanical behavior of the human trachea”, *Medical Engineering and Physics*, vol. 32 pp.76–82, 2010.

[5] Patent Application No. 102016000033555 filed 01/04/2016

[6] S. Montesanto, G.A. Mannella, F. Carfì Pavia, V. La Carrubba, V. Brucato, “Coagulation bath composition and desiccation environments tuning parameters to prepare skinless membranes via diffusion induced phase separation,“ *J. Appl. Polym. Sci.,* vol. 132, 2015.

Multiscale computational modeling of aortic mechanics via a patient-specific strategy

D. Bianchi[1], M. Marino[2], and G. Vairo[1]
[1] *University of Rome "Tor Vergata"- Department of Civil Engineering & Computer Science (DICII), Via del Politecnico 1, 00133 Rome - Italy, e-mail: d.bianchi@ing.uniroma2.it, vairo@ing.uniroma2.it ;*
[2] *Leibniz Universität Hannover - Institut für Kontinuumsmechanik, Appelstr. 11, 30167 Hannover - Germany, e-mail: marino@ikm.uni-hannover.de*

***Abstract*—A novel computational approach for analysing the mechanical response of aortic segments accounting for patient-specific data is proposed. A parametric tool, suitable for parametric biomechanical analyses, is developed by integrating: (i) segmentation techniques to define the geometry from aortic patient-specific CT images; (ii) multiscale homogenization techniques to describe the non-linear mechanics of biological tissues, as depending on micro- and nano-structural parameters obtained from histological and biochemical data; (iii) a non-linear finite-element formulation of the equilibrium problem. The proposed model has been applied for reproducing an inflation test on aortic segments. Moreover, the influence on aortic macroscale response of a localized defect affecting the crimp of collagen fibers is analyzed, proving that the adopted multiscale structural approach is able to investigate the etiology of cardiovascular diseases and physio-pathological remodelling mechanisms.**

***Keywords*—Aortic mechanics, patient-specific computational models, Multiscale tissue modelling, Non-linear finite element formulation, Cardiovascular diseases.**

I. Introduction

CARDIOVASCULAR diseases (CVDs) are the leading cause of death worldwide but their etiology is debated and the therapeutic approaches are still based on the definition of risk parameters mainly evaluated on the own experience of clinicians. In this framework, computational models have recently provided novel insights into aortic biomechanics, in both health and disease scenario [1],[2]. Although several reliable methods exist for reconstructing the geometry of computational domains from patient-based CT (computed tomography) images, a key aspect for accurate analyses is represented by the constitutive description of the tissue, characterized by anisotropic and non-linear mechanical response. Many constitutive formulations are available in literature [3],[4], but they generally have weak relation with histological/biochemical parameters. On the other hand, a multiscale structurally-motivated approach for tissue constitutive description has been recently proposed by some of the authors and has been proved, referring to simple study cases only, to be effective to reproduce tissue behaviour, by introducing parameters that straight describe histological and biochemical properties [5]-[9]. In order to allow the use of this refined constitutive description, that has never been employed in numerical simulations reproducing complex patient-specific geometries, a fully-personalized clinical application integrating a computational strategy for non-linear finite-element (FE) analyses of aortic segments is herein presented. In detail, patient-specific geometrical modeling is coupled with the aforementioned multiscale structural constitutive formulation, resulting in an overall 3D macroscale description explicitly depending on dominant micro- and nano-scale personalized features. The preliminary case study of a thoracic aortic segment undergoing an inflation test is numerically addressed, comparing different constitutive strategies and proving the capability of the proposed integrated computational approach to analyze the influence of possible localized tissue defects on aortic biomechanics.

II. Materials and Methods

A general methodology for developing 3D-FE models of blood vessels incorporating patient-specific geometry from computer tomography (CT) images and histological, biochemical and biophysical data is herein described. The corresponding schematic is represented in Fig. 1.

A. Constitutive description

In the framework of a multiscale strategy and referring to the tunica media only, the multi-layered histologic structure of the aortic tissue, constituted by the occurrence of media lamellar units (MLUs), is modelled as a layered structure comprising N perfectly-bonded layers characterized by the same thickness. Each MLU is composed by an elastin layer (EL) of thickness h_{EL} and an interlamellar substance (IL) of thickness h_{IL}. In turn, the interlamellar substance has a multi-layered sub-structure made up of concentrically fiber-reinforced sub-layers, comprising elastin, muscle cells, and crimped collagenous fibers whose main direction is helically arranged around the vessel axis. The orientation of collagen fibers with respect to the vessel axis is described by the wrapping angle ϑ_F, varying along the vessel thickness. Each IL sub-layer is here modelled as a composite material made up of crimped collagen fibers, taken aligned in the same direction, embedded in a linearly elastic isotropic matrix, describing both the elastin network and the muscle cells, having comparable stiffness [10]. Collagen fibres in soft tissues are bundles of densely packed tilted fibrils, laterally linked by means of proteoglycans. In turn, collagen fibrils are made up of staggered arrays of tropocollagen molecules, mutually interconnected by intermolecular covalent cross-links. Both micro-scale and nano-scale features of collagen fibers are accounted for, via a multiscale homogenization process [5]-[9].

B. Vessel geometry

The reference vessel configuration Γ_o is reconstructed from 3D contrast-enhanced CT images (Fig. 1). Such images

describe, with a sub-millimetric resolution, the anatomy of blood vessels through 3D arrays of grayscale intensities, and they contain body projection over coronal, sagittal and axial planes. By employing a region- based model which involves the Geodesic Active Contours algorithm [11], an image segmentation process is applied, providing a description of the aortic geometry via a surface mesh. Segmentation errors, due to possible coarse resolution of medical devices and/or involuntary patient movements, are reduced by applying a Taubin smoothing algorithm [12]. Finally, curves resulting from the intersection of the smoothed surface mesh with a family of planes orthogonal to the mean vessel axis are employed for generating the loft surface Γ_o used for FE simulations.

C. Numerical model

The surface of the aortic segment, resulting from the geometric reconstruction, is treated as a Mindlin-Reissner shell. In order to avoid locking phenomena related with both shell formulation and tissue incompressibility, a mixed displacement-pressure finite-element formulation is employed, by considering a MITC shell element [13]. In detail, shell surface is discretized by means of iso-parametric 6-nodes 2D-triangular elements with quadratic (resp., linear) shape functions for displacements and rotations (resp., for pressure). In agreement with a computational homogenization strategy, a material map is computed on the basis of the homogenization procedure previously recalled. By employing an updated-Lagrangian strategy, both geometric and material non-linearities are treated via an incremental approach, by solving a series of incremental linearly-elastic sub-problems, and thereby allowing for a step-by-step updating of: (i) geometry; (ii) reference coordinate system; (iii) material properties. Figure 2 gives a schematic representation of the implemented solution algorithm.

III. Results

As a case study, a thoracic aortic segment subjected to an inflation test up to 180 mmHg is numerically addressed. Numerical results are obtained by adopting the above introduced multiscale homogenization procedure and by describing histochemical properties as referred to a homogeneous distribution into the aortic domain (homogeneous non-linear model, HNM) and to a localized defect (defect non-linear model, DNM). In the latter case, values of model parameters coincide with the HNM's ones with the exception of an higher initial collagen fiber amplitude in a region located below the middle section of the aortic segment (Fig. 1). Figure 3 shows that the localized defect of collagen fiber crimp in the DNM case induces significant differences in the macroscopic strain field of the overall aortic domain with respect to the HNM case.

IV. Conclusions

The mechanical response of aortic segments has been addressed by proposing a novel integrated computational approach able to describe, in a general patient-specific framework, both aortic geometry and material properties. A geometric reconstruction procedure from 3D computer-tomography images has been coupled with a multiscale non-linear constitutive description, accounting for highly-personalized histological and biochemical features. In detail, a multi-step homogenization approach based on a bottom-up strategy (from the nano-up to the macroscale) has been employed for describing the non-linear and anisotropic response of aortic tissues. Dominant nano- and micro scale mechanisms have been consistently up-scaled following a structurally-motivated multiscale strategy, which allows to couple in a non-phenomenological scheme the tissue macroscale mechanics with both histological subscale arrangement and biochemical environment.

Acknowledgement

Present research study was partially supported by Italian Minister of University and Research, MIUR (PRIN, Grant number F11J12000210001). M. Marino gratefully acknowledges a post-doctoral fellowship from the Alexander von Humboldt Foundation.

References

[1] F. Auricchio, M. Conti, S. Morganti, A. Reali, 2013, Patient-specific finite element analysis of carotid artery stenting: a focus on vessel modeling. *Int. J. Numer. Methods Biomed. Eng.* 29, p.p. 645–664

[2] D.Roy, G. Holzapfel, C. Kauffmann, G. Soulez, 2014, Finite element analysis of abdominal aortic aneurysms: geometrical and structural reconstruction with application of an anisotropic material model. *IMA J. Appl. Math*. 79, p.p. 1011–1026.

[3] G. Holzapfel, T. Gasser, R. Ogden, 2000, A new constitutive framework for arterial wall mechanics and a comparative study of material models. *J. Elast.*, 61, p.p. 1–48.

[4] F. Auricchio, A. Ferrara, S. Morganti, 2012, Comparison and critical analysis of invariant-based models with respect to their ability in fitting human aortic valve data. *Ann. Solids Struct. Mech.*, 4, p.p. 1–14.

[5] F. Maceri, M. Marino, and G. Vairo, 2010, A unified multiscale mechanical model for soft collagenous tissues with regular fiber arrangement, *J. Biomech.*, 43 pp. 355-363,.

[6] F. Maceri, M. Marino, and G. Vairo, 2012, Elasto-damage modeling of biopolymer molecules response, *Comput. Model. Eng. Sci.*, 87, pp. 461-481.

[7] F. Maceri, M. Marino, and G. Vairo, 2013, Age-Dependent Arterial Mechanics via a Multiscale Elastic Approach, *Int. J. Comput. Methods Eng. Sci. Mech.*, 14, p.p. 141-151.

[8] M. Marino, and G. Vairo, 2014, Stress and strain localization in stretched collagenous tissues via a multiscale modelling approach, *Comput. Methods Biomech. Biomed. Engin.*, 17, p.p. 11-30.

[9] M. Marino, G., Vairo, 2013,Multiscale elastic models of collagen bio-structures: from cross-linked molecules to soft tissues. A., Gefen (Ed.), *Studies in Mechanobiology, Tissue Engineering and Biomaterials*, vol.14, Springer, Berlin, Germany, p.p. 73–102.

[10] M.A. Zulliger, A. Rachev, N. Stergiopulos, 2004, A constitutive formulation of arterial mechanics including vascular smooth muscle tone, *Am. J. Physiol. Heart Circ. Physiol.*, 287, p.p. 1335-1343.

[11] V. Caselles, F. Catte, T. Colle and F. Dibos, 1993, A geometric model for active contour , *Numer. Math.*, 66, p.p. 1-31.

[12] G. Taubin, 1994,Curve and surface smoothing without shrinkage, Technical Report, RC-19563, IBM-Research.

[13] D. Chapelle and K.J. Bathe, 2003, *The Finite Element Analysis of Shells Fundamentals.* Springer Berlin Heidelberg, (2003).

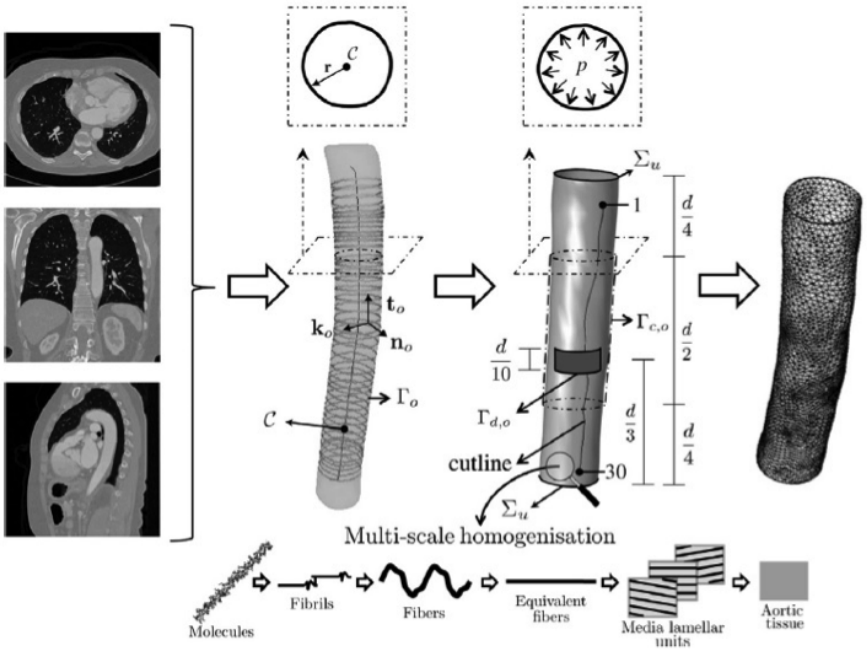

Fig. 1 Patient-specific aortic models. From left to right: CT images; geometric reconstruction; numerical model integrated with a multiscale homogenization approach to describe the tissue mechanical behavior; computational mesh.

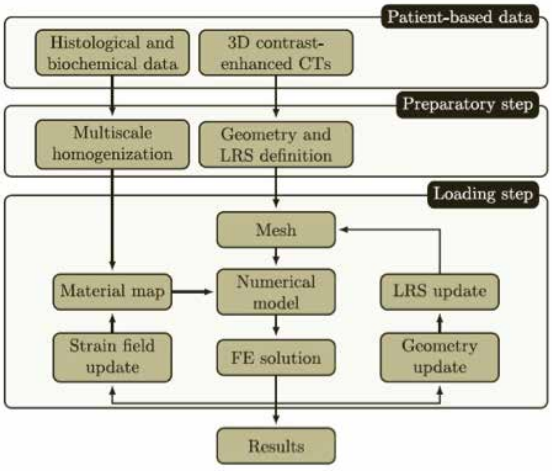

Fig. 2 Flowchart of the implemented solution algorithm. CT: computer tomography; LRS: local reference system; FE: finite element.

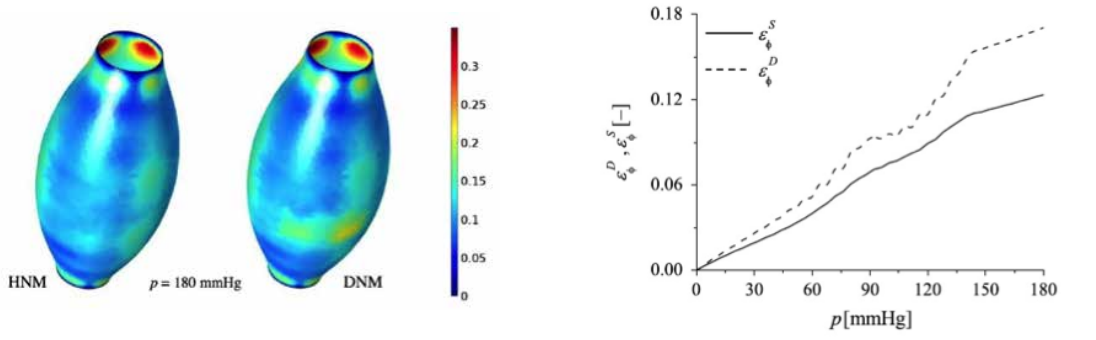

Fig. 3 (left) Distribution of the circumferential strain ε_ϕ at p = 180 [mmHg] in HNM and DNM cases. (right) Average circumferential strain vs. the pressure p in the defect zone (ε_ϕ^D) and in the surrounding tissue (ε_ϕ^S) for the DNM case.

Enzymatically Stiffenable Gelatin Hydrogels for Engineering Pathophysiological Organ Models

L. Cacopardo[1], G. Mattei[1] and A. Ahluwalia[1]
[1] *Research Centre 'Enrico Piaggio', University of Pisa (Italy)*

***Abstract*—Developing cell culture substrates that mimic the mechanical properties of the native cellular micro-environment is critical to engineer physiologically relevant in-vitro organ models. Moreover, considering that tissue ageing and fibrotic processes are generally associated with an extracellular matrix (ECM) stiffening, cell culture substrates capable of reproducing this healthy-to-aged/fibrotic transition in-vitro are fundamental for the realization of pathophysiologically relevant organ models. Here, we present transglutaminase-gelatin hydrogels with stiffenable properties as cell culture substrates for engineering tissue ageing or fibrotic models in-vitro.**

***Keywords*—nano-indentation, gelatin, transglutaminase, hydrogels, fibrotic models, in-vitro organ models.**

I. Introduction

The classical tissue engineering approach based on the successful interaction between cell, scaffold and bioreactor, represents an attractive strategy for the development of in-vitro organ models [1]. An ideal scaffold should mimic most of the properties of the native extracellular matrix (ECM) to provide cells with an appropriate microenvironment promoting their growth, differentiation and function. Among the ECM cues, biomechanical properties play a critical role in regulating pathophysiological cell behaviour and directing the development of tissue fibrosis, which is generally associated with an enzyme-mediated ECM hardening [2]. Tissue ageing is also associated with ECM hardening. For example, ageing in the cardiovascular system is characterized by an enhanced collagen and calcium deposition in the ECM and an increased protein cross-linking [3], while fibrosis may be observed in hepatic or pulmonary tissue affected by hepatitis [4] or lung disorders [5], respectively.

Based on the hypothesis that tissue stiffness increases as ageing/fibrosis progresses, dynamic scaffolds that mimic the elasticity of healthy and aged/diseased tissue ECM in-vitro need to be engineered to temporally manipulate their mechanical properties on demand [6].

Gelatin (a commercially available biomaterial derived from collagen) is often used as the organic component of scaffolds because of its biocompatibility [7]. However, due to its rapid degradation in typical cell culture environments (T = 37 °C), gelatin-based scaffolds are often covalently crosslinked using various chemical reagents (e.g. glutaraldehyde, formaldehyde [7]) or enzymes (e.g. transglutaminase [8]) to improve their stability and enhance the mechanical properties. In particular, transglutaminase is a calcium-independent enzyme that catalyses the formation of covalent cross-links between glutamine and lysine residues in proteins. Since it is commonly used in food manufacturing processes approved for human consumption by the U.S. Food and Drug Administration, this enzyme seems to be a promising cross-linking agent with respect to glutaraldehyde and formaldehyde, that may reduce gelatin biocompatibility if not completely washed out prior to cell seeding, and cannot be used in presence of cells.

Here we present the use of microbial transglutaminase (mTG) as a biocompatible second step enzymatic crosslinker for gelatin hydrogels to engineer pathophysiological in-vitro models that can be dynamically stiffened during cell culture from healthy towards aged/fibrotic environments at a user-defined time.

II. Materials and Method

A. Hydrogel Preparation

Since we are interested in characterizing mTG-mediated hardening at 37 °C (physiological temperature), gelatin hydrogels need to be stabilized via pre-crosslinking. Two series of pre-crosslinked mTG-gelatin samples were obtained adding 1 and 10 units of mTG (Activa WM, kindly gifted by Ajinomoto) per gram of gelatin to 5% w/v Type A gelatine solution (G2500, Sigma-Aldrich). The latter was then cast into custom cylindrical moulds (13 mm diameter – 8 mm height) and incubated at 37 °C (Day -1), obtaining 1 and 10 unit/gram (U/g) mTG-gelatin samples, respectively.

After 24h (Day 0), the hydrogels were carefully removed from the moulds and each sample was placed in different wells of a 12-well plate. Here, the hydrogels were submerged in 5 mL of mTG solutions at different concentrations (prepared in 1x phosphate buffered saline, PBS) to exogenously provide 10 and 100 units of mTG per gram of gelatin to crosslink (U/g). Finally, samples were incubated at 37 °C to be stiffened towards aged/fibrotic models. Samples immersed in 1x PBS (i.e. provided with no exogenous mTG or 0 U/g mTG) were used as controls.

B. Mechanical Testing

Nano-indentation tests were performed using a PIUMA Nanoindenter (Optics11) with a 61.5 μm spherical tip. Each hydrogel was glued on a Petri dish using cyanoacrylate (Attack, Loctite) and submerged with deionized water before testing. At least 10 indentations were performed on different surface points of each sample, using a constant strain rate of $\dot{\varepsilon} = 0.05\ s^{-1}$. Hydrogels were tested at day 1 and 7 after incubation in mTG solution. Experimental data were analysed with the nanoepsilon dot method, deriving elastic moduli as the stress-strain slope within 0.10 strain [9].

C. Statistical Analysis

Statistical analyses were performed with GraphPad Prism (Graph Pad Software Inc.). Data obtained for 1 and 10 U/g mTG-gelatin hydrogels were analysed separately with a 2-way ANOVA to investigate the effect of both exogenous mTG concentration and incubation time on the elastic modulus of each group of samples. Multiple comparisons were performed with Sidak test, in order to investigate either the effect of incubation time on resultant E for each exogenous mTG concentration or the effect of mTG concentration at the same time point. Statistical significance was set to $p < 0.05$.

III. Results

Figure 1A shows mTG-gelatin hydrogels removed from the moulds (day 0): 10 U/g hydrogels appear opaque and more stiff with respect to 1 U/g ones that are transparent and soft.

After 24 h of incubation in mTG, the elastic modulus (E) of 1 U/g gels significantly increases with exogenous mTG concentration (Fig. 2). Although higher in controls with no mTG (0 U/g), as expected, at 24 h the modulus of 10 U/g samples immersed in mTG solution is generally lower than that of 1 U/g gels and reaches a plateau at 10 U/g mTG.

The differences measured via nanoindentation are also appreciable in Fig. 1. At day 1 (Fig. 1B), control samples appear softer with respect to day 0 (Fig. 1A), while the other gels tend to shrink and become more opaque with increasing exogenous mTG concentration. On the contrary, differences are less evident in 10 U/g gels, except for the control that seems to be less shrunk and opaque than those exposed to 10 and 100 U/g exogenous mTG.

After 7 days of incubation, the E continues to increase significantly for both 1 and 10 U/g samples immersed in both 10 and 100 U/g mTG solutions with respect to 24 h (Fig. 3A-B), while it decreases in case of controls ($p < 0.05$ only in case of 10 U/g gels), suggesting that hydrolysis prevails over the enzymatic crosslinking.

The interaction between the two factors (i.e. exogenous mTG and incubation time) was significant for both 1 and 10 U/g pre-crosslinked samples, with incubation time effect depending on the level of mTG concentration. In particular, the elastic modulus increases with time only in presence of mTG, while it decreases between day 1 and day 7 in absence of the enzyme (Fig. 3A-B). Moreover, the E increases increasing the exogenous mTG concentration ($p < 0.05$ only in the case of 10 U/g gels at day 7, between 10U/g and 100U/g exogenous concentrations).

IV. Conclusion

Pathophysiological in-vitro models are important to understand the processes underneath aging and several diseases, such as fibrosis. Given the critical role of the biomechanical environment in regulating cell behaviour and directing the development of tissue fibrosis, mTG-gelatin hydrogels were designed to reproduce the typical stiffness of healthy soft tissues and to subsequently be stiffenable via enzymatic activity to recreate aged or fibrotic environments, in an in-vivo like manner.

We demonstrate that mTG can be used as a second step crosslinker to increase the elastic modulus of gelatin substrates, thus reproducing the transition from healthy to aged/fibrotic environments in-vitro. Microbial transglutaminase is an attractive biocompatible agent [8] for altering the mechanical properties of amino-containing scaffolds during cell culture to engineer fibrotic/aged organ models in-vitro.

Thanks to exogenous mTG administration, the elastic modulus of 1 U/g samples can be varied from about 4 to70 kPa. These values cover the range of typical pathophysiological elastic moduli of soft tissues [10].

References

[1] Mattei G., Giusti S., Ahluwalia A., 'Design Criteria for Generating Physiologically Relevant In Vitro Models in Bioreactors'. *Processes* 2:548-69, 2014.

[2] Frantz C., Stewart KM and Weaver VM. 'The extracellular matrix at a glance'. *Journal of Cell Science*, 123:4195-200, 2010.

[3] Wu M., Fannin J., Rice K. M., Wang B. and Blough E. R. 'Effect of aging on cellular mechanotransduction'. *Ageing Research Reviews* 10, 1–15, 2011.

[4] Yeh, W., Li P., Jeng Y., Hsu H., et all. 'Elastic Modulus Measurements of human liver'. *Ultrasound Medicine in Medicine and Biology* 28, 4467–474, 2002.

[5] Booth, A. J., Hadley R., Cornett A., Dreffs A., et al. 'Acellular Normal and Fibrotic Human Lung Matrices as a Culture System for In Vitro Investigation'. *American Journal of Respiratory and Critical Care Medicine* Vol 186, 2012, doi:10.1164/rccm.201204-0754OC.

[6] Guvendiren M. and Burdicj J. 'Stiffening Hydrogels to probe short- and long-term cellular response to dynamic mechanics'. *Nature Communication*, 3:792, 2012.

[7] Mattei G., Ferretti C., Tirella A., Ahluwalia A. and Mattioli-Belmonte M. 'Decoupling the role of stiffness from other hydroxyapatite signalling cues in periosteal derived stem cell differentiation'. *Scientific Reports* 5:10778, 2015.

[8] Broderick E., Halloran D., Rochev Y., Griffin M., Collighan R. and Pandit A. Set al, 'Enzymatic Stabilization of Gelatin-Based Scaffolds' JBMR B, 72:37-42, 2005.

[9] Mattei G, Gruca G., Rijnveld N. Ahluwalia A. 'The nano-epsilon dot method for strain rate viscoelastic characterisation of soft biomaterials by spherical nano-indentation'. *Journal of the Mechanical Behavior of Biomedical Materials*, 50:150-9, 2015.

[10] Wells R. 'Tissue mechanics and fibrosis'. *Biochimica et Biophysica Acta-Molecular Basis of Disease* 1832: 884–890, 2013.

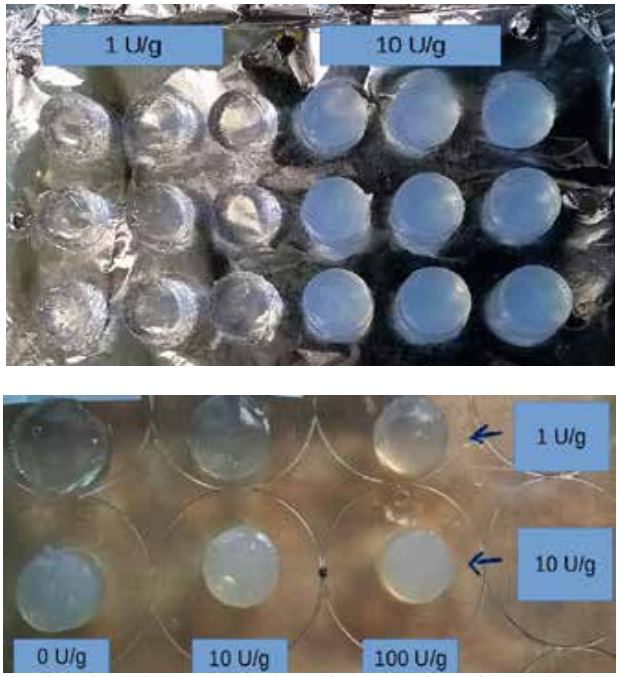

Fig. 1. mTG-gelatin hydrogels: a) day 0 (1 U/g and 10 U/g represent the internal concentrations of mTG); b) day 1 (U/g values on the rows represent mTG internal concentrations, while U/g values on the columns are the exogenous mTG concentrations administered to mTG-gelatin samples).

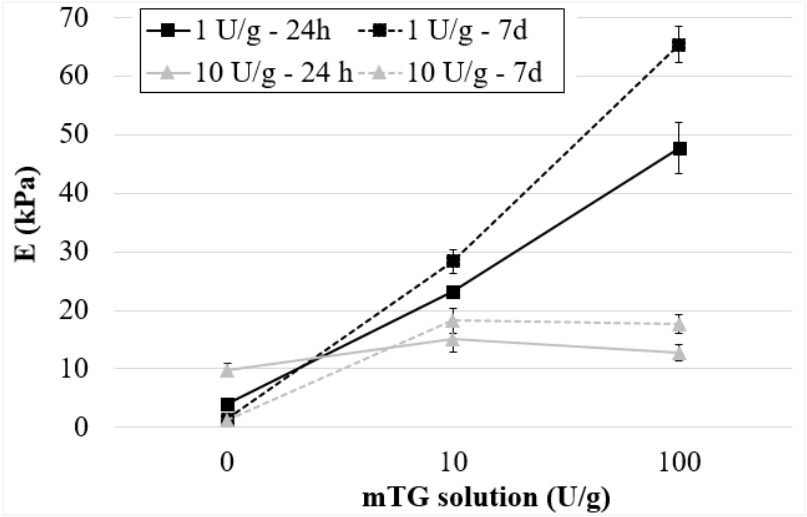

Fig. 2. Elastic moduli of 1 and 10 U/g mTG-gelatin samples immersed in mTG solutions after 1 and 7 days.

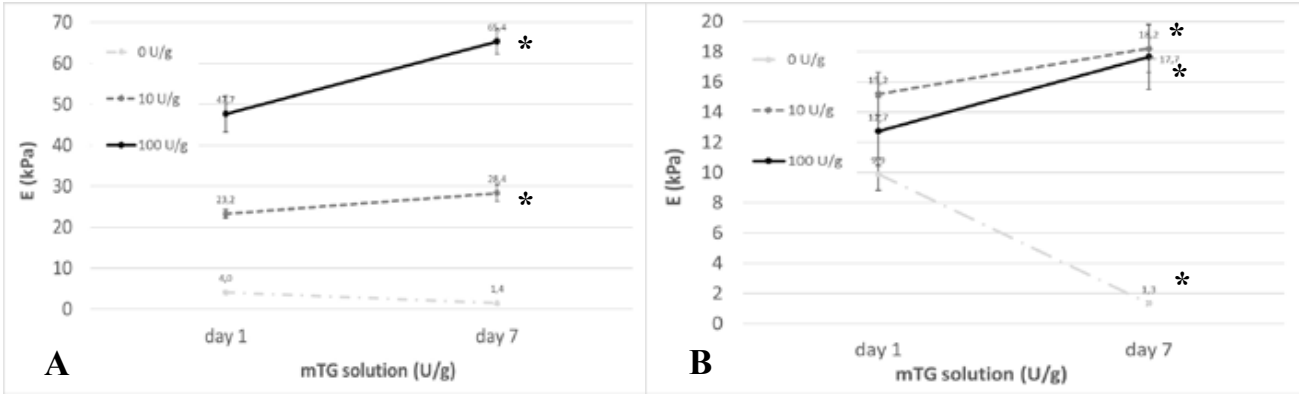

Fig. 3. ANOVA interaction plot of a) 1 U/g and b) 10 U/g mTG-gelatin samples. For each exogenous mTG concentration, significant differences between E at day 1 and 7 are denoted with an asterisk ($p < 0.001$).

Biomechanical evaluation of skin lesions: a combined approach

E. Cutrì[1], F. Crippa[1], G. Franzetti[1], E. Mortin[2], G. Spadola[3], A. Testori[3], L. Mainardi[2], and G. Pennati[1]
[1] *LaBS-Depart. of Chemistry, Materials and Chemical Engineering, 'Giulio Natta', Politecnico di Milano, Milan, Italy.*
[2] *Depart. of Electronics, Information and Bioengineering, Politecnico di Milano, Milan, Italy.*
[3] *Dermatoncological Surgery Division, Istituto Europeo di Oncologia, Milan, Italy.*

***Abstract*—Malignant melanoma is a highly aggressive skin cancer whose rate of mortality dramatically decreases if detected in the initial phases of its development. For this reason, early recognition of melanoma is of upmost importance. Enhancement in the imaging technique such as confocal laser scanning microscopy (CLSM) enabled the obtainment of high-resolution images but up to date, a definitive diagnosis can be achieved only after excisional biopsy and subsequent histological analysis. Literature studies assessed alteration in the mechanical properties of the biological tissue when a pathological condition occur. In this context, we propose a combined approach comprising an experimental analysis and a computational modelling. The latter will be devoted to the obtainment of transverse displacement from CLSM images while the former will be devoted to the development of a multiscale approach to fully characterize the skin and skin lesion. Such a combined approach will allow further understanding on biomechanical changes that occur in presence of skin lesions.**

***Keywords*—skin lesion, multiscale, skin biomechanics**

I. Introduction

MALIGNANT melanoma is a highly aggressive skin tumour whose incidence has dramatically risen in the last decades causing the 75% of skin cancer-related deaths [1]. The 5-years survival rate ranges from 15% if lately detected to 99% if early detected [2]. For these reasons, the early recognition of melanoma is of upmost importance. Currently, the diagnosis is performed using the so-called ABCDE rule, which is based on the visual evaluation of dermatoscopic features (Asymmetry of the lesion, Border irregularity, Color variegation, Diameter dimension and Evolution). Suspicious melanoma undergo to excisional biopsy and subsequent histological analysis. Improvements in diagnostic imaging technique allowed the obtainment of higher resolution with respect to classical dermatoscopy analysis. Confocal laser scanning microscopy (CLSM) is able to provide the visualization of the upper layers of the skin layers with a cellular resolution. Nevertheless, biopsy and histological analyses are mandatory to provide a final diagnosis. In this context, exploring new methodologies to investigate the changes occurring when such a pathological conditions initiate could suggest new clinical pathways. Starting from these considerations, our study aims at evaluating if mechanical alterations that occur when the pathology develops can be used to help the clinical decision. Several literature study in fact assessed a modification of the mechanical properties of biological tissues during the development of the metastasis of cancers such as carcinoma [3], [4] or melanoma [5]-[7].
In this view, a combined approach including an experimental analysis and a computational study is proposed to characterize the mechanical properties of the superficial layers of the skin and skin lesion . In the latter CLSM images of the skin and skin lesions are obtained before and after the application of a mechanical stimulus. The depth-dependent behaviour of the skin layers is investigated by calculating the transverse displacement after the stimulus. The former is aimed at reproducing the experimental condition to identify the different layers material parameters for skin and skin lesions that allow reproducing the transverse displacement experimentally obtained.

II. Material and Methods

To fully characterize the skin and skin lesions, a combined approach is proposed comprising an experimental and a computational analysis. The former is devoted at the evaluation of the response of the skin and skin lesion when a displacement field is applied. The latter is aimed at the assessment of the different mechanical properties of the skin layers and to establish if the skin and skin lesions exhibit a different behaviour.

A. Experimental set up

The experimental set up consisted of a CLSM Vivascope® 1500 (MAVIG VivaScope Systems, Munich, Germany), a tissue ring, an adhesive plastic window, an adhesive tape (Opsite Flexigrid, Smith & Nephew, London, UK) and a (pliers) support. The schematic of the experimental set up is illustrated in figure 1. The CLSM probe is coupled to the tissue ring on which a disposable adhesive plastic window is glued. This plastic window adheres to the skin. In this way, a displacement is applied to the CSLM probe, which in turn transmits it to the skin. In vivo CLSM images were acquired on the dorsal forearm of healthy Caucasian volunteers. Image stacks (500 x 500 μm, depth 152 μm) were acquired in undeformed and deformed (i.e., the CLSM probe is submitted to a displacement of 250 μm along the X direction) configurations (Fig. 1). For both configurations, the stacks were reconstructed and the displacement field was computed through a registration strategy, which estimated the best alignment of the deformed and undeformed images [8]. The depth-dependent displacement was computed to evaluate if different behaviors are evident in the different layers for the skin and skin lesion.

B. Computational model

To obtain the mechanical information of the different skin layers, a multi-scale approach was adopted ranging from macroscale, microscale up to cellular scale. The schematic of the multi-scale approach is illustrated in figure 2.

Starting from CLSM subject specific model of the skin and skin lesions have been created.

1. Tissue macroscale model

The subject specific 3D FE tissue macroscale models were developed using Abaqus 6.13 ® (SIMULIA, Dessault Systèmes, France). Each layer was modelled as an isotropic hyperelastic material using the Neo-Hooke constitutive equation and incompressibility was assumed. For each layer the thickness is measured from CLSM images and assumed constant. A displacement type boundary condition is applied in correspondence of the area of the adhesive plastic window, a shear stress is applied to simulate the effect of the fluid under the same plastic window. The model is complemented with appropriate boundary conditions to simulate the effect of surrounding tissue. The material parameters of the different layers are initially set according to literature data and then iteratively varied until the numerical transverse displacement matches the experimental one.

2. Tissue microscale model

Once the material parameters in the tissue macroscale models are obtained, the corresponding subject specific 3D FE tissue microscale models accounting for the upper layers of the skin (i.e., stratum corneum, epidermis, basal membrane and dermis) are set up. These models were developed using Abaqus 6.13 ® and the material behaviour of each layer is describe as an incompressible isotropic hyperelastic material as in the tissue macroscale models. At this level, the peculiar morphology of the basal membrane is taken into account. The geometry of the basal membrane is reconstructed from CLSM images using Rhinoceros (Seattle, WA, USA). To obtain the material parameter of the membrane a traction test in numerically performed on a specimen comprising the subject specific basal membrane the epidermis and the dermis. This information is then added to the tissue microscale models. Each subject specific model is then complemented with displacement boundary conditions obtained from the corresponding tissue macroscale model.

3. Cellular model

The cellular scale model was developed using Chaste (Cancer, Heart And Soft Tissue Environment, University of Oxford), an open source code which allows the modelling of the interactions among different types of cells. The aim of the model is to reproduce the cellular composition of different regions of interest modifying the ratio of melanocytes- and keratinocytes. Two families of cells have been defined, the leukocytes and melanocytes each with a cellular dimension of 8 μm. The cellular interaction are set according to literature indications. A displacement boundary condition is applied.

C. Results

For the sake of brevity, we report the comparison of the transverse displacement computed for skin and skin lesion from the CLSM registration and that numerical simulated using the tissue macroscale model (Fig. 3). A good agreement has been achieved between the experimental (dots) and the computational (line) for both the skin lesion (a) and the skin (b). In addition, it worth noting that while in the case of skin the slope of the displacement show only a variation from the stratum corneum to the lower layers, in the skin lesion the changes in the slope are observed in the epidermis, the DEJ and the dermis. These changes depend on the variation of the mechanical properties: the estimated Young's modulus in case of skin lesion at the derma-epidermal junction the is five-fold greater than case of normal skin. The analysis of the deformation field for skin (c-d) and skin lesions (e-f) also showed a higher gradient of the deformation in the skin lesion in correspondence of the DEJ.

III. Conclusion

The combined approach here proposed allowed to obtain the experimental transverse displacement in skin and skin lesions of healthy volunteer. The multiscale model provided important information on the modification of the mechanical properties in the skin lesion with respect to the normal skin. Such a methodology represents an interesting and suitable tool to be applied in the investigation of the melanoma to obtain further understanding of such pathology as well as indications to support clinical diagnosis.

Acknowledgement

This project was supported by Fondazione Ieo, Milan, Italy.

References

[1] A.V. Giblin, J.M. Thomas. (2007). "Incidence, mortality and survival in cutaneous melanoma" *J Plast Reconstr Aesthet Surg*, vol 60, pp. 32-40. http://dx.doi.org/ 10.1016/j.bjps.2006.05.008

[2] Skin Cancer Foundation. Skin Cancer Facts. 2012. Available from: http://www.skincancer.org/Skin-Cancer-Facts.

[3] M. J. Paszek, N. Zahir, K. R. Johnson, J. N. Lakins, G. I. Rozenberg, A. Gefen, C. A. Reinhart-King, S. S. Margulies, M. Dembo, D. Boettiger, D. A. Hammer, V. M. Weaver. (2005) "Tensional homeostasis and the malignant phenotype" *Cancer Cell,* vol. 8 (3), pp. 241-54. http://dx.doi.org/ 10.1016/j.ccr.2005.08.010

[4] M. Plodinec , M. Loparic , C.A. Monnier, E. C. Obermann, R. Zanetti Dallenbach , P. Oertle , J. T. Hyotyla, U. Aebi, M. Bentires-Alj, R.Y. Lim and C. A. Schoenenberger. (2012). "The nanomechanical signature of breast cancer" *Nat Nanotechnol,* vol. 7 (11), pp. 757-65. http://dx.doi.org/ 10.1038/nnano.2012.167

[5] M. I. Miga, M. P. Rothney and J. J. Ou. (2005). "Modality independent elastography (MIE): potential applications in dermoscopy" *Med Phys,* vol. 32 (5), pp. 1308-20. http://dx.doi.org/ 10.1118/1.1895795

[6] S. J. Kirkpatrick, R. K. Wang, D. D. Duncan, M .Kulesz-Martin and K., Lee. (2006). "Imaging the mechanical stiffness of skin lesions by in vivo acousto-optical elastography," *Optics express,* vol. 14 (21), pp. 9770-9. http://dx.doi.org/ 10.1364/OE.14.009770

[7] G .Weder, M. C. Hendriks-Balk, R. Smajda, D. Rimoldi, M. Liley, H. Heinzelmann, A. Meister, and A. Mariotti. (2014). "Increased plasticity of the stiffness of melanoma cells correlates with their acquisition of metastatic properties" *Nanomedicine: Nanotechnology, Biology, and Medicine*, vol. 10, pp. 141:148. http://dx.doi.org/ 10.1016/ j.nano.2013.07.007

[8] E. Montin, E. Cutrì, G. Spadola, A. Testori, G. Pennati, L. Mainardi. (2015, November.) "Tuning of a deformable image registration procedure for skin component mechanical properties assessment" *Proceedings of the Annual International Conference of the IEEE Engineering in Medicine and Biology Society, EMBS,* pp. 6305-6308. http://dx.doi.org/ 10.1109/EMBC.2015.7319834.

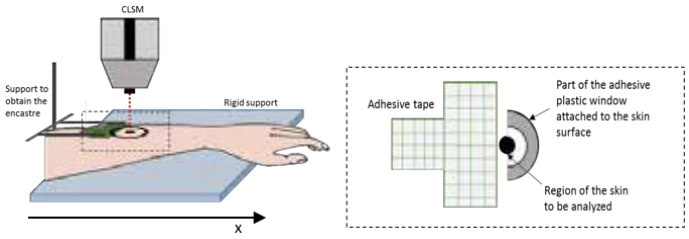

Fig. 1. Schematic of the experimental set up. The CLSM probe is attached to the skin through a tissue ring and an adhesive plastic window (*left*). The adhesive plastic window was cut so that only half was attached to the skin surface and on the opposite side, an adhesive tape was attached onto the skin surface and held through a support to obtain an encastre (*right*).

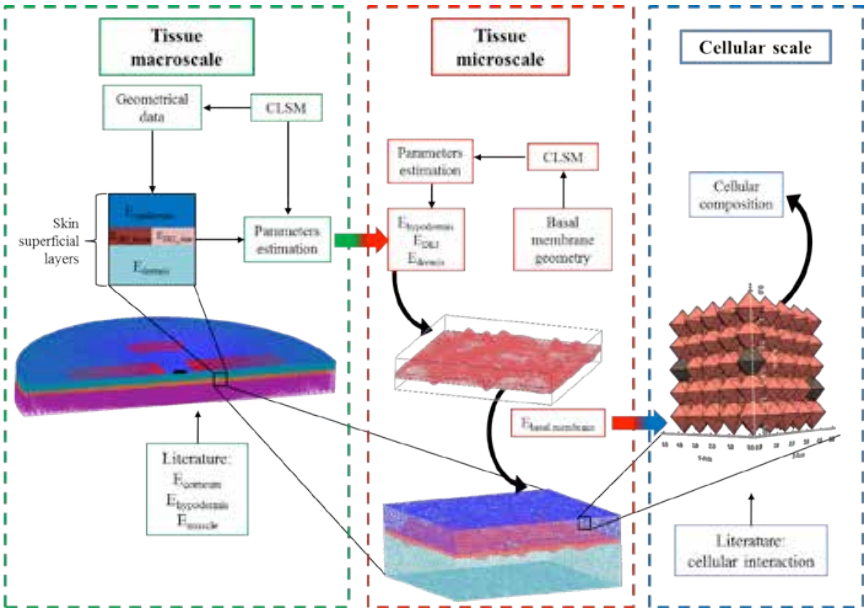

Fig. 2. Schematic of the multiscale model. From the left to the right: tissue macroscale (*green*), tissue microscale (*red*) and cellular scale model (*blue*).Geometrical data from CLSM and data from literature are integrated in the models. The figure underlines the communications of parameters between the three models.

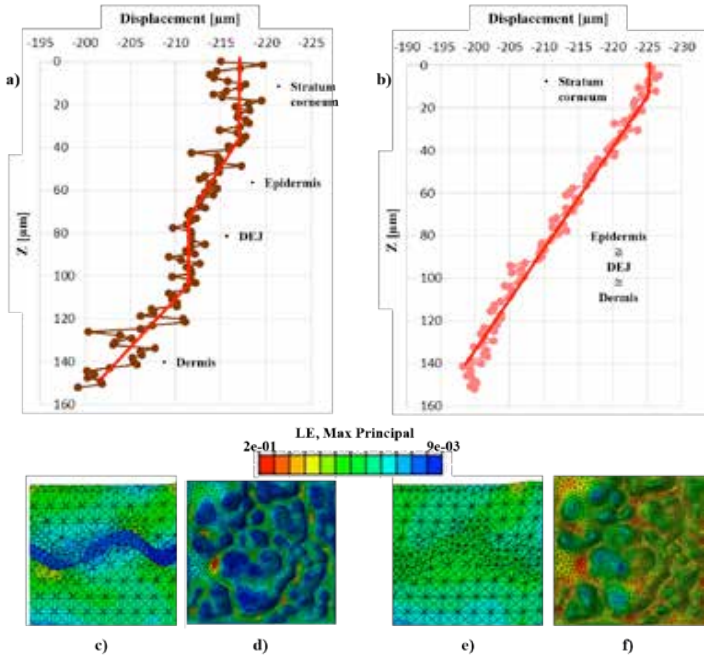

Fig. 3. Results of the computational model. *Top*: comparison of the transverse displacement for the skin (a) and skin lesion (b) obtained from the CLSM images (dots) and from simulation (line). *Bottom:* maps of the deformation for the skin (c-d) and the skin lesion (e-f).

First application of digital volume correlation to study the efficacy of prophylactic augmentation

V. Danesi[1], G. Tozzi[2], and L. Cristofolini[2]
[1] *Department of Industrial Engineering, Alma Mater Studiorum – University of Bologna, Italy*
[2] *School of Engineering, University of Portsmouth, UK*

***Abstract*—The aim of this study was to measure, for the first time, the full-field three-dimensional strain distribution inside prophylactic-augmented vertebrae in the elastic regime and to failure. Eight porcine vertebrae were prophylactically augmented using two different cements. They were micro-CT scanned (40 micrometer voxel) in the unloaded state and at 5%, 10% and 15% compression. Internal strains were computed using digital volume correlation (DVC). For both cement types, the highest strains were measured in the regions adjacent to the injected cement mass, whereas the cement-interdigitated-bone was less strained. While this was already visible in the elastic regime (5%), it was a predictor of the localization of failure, which became visible at higher degrees of compression (10% and 15%) when failure propagated across the trabecular bone, sometimes reaching the cortex. Localization of the high strains and failure was consistent between specimens, but different between the two cement types: for one cement (having a lower young modulus) this was located at mid-height, at the same level as the cement mass; for the other one (having a higher young modulus) strain concentration and failure were cranial or caudal to the cement mass. This study demonstrated the potential of DVC in measuring the internal strain (elastic regime) and failure in prophylactic-augmented vertebrae. While the cement-interdigitated region becomes stronger (less strained), the adjacent non-augmented trabecular bone is affected by the stress concentration induced by the cement mass, and tends to fail. This approach can help establishing better criteria to improve the vertebroplasty and augmentation.**

***Keywords*— Prophylactic vertebral augmentation, Digital volume correlation, Bone fracture, Full-field three-dimensional strain measurement.**

I. Introduction

THERE are cases in which vertebrae are at high risk of fracture, such as in with low bone mineral density or metastatic lesion. One prophylactic strategy that has recently been proposed to reduce fracture risk in weak vertebrae is the mechanical reinforcement of the vertebral body by injection of a foreign augmentation material. Past studies only investigated structural failure [1-3] and the surface strain distribution [4]. To elucidate the failure mechanism of the augmented vertebral body, information is needed about the internal distribution of strains. With the recent and rapid progress of high-resolution micro-CT imaging in conjunction with *in situ* mechanical testing, digital volume correlation (DVC) emerged as a novel tool for the measurement of 3D deformation fields throughout entire bone volumes [5]. The aim of this study was to improve the understanding of the failure mechanism inside prophylactic-augmented vertebral bodies under compression. DVC was used for the first time to measure the full-field internal strain distribution inside the vertebral body, in the injected cement, and in the cement-bone interdigitated region of vertebrae that were prophylactic-augmented with two different cements, including both the elastic regime (axial components of strain), and the internal micro-failure mechanism.

II. Materials and Methods

Eight single thoracic porcine vertebrae were divided in two groups:

- Augmentation with Cal-CEMEX Spine (Tecres, Italy) was performed on 4 intact vertebrae.
- Augmentation with Mendec Spine (Tecres, Italy) was performed on 4 intact vertebrae.

Destructive tests were performed with a step-wise axial compression (0%, 5%, 10% and 15% compression). MicroCT images were acquired at each step (typically 40 micron resolution). DVC analysis (LaVision, UK) was performed on the microCT-reconstructed volumes to obtain the full-field displacement and strain distribution, in order to identify the onset and progression of bone-biomaterial failure in the natural and prophylactic augmented vertebral body.

III. Results

In all of the augmented specimens, the micro-CT images (Fig. 1) showed a main micro-damage, at 15%. For both cement types, the cement region appeared to be undamaged, even at the final loading stage (15%); failure tended to initiate in the trabecular bone adjacent to the cement-bone interdigitated region. In the majority of the Mendec specimens (3 out of 4, Fig. 1) the main micro-

damage was localized in the trabecular bone at mid-height, at the same level of the cement mass. Such a collapse seemed to initiate from the cement-bone interface, then gradually spread across the trabecular bone anteriorly and finally in the transverse plane reaching the cortical bone. Only for specimen Mendec-4 collapse initiated at the two extremities (Fig. 1, 15%), which ended with a trabecular crushing in most of the cranial and caudal region, far away from the augmented region. The specimens augmented with Cal-CEMEX showed a main micro-damage localized in the trabecular region just cranial or caudal to the cement mass (Fig. 1, 15%). Only in Cal-CEMEX-3 the micro-damage was at the same height of the cement mass, towards anterior (Fig. 1, 15%). Similar to the Mendec specimens, such a collapse initiated from the cement-bone interface, and gradually developed across the trabecular anteriorly or posteriorly in the transverse plane, in some cases affecting the cortical bone (Cal-CEMEX-2 and Cal-CEMEX-3).

At the first compression step (5%) the localization of high-strain regions varied between specimens (Fig. 3-4). Conversely in the final loading step (15%) the cement regions seemed to be less strained in all specimens, and the largest strains were generally observed adjacent to the cement-bone interdigitated region. In the Mendec specimens, the highest strains observed at 10% and 15% compression were at mid-height, at the same level of the cement mass (Fig. 2). Conversely, in the Cal-CEMEX specimens the largest strains were just cranial and caudal of the cement mass (Fig. 3). The highest strain was localized in a single region within the augmented vertebral body for most specimens; the only exceptions were Mendec-3 and Cal-CEMEX-4, where two distinct strain peaks were observed, adjacent to the cement mass. For the specimens augmented with both cement types, the regions of high strain seemed to match very well the localization of micro-damage visualized in the micro-CT images (Fig. 1). Strains were markedly lower away from the most stressed regions where damage initiated. The strain distribution in the augmented vertebrae in the elastic regime (5%) seemed to predict the location of the micro-damage initiation before it actually became identifiable (at 10% and 15%) in the most of the specimens (Fig. 2 and 3). Only the specimen Mendec-1 showed a relocation of the highest axial strain from the posterior (5%, Fig. 2) to the anterior region (15%).

IV. Conclusion

Both the micro-CT images, and the DVC strain analysis highlighted that: the cement mass was less strained than any other regions in the vertebra and was never the point of failure initiation. This can be explained with the additional stiffening and reinforcement associated with the infiltration of the cement inside the trabecular bone. The highest strains and failure were localized in the bone adjacent to the cement-bone interdigitated region. This can be explained by the stress concentration between two regions: the cement-interdigitated bone, which has become stiffer and stronger, and the adjacent non-augmented trabecular bone (where some trabeculae might also have been damaged by the injection process). The specimens augmented with the two cement types seemed to have different failure mechanisms: this could be possibly associated with the different stiffness of the two cements. In conclusion, this study has demonstrated the potential of digital volume correlation in measuring the internal strain (elastic regime) and failure in prophylactic-augmented vertebrae. It has been shown that failure starts inside the augmented vertebral body, next to the injected cement mass. This can help establishing better criteria (in terms of localization of the cement mass) to improve the clinical protocols for vertebroplasty and augmentation.

Acknowledgement

The authors with to thank: Tecres for donating the bone cements and providing the injection kits. Funding was provided by the Royal Society (RG130831), the University of Portsmouth and the European Society of Biomechanics (ESB mobility award 2014).

References

[1] M. Kinzl, "The effect of standard and low-modulus cement augmentation on the stiffness, strength, and endplate pressure distribution in vertebroplasty," *Eur Spine J*, vol.21,pp.920-9,2012.

[2] N. Furtado, "A Biomechanical Investigation of Vertebroplasty in Osteoporotic Compression Fractures and in Prophylactic Vertebral Reinforcement," *Spine*, vol.32, 2007.

[3] P.F.Heini, "Augmentation of mechanical properties in osteoporotic vertebral bones a biomechanical investigation of vertebroplasty efficacy with different bone cements," Eur Spine J, vol.10, pp.164-71, 2001.

[4] L. Cristofolini, "A preliminary in vitro biomechanical evaluation of prophylactic cement augmentation of the thoracolumbar vertebrae ", JMMB *in press*

[5] B. C. Roberts, "Application of the digital volume correlation technique for the measurement of displacement and strain fields in bone: a literature review", *J Biomech,* vol.47, pp.923-34, 2014

On the impact of modeling assumptions in subject-specific hemodynamic simulations of low-density lipoproteins transport in aorta

G. De Nisco[1], P. Zhang[2], D. Gallo[1], X. Liu[2], X. Deng[2], R. Ponzini[3], G. Rizzo[4], and U. Morbiducci[1]

[1] *Department of Mechanical and Aerospace Engineering, Politecnico di Torino, Turin, Italy*

[2] *School of Biological Science and Medical Engineering, Beihang University, Beijing, China*

[3] *CINECA, Milan, Italy*

[4] *IBFM, Research National Council, Milan, Italy*

***Abstract*—In this study we use an image-based hemodynamic model of human aorta to investigate the influence of different strategies of applying boundary conditions (BCs) on low-density lipoproteins (LDL) transport and wall transfer. Findings from simulations clearly show that the imposition of idealized, rather than PC-MRI measured velocity profile as inflow BCs in subject-specific computational models of mass transport could largely affect the location and extension of regions of LDL polarization at the luminal surface of the aorta.**

***Keywords*— Low-density lipoproteins transport, arterial mass transport, computational hemodynamics, atherosclerosis.**

I. Introduction

THE complex hemodynamics observed in the human aorta make this district a site of election for an in depth investigation of the relationship between fluid structures, transport and patho-physiology. In fact, it is well known that hemodynamics play an important role in the mass transport of blood specimen, and in turn, in their transfer to the vascular wall and ultimately in the localization of vascular disease in areas of complex arterial flow. In particular, the accumulation of lipoproteins in the arterial intima is a hallmark of atherosclerosis. Low-density lipoproteins (LDL) are the most abundant atherogenic lipoproteins in plasma and high plasma levels of LDL are causally related to the development of atherosclerosis [1].

In the last decade the coupling of medical imaging and computational fluid dynamics (CFD) has contributed to enhance the comprehension of the aortic hemodynamics, with the possibility to obtain highly resolved blood flow patterns in anatomically realistic arterial models. In particular, in the context of a subject-specific oriented approach, PC-MRI has emerged as able to provide the anatomical and hemodynamic inputs to even more realistic, fully personalized flow simulations [2]. Moreover, personalized computational modeling of mass transfer has been proposed as a powerful way of addressing abnormalities in mass transfer patterns, which could be in themselves atherogenic [3]. In this regard, a recent study investigated the effects of geometric features of human aorta on the flow pattern and the luminal surface LDL concentration. More in detail, it was investigated the role played by aortic torsion, branching, taper, and curvature on LDL transport and luminal surface distribution in four aortic models with different geometry [4].

In this study we analyze the influence of different possible strategies of applying PC-MRI measured data as inflow boundary conditions (BCs) to confidently model LDL transport and transfer in image-based hemodynamic models of human aorta. In detail, the influence on LDL transport of assumptions regarding the velocity profile at the inlet section of the ascending aorta. We impose PC-MRI measured 3D velocity profiles (i.e. locations-dependent direction and magnitude of velocity vectors at the inlet section) at the inlet of the computational model and compare the obtained results, in terms of low-density lipoproteins transport, to the results of two equivalent computational models with the same instantaneous flow rate prescribed as measured 1D velocity profiles (i.e. magnitude of velocity vectors normal to the inlet surface) and flat velocity profile inlet BCs. Technically, steady-state flow simulations were carried out at three representative phases of the cardiac cycle for the three inlet velocity profiles considered. The LDL distribution at the aortic luminal surface was computed and the results were compared.

The study here presented would contribute to clarify which is the impact of the conditions applied at inflow boundaries on aortic LDL transport. In particular, the comparison of LDL transport at the aortic luminal surface as obtained prescribing idealized *vs* measured velocity profiles as inflow BCs, will contribute to clarify which is the level of detail obtained from measured phase velocity, sufficient to satisfactorily simulate mass transport/transfer in personalized computational hemodynamics models of human aorta.

II. Methods

The geometry of an ostensibly healthy human aorta was reconstructed from 4D PC-MRI images. PC-MRI slices were used to generate the model of aorta into the Vascular Modeling Toolkit environment by applying a multiple step procedure for the extraction of the surface mesh of the thoracic aorta from PC-MRI data [5]. The finite volume method was applied to perform numerical simulations under steady flow conditions. The general purpose CFD code Fluent (ANSYS Inc., USA) was used on computational mesh-grids with high quality prismatic cells near the wall at the inlet surface and structured tetrahedral elsewhere, semi-automatically generated using ICEM (ANSYS Inc., USA). The domain was equipped with straight flow extensions at the outlet faces and divided into about $4 \cdot 10^6$ cells. Blood was modeled as an isotropic, incompressible, homogeneous, Newtonian viscous fluid with density equal to 1060 kg/m^3 and dynamic viscosity equal to 3.5 cP. The LDL diffusion coefficient in blood was set to $5.94 \cdot 10^{-9}$ m^2/s. Arterial walls

were assumed to be rigid with no-slip condition at the wall. At the outlet sections of the model measured flow rate ratios were imposed as outflow BCs, as detailed in [5].

Steady state LDL transport in flowing blood can be described by the convective-diffusion equation for the LDL concentration *C*:

$$u \cdot \nabla C - D_L \nabla^2 C = 0 \qquad (1)$$

where u is the velocity vector and D_L is the diffusivity of LDL in flowing blood, set to $4.8 \cdot 10^{-12}$ m^2/s [4].

Flow simulations were carried by applying conditions at boundaries as measured at three different phases of the cardiac cycle (i.e. acceleration phase, systolic peak and deceleration phase, Figure 1), for a total number of nine simulations. According to a previous strategy [2], the following BC strategies were applied at the inlet section of the ascending aorta. The first strategy consists in the application of the measured PC MRI velocity profiles at the inlet section. Technically, at the inlet section of the model the measured three components of the velocity were extracted from the phase images. Using phase-contrast flow data, two different inflow conditions were generated, by imposing at the inlet of the ascending aorta: (1) PC-MRI measured 3D velocity profile at systolic peak, and at two phases of the cardiac cycle, one along the acceleration phase and the other along the deceleration phase; (2) PC-MRI measured 1D velocity profile at the same phases of cardiac cycle, obtained considering the measured velocity component orthogonal to the inlet section of the anatomic model (i.e., the axial velocity component). The second strategy is a widely applied approach and consists in the application of the measured velocity waveform at the inlet surface in terms of idealized flat velocity profile, where the velocity magnitude of flat profile was obtained by averaging 1D velocity profile, at each one of the three considered phases of cardiac cycle.

The equation (1), governing mass transport, was solved coupled to the Navier-Stokes equations by imposing the following BCs:

$$\text{BC } inlet: \quad C = C_0 \qquad (2)$$

$$\text{BC } outlet: \quad C = \frac{\partial C}{\partial n} \qquad (3)$$

$$\text{BC } wall: \quad D_L \left(\frac{\partial C}{\partial n}\right) = v_w C_w \qquad (4)$$

where C_0 is the LDL concentration in the bulk flow (set equal to $2.86 \cdot 10^{-9}$ mol/m^3 [4]), C_w is the concentration of LDLs at the luminal surface of the artery, v_w is the filtration velocity of fluid across the vessel wall (set equal to $4 \cdot 10^{-8}$ m/s [4]), and suffice *n* indicates the direction normal to the boundary.

LDL transport was computed for the three inflow conditions cases and the impact of the choice of idealized rather than measured velocity profiles as inflow BCs was investigated focusing on LDL transfer to the aortic luminal surface.

III. Results

As main finding of the study the uptake of LDL at the aortic wall (normalized with respect to the initial LDL concentration C_0 at the aortic inlet section) is reported. In detail Figure 1 presents the LDL accumulation profiles at the luminal surface obtained by imposing in silico (FLAT panel) and in vivo (1D and 3D panels) velocity profiles as inflow BCs for the three simulated phases of the cardiac cycle. Notably, differences in LDL patterns at the luminal surface are present, depending on the applied velocity profile at the inflow. In detail, the surface area subjected to elevated LDL accumulation is markedly wider than the 3D and 1D cases, when flat velocity profile is prescribed at the aortic inflow section. The FLAT case presents three luminal regions at the aortic arch subjected to severe polarization of LDL, more evident during the acceleration phase of the cardiac cycle (inner lateral edge of the brachiocephalic artery, intrados of the ascending aorta and inner wall of the descending aorta). The same regions were identified in [4], as interested by elevated LDL accumulation. LDL polarization at these luminal regions sensibly decreases in 1D and 3D simulation cases. Results obtained for 3D and 1D cases show a more uniform LDL distribution at the wall along the aortic arch, with a weak increase in LDL polarization at the inner wall of the descending aorta. In general, Figure 1 confirms that light or negligible differences can be appreciated in LDL transport between 1D and 3D cases at the three cardiac phases here investigated.

IV. Conclusion

The findings of this study show that the imposition of idealized velocity profile as inlet BCs in subject-specific computational hemodynamics models of mass transport in the human aorta could largely affect the location and extension of regions of LDL polarization at the luminal surface. We conclude that the plausibility of the assumption of idealized velocity profiles as inlet BCs in personalized model of the aortic hemodynamics could not, or could loosely, hold true. This finding needs further investigation, because of the fact that it is derived from steady-state flow analysis. The same analysis will be extended to unsteady-state simulations, applying the same scheme as proposed in previous works [2]. Ultimately, the approach here proposed is intended to be applied to elucidate the role played by the aortic helical flow in mass transport [6], in particular in testing the hypothesis that the promoted-by-helicity mixing of blood could be beneficial in suppressing severe LDL polarization at peculiar aortic regions, thus being part of the physiologic atheroprotective mechanism.

References

[1] J.M. Tarbell, "Mass transport in arteries and the localization of atherosclerosis", *Ann Rev Biomed Eng*, vol. 5, pp. 79-118, Aug. 2003.

[2] U. Morbiducci, R. Ponzini, D. Gallo, C. Bignardi, G. Rizzo, "Inflow boundary conditions for image-based computational hemodynamics: Impact of idealized versus measured velocity profiles in the human aorta", *J Biomech*, vol. 46, pp. 102–109, Jan. 2013.

[3] C.R. Ethier, "Computational modeling of mass transfer and links to atherosclerosis", *Ann Biomed Eng*, vol. 30, pp. 461-471, Apr. 2002

[4] X. Liu, F. Pu, Y. Fan, X. Deng, D. Li, S. Li, "A numerical study on the flow of blood and the transport of LDL in the human aorta: the physiological significance of the helical flow in the aortic arch", *Am J Phys Heart Circ Phys*, vol. 297, pp. H163–H170, 2009.

[5] D. Gallo, G. De Santis, F. Negri, D. Tresoldi, R. Ponzini et al., "On the use of in vivo measured flow rates as boundary conditions for image-based hemodynamic models of the human aorta: implications for indicators of abnormal flow", *Ann Biomed Eng*, vol. 40, pp. 729-741, March 2012.

[6] U. Morbiducci, R. Ponzini, G. Rizzo, M. Cadioli, A. Esposito et al., "Mechanistic insight into the physiological relevance of helical blood flow in the human aorta: an in vivo study", *Biomech and Modeling in Mechanobiology*, vol. 10, pp. 339-355, June 2011.

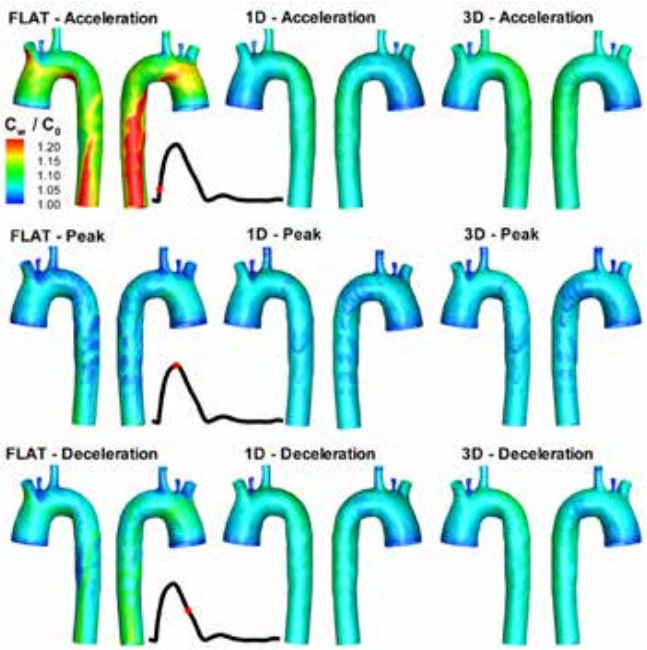

Fig. 1. Comparison of the normalized LDLs concentrations at the luminal surface for the simulated inflow boundary conditions.

Tendon tissue engineering: decellularization protocol for equine-derived tendon matrix

M. Ferroni[1*], A.F. Pellegata[2*], M. Bottagisio[2], M. Moretti[2], A.B. Lovati[2] and F. Boschetti[1]
[1] *Department of Chemistry, Materials and Chemical Engineering Giulio Natta, Politecnico di Milano, Milan, Italy*
[2] *Cell and Tissue Engineering Laboratory, IRCCS Galeazzi Orthopaedic Institute, Milan, Italy*
** These authors contributed equally to this work*

***Abstract*—Tendon ruptures remain a clinical challenge and require the replacement of the damaged tissue. The current use of autografts is an established approach but related to a low biocompatibility and biomechanical properties. This study aimed to identify a novel decellularization protocol for equine tendons to obtain a suitable substitute for the regeneration of injured tendons. Samples were analyzed by biochemical and biomechanical tests. 1% TBP+3% PAA was identified as the proper decellularization protocol, then tested for cell viability.**

***Keywords*—xenograft, biomaterials, decellularization, equine tendon biomechanics.**

I. Introduction

TRAUMATIC tendon ruptures or losses require a surgical replacement of the damaged tissue. Currently, tendon autografts are the common choice to reconstruct the tendon integrity but with several limitations [1], [2]. In the recent years, tissue engineering widely investigated the use of scaffolds that might be seeded with host cells to promote tissue and functional integration [3]. Several decellularization techniques of xenografts by using chemico-physical agents have been studied, since bioengineered graft with biochemical and biomechanical properties similar to the native tendon should be compatible with the receiving host [2]. In this context, equine species is the most suitable source in terms of tissue supply, whereas the tri(n-butyl) phosphate (TBP) and peracetic acid (PAA) are the most efficient agents to optimize cell removal, maintaining all functional requirements. Our study wants to identify a proper decellularization protocol to obtain an extracellular matrix as suitable substitute able to deliver reseeded cells for the regeneration of injured tendons. The main goal was to remove intrinsic cells from equine superficial digital flexor tendons (SDFT) by means of the 1% TBP associated or not to low concentrations of PAA. Thus, we evaluated the biochemical and biomechanical properties of decellularized tendons and we compared them to fresh-stored SDFT to determine any effect of the treatments on the tissue. Finally, we tested the best decellularization protocol in supporting the attachment and growth of the NIH-3T3 murine fibroblasts.

II. Materials and Methods

A. Preparation of equine SDFT

Equine SDFT were harvested from adult horses and 10 cm length portions were excised, washed in phosphate-buffered saline (PBS) and dry-stored at -80 °C. Then, specimens were thawed at room temperature (RT) in saline solution, sectioned into slices and frozen until processing.

B. Decellularization methods

Tendon slices of each donor were treated by one of the following protocols starting from 1% TBP: (1) 0% PAA, (2) 1% PAA, (3) 3% PAA and (4) 5% PAA. An untreated slice of each donor was used as control (native tendon, NT). Slices to treat were immersed in PBS, then decellularized in 1% TBP buffered in 1M Tris-HCl (pH=7.8) under agitation. Following, slices were rinsed and stored to remove residual detergents. After this passage, specimens were immersed in 0.0025 % DNAse-I in PBS under agitation and later washed in ddH2O and PBS. The last step was a different incubation in 0%, 1%, 3% or 5% aqueous solution of PAA. Finally, slices were rinsed in ddH2O and PBS, then stored in PBS or dry-stored for several analyses.

C. Biochemical characterization

DNA assay allowed to measure DNA content and post-decellularization cellular component by means of a cell proliferation assay (CyQuant® kit–LifeTechnologies, Monza, Italy) and fluorescence spectroscopy (Perkin Elmer Victor X3 microplate reader). The quantification of sGAG was performed on decellularized and native tendons using the 1,9-dimethylmethylene blue dye-binding assay (Sigma-Aldrich, Milan, Italy). The sGAG concentration was determined by reading the absorbance at 500 nm (Perkin Elmer Victor X3 microplate reader). In order to quantify the collagen content, we firstly removed proteoglycans and prepared the supernatant obtained from the collagen residue. The optical densities, obtained from the supernatant by absorption spectroscopy, were interpolated in a curve of absorbance, using collagen type I from rat-tail soluble in acetic acid. Data obtained were expressed as total acid-soluble collagen.

D. Biomechanics

Biomechanical testing was performed starting from rectangular specimens obtained from the decellularized and native tendons, using an electromagnetic testing machine (MTS Synergie, Eden Prairie, MN, USA), equipped with a load cell of 1 kN. The mean dimensions of the samples were 39±8 mm length, 14±2 mm width and 2.4±0.6 mm thickness. Tension protocol consisted of multi-ramp stress-relaxation tests, followed by the strain-controlled tension up to failure at 1%/s strain rate. For stepwise stress relaxation tests, three tension steps up to 2% strain were applied, at 1%/s strain rate, followed by 1000s of stress relaxation. The pure elastic response (Er) was calculated from the equilibrium data of the stress relaxation tests. The tendon hyperelastic response, the elastic modulus at high strains (EM) and the failure stress and

strain were derived from the failure tests. Experimental data were fit to a viscoelastic model by means of a Prony series to evaluate the first four relaxation time constants.

E. Repopulation of the decellularized matrix

Tendons decellularized by means of TBP + 3% PAA were sterilized into 70% ethanol, washed in PBS and left unseeded as negative control or seeded with NIH-3T3 murine fibroblasts and cultured in complete medium. 150 µL of the cell suspension was deposed onto the surface to seed the tendon. Then, the medium was added and both the unseeded and seeded tendon matrices were statically cultured for 7 days. The cell viability of seeded fibroblasts was evaluated performing a Live&Dead Viability/Cytotoxicity test (Life Technologies, Monza, Italy).

III. RESULTS

A. Biochemical analysis

The DNA content data, measured to analyze the capability of the decellularization protocols on cell removal, show that all treated samples reduce the DNA content if compared to the NT, supporting previous histological cell count. Moreover, an important decrease in DNA content was found in the groups treated with TBP + 3% PAA and TBP + 5% PAA (cell removal of 98% and 99%, respectively) and it responds to the minimal criteria (50ng/mg dry weight in Fig. 1A) to satisfy the purpose of tissue decellularization [2]. Figure 1B shows a significant decrease of sGAG content in tendon treated with TBP + 5% PAA but no significant differences were detected in the samples decellularized with TBP + 1% PAA, TBP + 3% PAA and TBP, with respect to NT. Figure 1C reports a significant decrease of the collagen content in tendon treated with all the protocols with respect to NT but a higher collagen content for the TBP group compared to the other protocols.

B. Biomechanical tests

The results of stress-relaxation tests conducted on native and decellularized samples with TBP + 1% PAA, TBP + 3% PAA, TBP + 5% PAA and TBP are reported in figure 2.A. The results of the failure tests report a hyperelastic response, particularly figure 2.B shows the EM at high strains. The tendons treated with all the decellularization protocols did not show significant changes in EM compared to the NT but only a significant difference was found between TBP + 1% PAA and TBP + 5% PAA, indicating a stiffer behavior of tendons treated with TBP + 1% PAA. The EM value for NT was 181±78 MPa. According to this, there was not a significant difference in failure stress and strain values measured after the decellularization with respect to the NT (one-way ANOVA coupled with Bonferroni's post hoc test). The average values of the relaxation constants at 2% of strain are shown in figure 3 and were not dependent on the decellularization protocol.

C. Cell colonization of the decellularized matrix

Accordingly to biochemical and biomechanical results, TBP + 3% PAA was considered the best decellularization protocol and used to reseed the equine tendons with NIH-3T3 fibroblasts. After 7 days of culture, the Live&Dead assay demonstrated a preserved viability of the seeded cells (Fig. 4), with a percentage of living cells of 80±9 %. This analysis, in addition to the collagen content in reseeded matrix, showed metabolic activity, NIH-3T3 viability and well distribution on the surface of the construct.

IV. DISCUSSION AND CONCLUSION

The present study wants to identify a proper decellularization protocol for large equine tendons by means of specific combination of TBP and PAA, biochemical and biomechanical tools. The results of the current study indicated that the TBP + 3% PAA and TBP + 5% PAA treatments reduced the resident cell amount by obtaining DNA values lower than the minimal criteria for clinical use [3]. The percentage of cell removal obtained by these two treatments was the most effective data obtained until now in the field of tendon decellularization protocols, to the best of our knowledge. These data strictly correlated with the sGAG analysis, in which well-preserved sGAG content was found in tendons treated with TBP + 3% PAA without any significant difference compared to the NT. Total collagen content was lower in all the tested decellularization protocols, since the exposure to PAA could affect the collagen content. All the tested decellularization protocols produced acellular scaffolds with mechanical properties similar to the NT for EM, failure stress and strains. High concentrations of PAA affected the pure elastic response of the tendon as evaluated by the stress-relaxation tests. Nevertheless, the tendons treated with TBP + 1% PAA demonstrated a greater stiffness in the whole viscoelastic behavior, whereas higher concentrations of PAA restored the viscoelastic response of the NT behavior. The maintenance of proper biomechanical features is mandatory either for the tissue engineering approaches to develop a tendon substitute. In terms of cell viability, our results demonstrated a good fibroblast cytocompatibility of the decellularized matrix with TBP + 3% PAA. According to the results of the current study, the TBP + 3% PAA seems to be the most suitable decellularization protocol for large tendon grafts, being highly effective in cell removal, matrix structure and cell reseeding. Our protocol led to the generation of biocompatible, acellular tendon scaffolds that will be suitable as substitutes for tendon tissue engineering.

ACKNOWLEDGEMENT

This study was funded by the Italian Ministry of Health (RF- GR-2011-02348899). The NIH-3T3 murine fibroblasts were kindly provided by Dr S. Previdi (Institute for Pharmacological Research Mario Negri, Milan, Italy).

REFERENCES

[1] L. W. Yao, et al. (2015). Patellar tendon autograft versus patellar tendon allograft in anterior cruciate ligament reconstruction: a systematic review and meta-analysis. *Eur. J. Orthop. Surg. Traumatol. 25(2).* pp. 355-365. doi: 10.1007/s00590-014-1481-5.

[2] C. W. Cheng, L. D. Solorio, and E. Alsberg (2014). Decellularized tissue and cell-derived extracellular matrices as scaffolds for orthopaedic tissue engineering. *Biotechnol. Adv. 32(2).* pp. 462-484. doi:10.1016/j.biotechadv.2013.12.012.

[3] P. M. Crapo, T. W. Gilbert, and S. F. Badylak (2011). An overview of tissue and whole organ decellularization processes. *Biomaterials. 32(12).* pp. 3233-3243. doi:10.1016/j.biomaterials.2011.01.057.

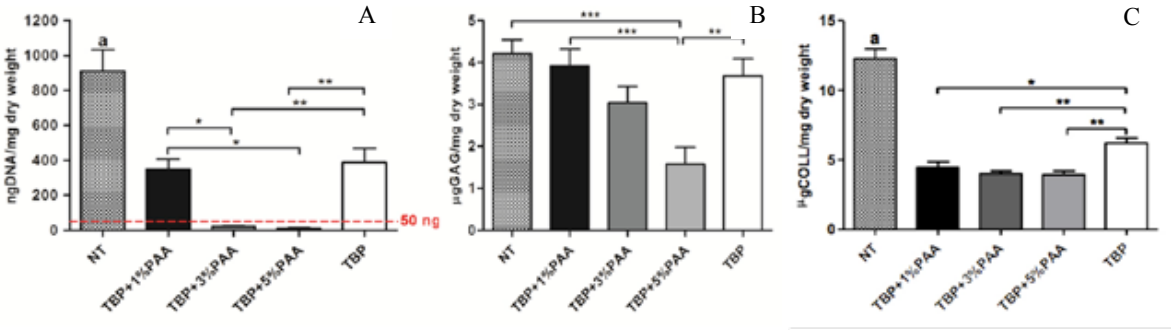

Fig. 1. Effects of the decellularization protocols on DNA (A), sGAG (B) and collagen content (C). Comparisons among groups were analyzed with one-way analysis of variance (ANOVA) coupled with Bonferroni's post hoc test (* $p<0.05$, ** $p<0.01$; a, *** $p<0.001$).

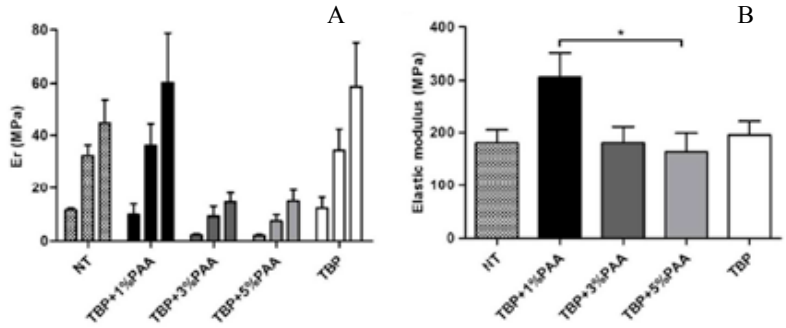

Fig. 2. Histogram of the relaxation moduli for the three ramps (A) and elastic modulus (B) comparing NT and the decellularization protocols. Comparisons among groups were analyzed with one-way analysis of variance (ANOVA) coupled with Bonferroni's post hoc test (*$p<0.05$).

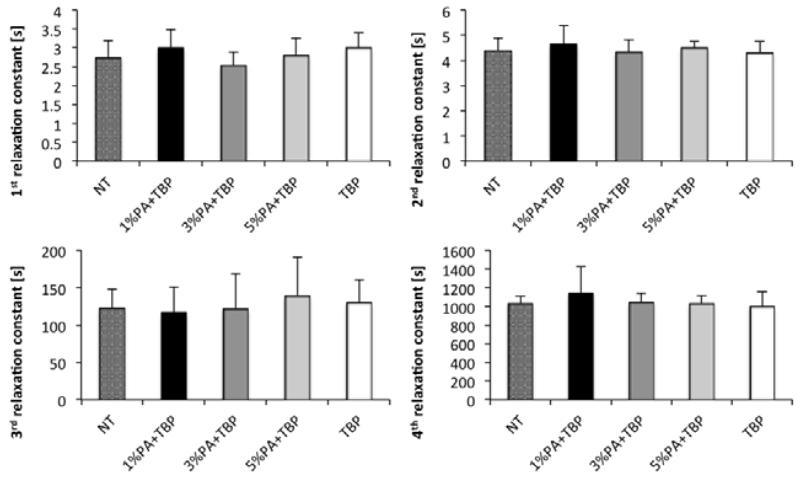

Fig. 3. Relaxation time constant values of the first four terms of Prony series for each decellularization protocols.

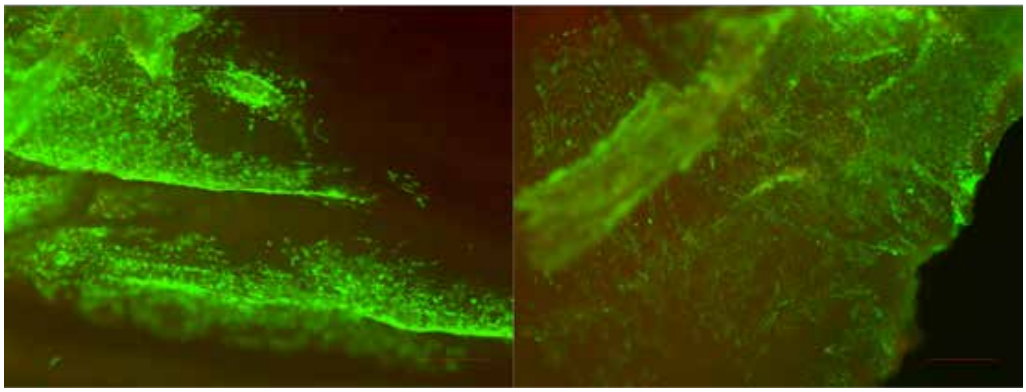

Fig. 4. Two representative panels of the Live&Dead of the reseeded matrix, with a percentage of living cells of 80±9 % and dead cells of 20±9 % (scale bars 200 μm).

Numerical model of ocular posterior chamber: fluid-dynamics for intravitreal drug delivery

M. Ferroni[1], A. Moioli[1], E. C. Sganzerla[1], M. G. Cereda[2], and F. Boschetti[1]
[1] *Department of Chemistry, Materials and Chemical Engineering Giulio Natta, Politecnico di Milano, Milan, Italy*
[2] *Eye Clinic, Department of Biomedical and clinical science Luigi Sacco, Sacco Hospital, University of Milan, Milan Italy*

***Abstract*—Nowadays, intravitreal injections are one of the most common techniques for the treatment of ocular diseases. To predict the transport mechanism of the injected drug, the fluid-dynamics inside the posterior chamber has to be known. This study aims at implementing a full CFD modeling of the vitreous domain. The main novelty of this work is the optimization of the boundary conditions. Results of the full CFD model suggest that effects of the physiological environment and the saccade must be taken into account.**

***Keywords*—computational fluid-dynamics, ocular drug delivery, vitreous, saccade.**

I. Introduction

MANY ocular diseases can be treated by means of specific drugs, delivered by several clinical methods. One of the possible drug delivery method consists in the intravitreal injection, which overcomes the limits of topical and intravenous drug delivery techniques but can lead to other ocular complications. The vitreous humor is a gel-like structure that acts as delivery medium in the posterior chamber of the eye. Several studies showed a liquefaction process after the age of 50 years, inducing an increase of the liquid volume [1]. Numerical models are powerful tools able to study the intravitreal fluid-dynamics, which is fundamental to predict the drug delivery mechanism. To the best of our knowledge, few literature studies have been devoted to the evaluation of the ocular fluid-dynamics. One study defines the flow of aqueous humor inside the vitreous and reports that the drug distribution is strictly related to the diffusion coefficients and the size of molecules [2]. By contrast, other works consider the effect of saccadic movements on the drug distribution injected intravitreally and report that convection transport is dominant for different diffusivities and injection locations [3], [4]. The goal of our study is to implement a novel CFD model able to compute the overall ocular fluid-dynamics, accounting for both the physiological environment and the ocular saccadic movement due to the extraocular muscles. In our opinion, this approach will allow us to define a powerful tool to predict the fluid-dynamics and the consequent drug delivery in case of ocular diseases.

II. Materials and Methods

A. Geometrical model

The model geometry represents the effective anatomy and shape of the human posterior chamber, which is bounded by the hyaloid membrane, the lens and the retina-choroid-sclera (RCS) membrane (Figure 1.A). The values of the radii of curvature of the retina and lens are equal to 0.85 cm and 0.55 cm, respectively. The retina and lens have two centers of curvature with respect to the hyaloid membrane, the posterior one of 0.61 cm, and the anterior one of 0.24 cm.

B. Governing equations

The fluid-dynamics of the vitreous is modelled by means of the Navier-Stokes and the continuity equations for a 3D unsteady incompressible Newtonian flow:

$$\rho \nabla \cdot \boldsymbol{u} = 0 \quad (1)$$

$$\rho \frac{\partial \boldsymbol{u}}{\partial t} + \rho(\boldsymbol{u} \cdot \nabla)\boldsymbol{u} = \nabla \cdot [-pI + \mu(\nabla \boldsymbol{u} + (\nabla \boldsymbol{u})^T)] \quad (2)$$

where ρ is the fluid density, $\boldsymbol{u}$ the fluid velocity vector, p the hydraulic pressure and μ the fluid viscosity. The vitreal density and viscosity are equal to 995.32 kg/m^3 and $7.3164 \cdot 10^{-4}$ Pa·s respectively, because we considered the high liquefaction for age-related diseases and the specific ocular temperature (T=34°C) [5].

C. Boundary conditions

We identified two kinds of boundary conditions, one related to the physiological surrounding around the posterior chamber and the other connected to the ocular saccadic movements. In particular, we imposed i) no aqueous permeation through the lens, ii) pressure at the posterior hyaloid surface equal to the physiological intraocular pressure

(IOP) and iii) normal velocity across the porous RCS membrane and defined as follows:

$$n \cdot v = Kp(p - Pv) \quad (3)$$

where Kp is the hydraulic conductivity ($5 \cdot 10^{-10}$ cm/Pa·s) [2] and Pv (1200 Pa) is the venous pressure downstream. Then, we implemented the real saccadic movement to all the external boundaries, connected to the rotation imposed by the extraocular muscles (Figure 2). This eye angular displacement relation consists in a fifth polynomial function with 50° of saccade amplitudes, the maximum angular displacement that a human eye can reach [3].

D. Mesh and computer code

Structured meshes (Figure 1.B), used to discretize the computational domains, and all the simulations were performed using the commercial software Comsol Multiphysics 5.2 (COMSOL Inc., Burlington, MA, USA).

III. Results

A. Effects of the physiological environment

We firstly simulated the effect of the physiological environment without considering the saccadic rotation. The results report an internal pressure equal to 2000 Pa in the entire posterior chamber and a steady permeating flow across the SCR membrane, with a mean velocity magnitude at the retinal surface and inside the vitreous chamber are $4 \cdot 10^{-7}$ cm/s and $1.08 \cdot 10^{-6}$ cm/s, respectively. The total volumetric flow through the retinal surface is 0.18312 µL/min. These results match with the data proposed by Stay *et al*.

B. Effects of the saccadic movements

In a second model, we considered only the ocular saccadic movement due to the extraocular muscles stimuli. The overall fluid-dynamics is quite different if compared to the previous one, particularly the mean velocity magnitude at the retinal surface and inside the vitreous chamber are definitely higher (3.705 cm/s and 0.612 cm/s, respectively). Figure 3.A-B shows the velocity distribution on the equatorial plane at specific time steps (the acceleration time t_P and the saccade duration D). Figure 4.A-B underlines the changes in wall shear stress distribution on the vitreous chamber wall. Shear stress values increase when the velocity of the movement is maximum ($t=t_P$) and decrease when the angular velocity tends to zero, due to the change in the angular motion direction (t=D). The maximum values of shear stress and velocity and the overall distribution are in accordance with previous studies [3].

C. Full CFD model

The full CFD model aimed at the description of the overall fluid-dynamics, considering the boundary conditions imposed in the previous models at the same time. The velocity distribution on the equatorial plane does not show huge differences if compared to the previous simulation (Figure 3.C-D), confirmed by the mean velocity magnitude at the retinal surface and inside the chamber (3.667 cm/s and 0.608 cm/s, respectively). Even if we do not report significant changes in wall shear stress on the lens and retinal surface (Figure 4.C-D), a higher volumetric flow rate (3.7 µL/min) due to the simultaneous presence of IOP, ocular saccadic rotation and Darcy's flow across the retina is noticed. Streamline analysis for the averaged flow field shows two main stagnant regions on the equatorial plane (Figure 5).

IV. Conclusion

The present study aims at implementing a fully CFD model of the posterior chamber of the eye. It overcomes the limitations of literature works and represents a generalized tool to predict the ocular fluid-dynamics. Our approach will be useful to study the transport mechanisms after intravitreal injections of drugs and the changes in fluid-dynamics due to specific diseases (e.g. glaucoma, age-related macular degeneration) and surgery (e.g. vitrectomy), by tuning the model parameters.

References

[1] B. Lee, M. Litt, and G. Buchsbaum. (1992). Rheology of the vitreous body. Part I: Viscoelasticity of human vitreous. *Biorheology 29(5-6)*. pp.521-533.

[2] M. S. Stay, J. Xu, T. W. Randolph, and V. H. Barocas. (2003). Computer simulation of convective and diffusive transport of controlled-release drugs in the vitreous humor. *Pharm Res. 20(1)*. pp. 96–102. doi: 10.1023/A:1022207026982.

[3] O. Abouali, A. Modareszadeh, A. Ghaffariyeh, and J. Tu. (2011). Numerical simulation of fluid dynamic in vitreous chamber due to saccadic eye movement. *Med Eng Phys. 34(6)*. pp. 681-692. doi: 10.1016/j.medengphy.2011.09.011.

[4] A. Modareszadeh, O. Abouali, A. Ghaffarieh, and G. Ahmadi. (2013). Saccade movements effect on the intravitreal drug delivery in vitreous substitutes: a numerical study. *Biomech Model Mechanobiol. 12(2)*. pp. 281–290. doi: 10.1007/s10237-012-0398-3.

[5] M. R. Romano, J. L. Vallejo-Garcia, V. Romano, M. Angi, P. Vinciguerra, and C. Costagliola. (2013). *Thermodynamics of vitreoretinal surgery.*, *Current Eye Research*, *38(3)*, pp. 371-374. doi: 10.3109/02713683.2012.745160.

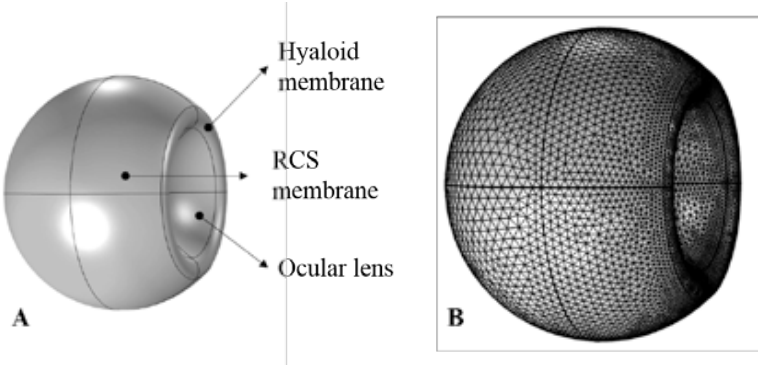

Fig. 1. Geometrical simplification of the ocular posterior chamber (A). Structured mesh used to discretize the whole CFD domain (B).

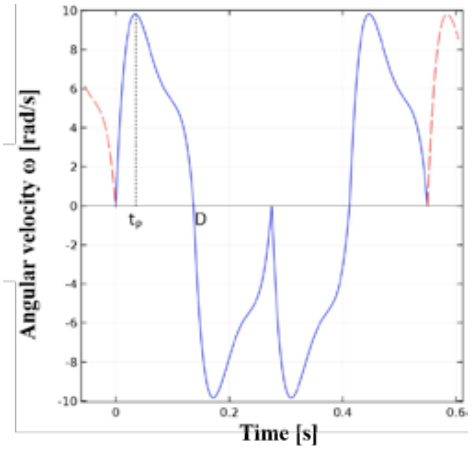

Fig. 2. The time law of the real saccadic rotation consists in four successive motions for each period, where a saccade to the left is followed by a return to the starting position and continues to the right at the same

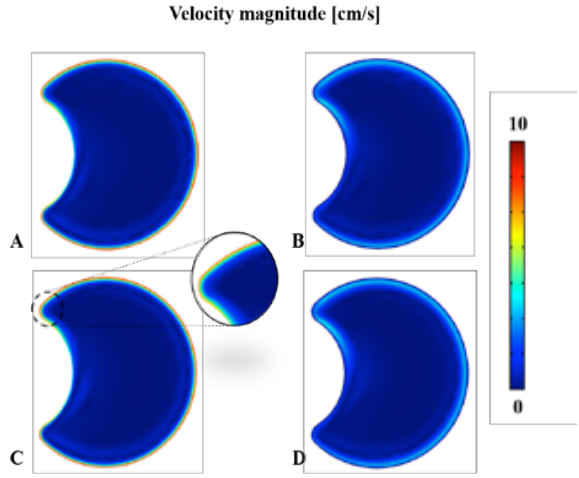

Fig. 3. Effects of the 50° saccadic movements in terms of velocity magnitude on the equatorial plane of the vitreous chamber at time t_P (A) and D (B). The full CFD model does not show significant changes (C, t = t_P - D, t = D).

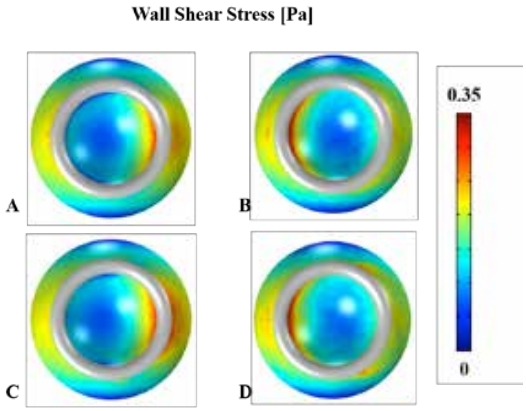

Fig. 4. Comparison of the wall shear stresses in presence of only the 50° saccadic movements (A, t = t_P – B, t = D) and those obtained by the full CFD model (C, t = t_P – D, t = D).

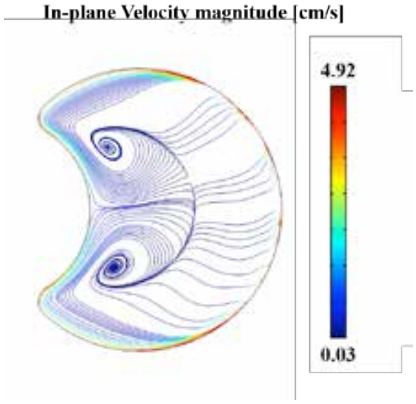

Fig. 5. Streamlines of averaged flow in equatorial plane of vitreous chamber computed by the full CFD model.

A novel pipeline for the analysis of the Multilayer Flow Modulator stent

A. Finotello[1], E. Faggiano[2], M. Conti[2], S. Morganti[2], G. Spinella[3], B. Pane[3], D. Palombo[3] and F. Auricchio[2]

[1] *University of Genova, Department of Experimental Medicine, Genova*
[2] *University of Pavia, Department of Civil Engineering and Architecture, Pavia*
[3] *Vascular and Endovascular Surgery Unit, University Hospital IRCCS San Martino-IST, Genova*

***Abstract*—The purpose of this work is to define a full framework for the analysis of the Multilayer Flow Modulator (Cardiatis, Isnes, Belgium) device in the repair of thoraco-abdominal aneurysms that provides reliable and accurate results to the surgeons. The framework includes an in-vitro study, a geometrical analysis and an in-silico investigation. In this work, the focus is given on the geometrical analysis. Therefore, geometrical indices to measure anatomical changes of the lumen and the aneurysm sac before and after the intervention are introduced. Results of the study for four patients with a two years follow-up are presented.**

***Keywords*—medical image processing, geometric analysis, TAA aneurysms, multilayer flow modulator.**

I. Introduction

Open surgery of thoraco-abdominal aortic aneurysm (TAAA) is the gold standard approach for treating such pathology but, endovascular aortic implantation can be considered a valuable alternative for patients who are not eligible for such an invasive procedure. The multilayer flow modulator (MFM) is an uncovered, self-expanding mesh of braided cobalt alloy representing a new paradigm to treat aortic aneurysms. Its main feature is to change the blood flow within the aneurysm, modifying turbulent to laminar flow and supporting the formation of organized, stable thrombus inside the aneurysm sac. As a consequence, the wall shear stress (WSS) is reduced protecting against the rupture. Thanks to device porosity, another important feature consists in the ability of maintaining perfused the side branches [1].

Clinical articles containing the firsts follow-up data of patients with Cardiatis can be found [2]. Engineering studies of the same subject are not in literature. In this context, a full engineering framework for the analysis of the MFM device represents an innovation. The study is intended to help clinicians understanding the feasibility of the intervention in TAAA using this novel device and interpreting the post-operative (short and long term) outcomes.

The overall project is divided into three tasks: in-vivo analysis, in-vitro experiments and numerical simulations. In detail, in vivo-analysis puts forth the aim of reconstructing aneurysms geometry and analyzing its changes in time, after the implantation of the MFM stent. In-vitro experiments aim at analyzing the performance of the stent in terms of porosity measuring the pressure drop through the surface of the stent. In-silico analyses integrate the previously mentioned studies simulating the hemodynamics around the stent for the quantification of WSS and flow behavior. In this paper main focus is given on the preliminary results of the in-vivo geometric procedure.

II. Methods

Through bioimaging techniques and geometrical analysis, starting from Computed Tomography (CT) images, we define a pipeline for the analysis of the geometric and morphological changes of the aneurysmatic lumen and thrombus induced by the implanted MFM device. The dataset is composed by CT images of four patients undergoing endovascular treatment at IRCCS AOU San Martino-IST, Genova. For each patient one pre-operative CT (*Pre*) and three post-operative CTs in the firsts two years of follow-up, at established times, were collected: immediately after intervention (*Post*), after 1 year (*1y*) and after 2 years (*2y*). International Review Broad approval was obtained for the conduct of this study, and the board waived the need for patient consent.

A. Segmentation and surface registration

Different segmentation processes are employed in order to extract the lumen, the MFM and the aneurysm region. A semi-automatic gradient-based level set method [3] is used to extract the lumen. A threshold technique (Hounsfield units >1000) is employed to recognize the stent region. A semi-manual technique is chosen to discern the aneurysm external wall. In particular, the manual contour of a reduced number of slices is extracted; then a 3D surface interpolation using radial basis functions is performed [4]. Later, the Iterative Closest Point algorithm [5] is used to register the follow-up surfaces to the pre-operative reference one.

B. Geometric analysis

Once segmented, we distinguish between the aneurysm, the total flow in the aneurysm sac and the residual blood flow, i.e. the blood that still flows outside the implanted stent. For each patient under study, we aim at verifying the presence or absence of blood flowing inside the aneurysm and the growth and the morphological changes of the aneurysm sac. To this end, geometric measurements on sections and volumetric indices are evaluated. Once observed that side branches remain perfused, they are eliminated from the reconstructed anatomical surface and only the principal lumen is considered [6]. Then, centerline of the vessel is computed and sections are generated, at given distances, perpendicular to this centerline. We remark that, thanks to the surface registration step, the sections are extracted at the same positions in all the pre-operative and post-operative surfaces allowing a direct comparison between different time instants. For each section we evaluate area, maximum and minimum diameter and a shape index that ranges from 0 to 1 where 1 signify a completely circular shape [7]. These

measurements are taken both for the lumen and for the total aneurysm sac.

We also evaluate some volumetric indices. First of all, we consider the total aneurysm volume (v_{tot}) and the percentage of aneurysm growth in comparison with the pre-operative configuration ($v_{tot\%}$). Residual flow volume (v_{rf}) and the percentage of total flow growth in comparison with the pre-operative blood-flow configuration ($v_{l\%}$) are also estimated. Finally, we have introduced the *RTR* ratio (see Eq. (1)), which is a 3D size index related to the percentage of intraluminal thrombus in the aneurysm sac.

$$RTR = \left(1 - \frac{v_{rf}}{v_{tot} - v_{fi}}\right) \cdot 100 \quad (1)$$

where v_{fi} is the volume of blood inside the MFM. A value of 100 % indicates a complete thrombization of the aneurysm.

III. Results

In Fig. 1 the geometric 3D reconstructions of the four patients are reported. We take the configuration *Post* as an example. Red color refers to the circulating flow, yellow to the MFM and green to the intraluminal thrombotic zone. In Fig. 2 the results obtained from the analysis on sections are presented. Considering the lumen section area, for Patient 1 we observe that after 1 year the blood flows completely inside the stent while after 2 years there is a new increment.

TABLE I
VOLUMETRIC INDICES

		v_{tot} (10^5 mm^3)	$v_{tot\%}$	v_{rf} (10^5 mm^3)	$v_{l\%}$	*RTR*
Patient 1	*Pre*	2.8				
	Post	3.9	38 %	0.5	17 %	77 %
	1y	3.8	37 %	0.1	-14 %	94 %
	2y	5.2	79 %	1.0	42 %	71 %
Patient 2	*Pre*	1.1				
	Post	1.1	11 %	0.4	-12 %	61 %
	1y	1.6	47 %	0.5	24 %	58 %
	2y	2.1	94 %	0.8	53 %	58 %
Patient 3	*Pre*	3.8				
	Post	3.9	3.2 %	1.4	40 %	48 %
	1y	4.3	13 %	0.95	17 %	69 %
	2y	4.8	26 %	1.0	24 %	70 %
Patient 4	*Pre*	2.1				
	Post	2.1	0.1 %	0.2	-10.8 %	87 %
	1y	1.95	-6.7 %	0.185	-11.7 %	88 %
	2y	1.9	-9.5 %	0.135	-12.9 %	90 %

Volumetric indices for all patients in pre-operative and post-operative configurations are calculated.

The total aneurysm remains stable until 2 years when a sudden growth is detected. Patient 2 is characterized by a gradual increase in time of both lumen and aneurysm area sections. For the Patient 3 after 1 year, the lumen areas have decreased in the proximal region but increased in the distal one. Aneurysm important growth is observed only after 2 years. Trend reversal is observed for Patient 4: both the lumen section areas and the aneurysm section areas decreased.

In Table I results of the volumetric indices are reported. Considering the aneurysm sac, for the first and the second patient, a nearly linear growth is observed. Patient 3 has a little growth of the aneurysm while for Patient 4 a volume reduction is detected. After 1 year, *RTR* index of Patient 1 has increased until 94 % indicating a nearly full thrombosed sac. For Patient 2 and Patient 4 *RTR* index does not change in time, but the latter is fixed at a higher value (≈90 %). In Patient 3 an important thrombization process is observed in the first year (*RTR* from 48 % to 69 %) followed by a stabilization.

In Fig. 3 a signed distance computed between the *Pre* and the *2y* configuration is presented to graphically illustrate the aneurysm zones where the maximum volumetric changes occurred.

IV. Conclusions and Future Developments

We have defined a new pipeline for the geometric analysis of aneurysms treated with the MFM device. The dataset is composed of four patients affected by TAAA of different geometrical shape. They are also characterized by an extremely different behaviour in terms of MFM implantation response. Therefore, our pipeline has been proved and is able to provide multiple and accurate results for any aneurysm shape and for any morphological change in time.

This is a first step within a larger project for the study of MFM feasibility.

References

[1] M. Henry, A. Polydorou, N. Frid, P. Gruffaz, A. Cavet, I. Henry et al., "Treatment of renal artery aneurysm with the Multilayer stent" in *J. Endovasc. Ther.* 2008

[2] M. Henry, A. Benjelloun and I. Henry, "The Multilayer Flow Modulator stent for the treatment of arterial aneurysms concept-Indications-contraindications", in *Journal of Indian College of Cardiology.* 2015.

[3] L. Antiga, M. Piccinelli, L. Botti, B. Ene-Iordache, A. Remuzzi, and D.A. Steinman, "An image-based modeling framework for patient-specific computational hemodynamics." in *Medical & biological engineering & computing*, 46(11), 1097-1112. 2008

[4] A. Fetzer, S. Zelzer, T. Schroeder, H.P. Meinzer and M. Nolden, "An interactive 3D segmentation for the Medical Imaging Interaction Toolkit (MITK) ", Conference: MICCAI, At Harvard Medical School, Boston, MA, United States, Volume: Proc MICCAI IMIC (Interactive Medical Image Computing). 2014.

[5] P.J. Besl and N.D. McKay, "A Method for registration of 3-D shapes" in *Proceedings of Spie- The International Society for Optical Engineering,* 14(3):239-256. 1992

[6] L. Antiga and D.A. Steinman, "Robust and objective decomposition and mapping of bifurcating vessels." in *IEEE Trans Med Imaging.* 2004

[7] M. Piccinelli, D.A. Steinman, Y. Hoi, F. Tong, A. Veneziani, and L. Antiga, "Automatic neck plane detection and 3D geometric characterization of aneurysmal sacs" in *Annals of Biomedical Engineering,* Vol. 40, No.10, pp.2188-2211. 2012

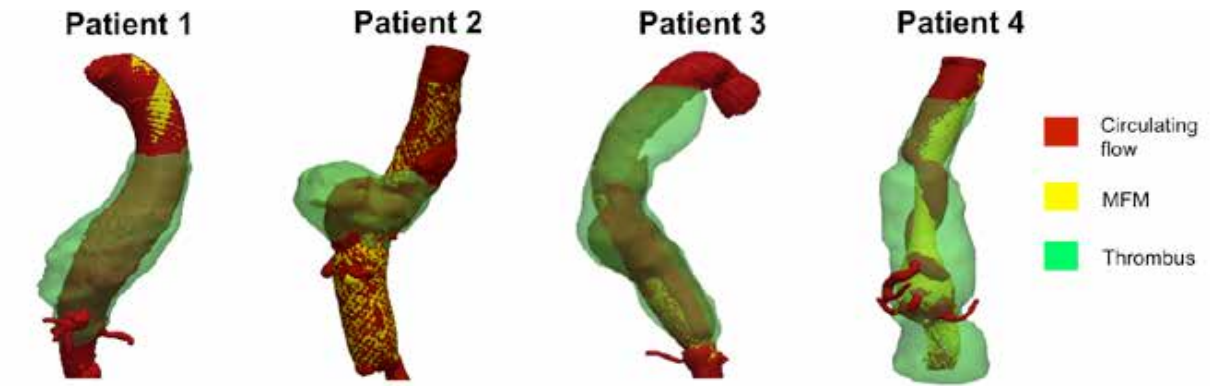

Fig. 1. 3D reconstructions concerning the configuration *Post* are depicted.

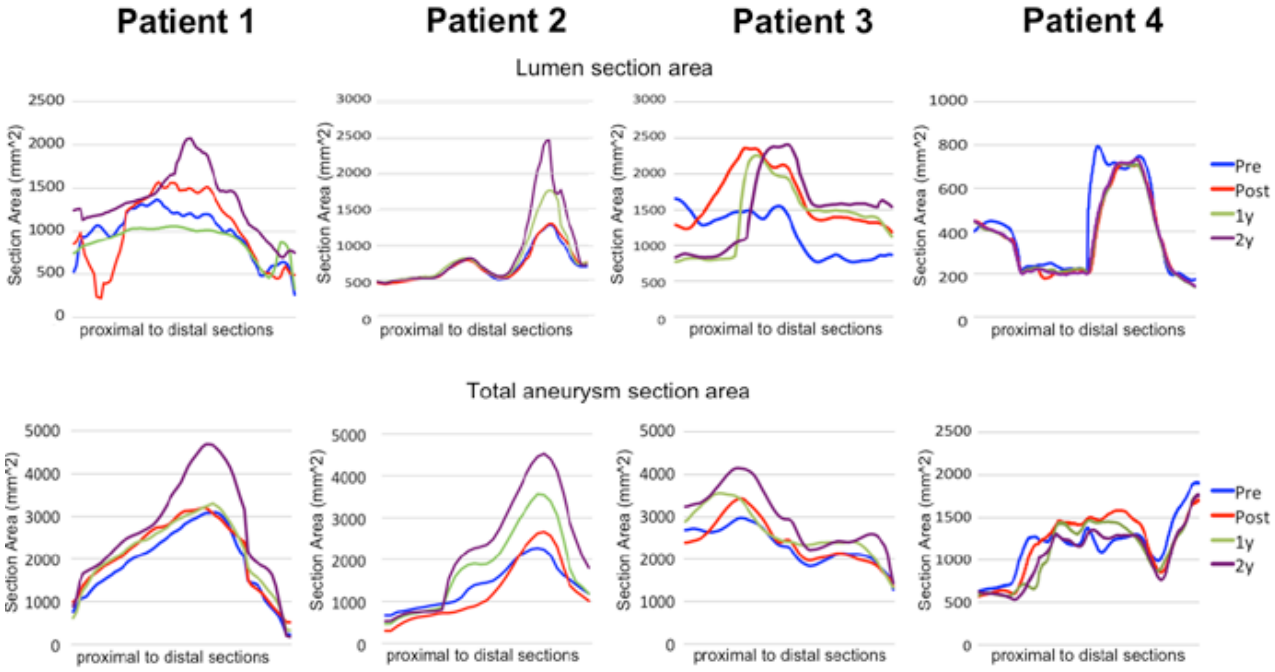

Fig. 2. Geometric indices on sections: total lumen area and total aneurysm area, for the four patients in all time configurations are considered.

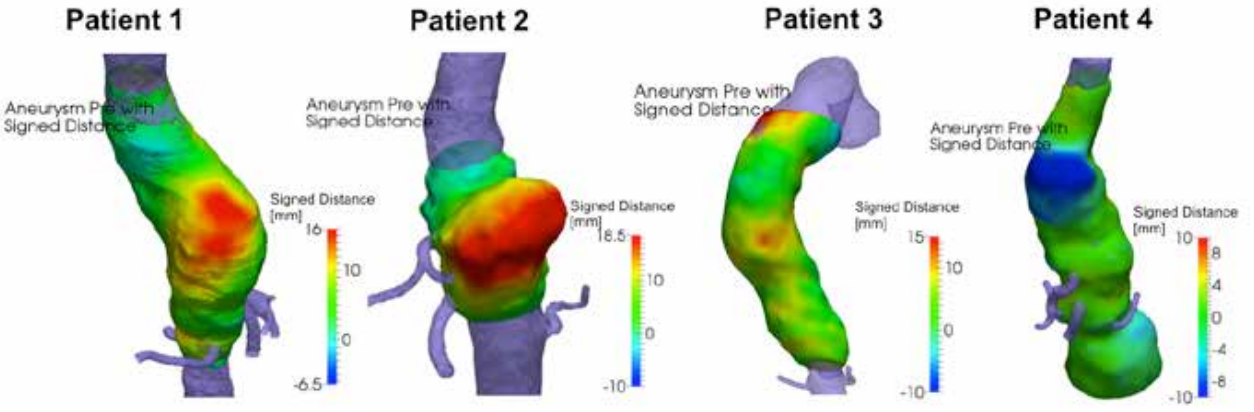

Fig. 3. For all patient signed distance between the pre-operative and the last (2y) configuration is depicted.

Experimental/computational approach of the nuclear pore complex mechanics

A García[1], R Marotta[3], M Tunesi[1], MM Nava[1], R Fedele[2], E Jacchetti[1], JF Rodríguez Matas[1] and MT Raimondi[1]

[1] *Department of Chemistry, Materials, and Chemical Engineering Giulio Natta Politecnico di Milano, Italy.*
[2] *Department of Civil and Environmental Engineering (DICA) Politecnico di Milano, Italy.*
[3] *Electron microscopy lab, Nanochemistry Department Istituto Italiano di Tecnologia, Genoa, Italy*

***Abstract*—Recent findings have shown that nuclear distortions may alter the import flux of transcription factors toward the nucleus and control the expression of genes and the protein synthesis. A possible mechanism of such a mechanosensory system resides in the nuclear pore complex (NPC). NPCs are generally considered sites of active transcription. Here we hypothesized that cell-stretching forces can mechanically activate the pore, thus allowing faster diffusivity of molecules. To this purpose, we recreated the two extreme nuclear deformation conditions (spread and round). Cell nuclei were imaged by confocal microscopy and by scanning transmission electron tomography (STEM) to asses nuclear and pore features. We also developed a multyphysics model accounting for the change in permeability in response to deformation. We found an increase in the nuclear envelope (NE) surface by up to 50% in deformed cells. Non-significant differences in both shape and size of the reinforcement ring of single NPCs with NE deformation. The computational simulations show that NE-NPC structure predominates compared to the NPC structure.**

***Keywords*—Nuclear Pore Complex, Nuclear Envelope, Diffusion, Permeability.**

I. Introduction

A basic recent understanding in stem cell differentiation is that the cell is able to translate its shape (e.g. roundish or deformed) into a fate decision. However, the mechanisms by which phenotype expression is regulated by cell shape are complex and poorly understood. Our hypothesis is that cell deformation induces nuclear deformation, which in turn causes strains in the nuclear envelope (NE). This induces a change in porosity and in permeability of the NE that affects the flux of transcription factors involved in stem cell differentiation [1]. To demonstrate this hypothesis, we set-up a numerical model of the interaction between the nuclear pore complex (NPC) and the NE.

II. Material and methods

Firstly, we recreated the two extreme deformation conditions for the NE. We isolated mesenchymal stromal cells (MSC) from the bone marrow of adult rats. To recreate the deformed configuration, we processed the cells for microscopical analysis when they were in adhesion to a flat culture substrate. On the contrary, to recreate the roundish configuration, we fixed and processed the cells in suspension. In both configurations, we acquired images of the whole nuclei by scanning confocal microscopy, to measure the NE deformation. In addition, we reconstructed 3D portions of the NE by scanning transmission electron tomography (STEM), see Fig. 1 and Fig. 2, to measure geometrical parameters of the NPC size/shape.

Secondly, in order to couple a change in permeability of the NE at the microscale with a change in configuration of a single NPC at the nanoscale (in response to the deformation applied to the NE), we fed the measured data into a computational model of the NPC-NE mechanical interaction.

III. Results

Our preliminary results show an increase in the NE surface by up to 50% together with a significant change of the local NE curvature in deformed cells, compared to roundish ones. However, we found non-significant differences in both shape and size of the reinforcement ring of single NPCs with NE deformation.

IV. Conclusion

The computational simulations show that the highly different mechanical response of the NE structure, compared to the NPC structure, predominates in determining the change in porosity of the NE in response to the applied strains. This result is consistent with experimental published evidences showing a dramatic change in NPC density and shape in cells lacking lamin, an essential nuclear protein anchoring the NPCs to the NE [2].

Acknowledgement

Manuela Teresa Raimondi has received funding from the European Research Council (ERC) under the European Union's Horizon 2020 research and innovation programme (grant agreement No 646990 - NICHOID).

References

[1] Nava et al. "*Computational prediction of strain-dependent diffusion of transcription factors through the cell nucleus,*" Biomech Model Mechanobiol, 2015, pp 1-11.

[2] Giacomini et al. "*Lamin B1 protein is required for dendrite development in primary mouse cortical neurons,*" (2015) Mol Biol Cell, doi:10.1091/mbc.E15-05-0307

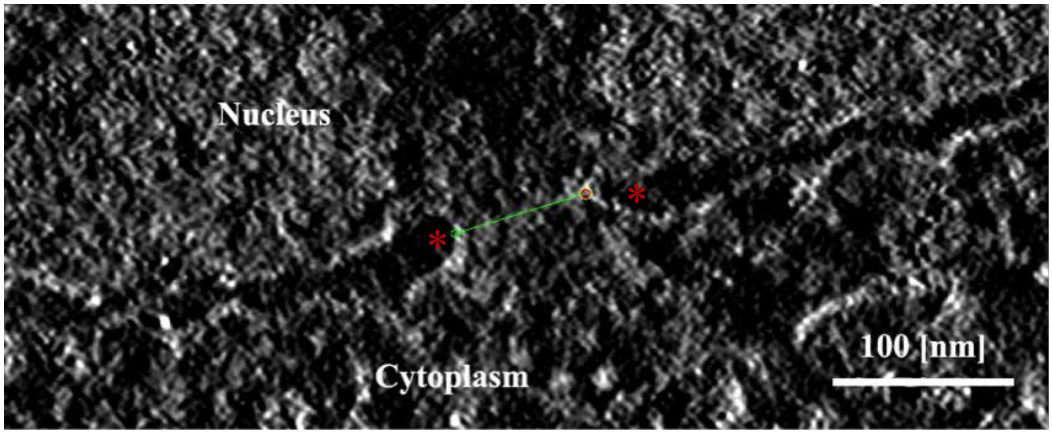

Fig. 1. Single tomographic slice through the nuclear envelope of a MSC cell grown in suspension. The highlighted distance (green) in the nuclear envelope (asterisks) corresponds to a nuclear pore complex.

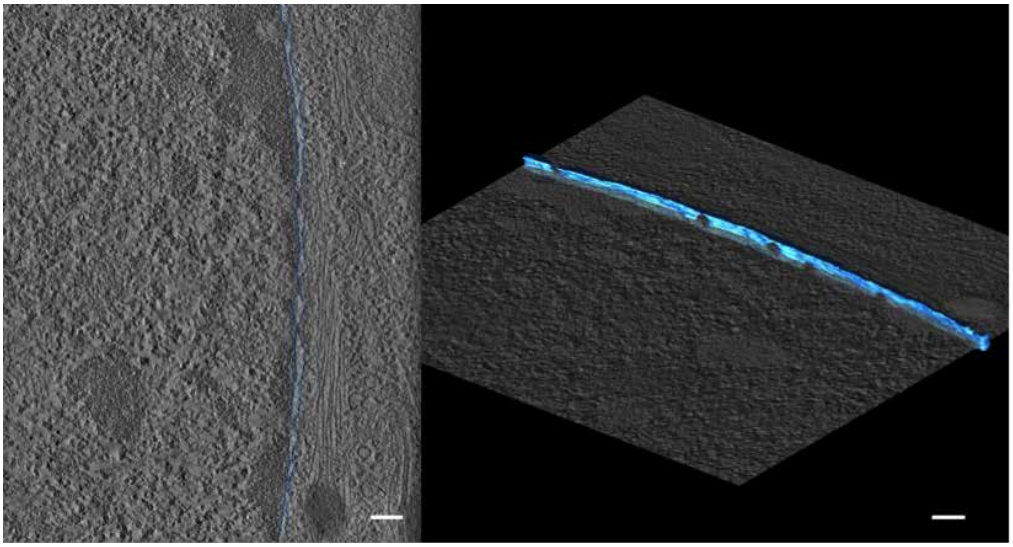

Fig. 2. Slice segmentation (blue-left image) and corresponding 3D reconstruction (blue-right image) of the nuclear envelope of a MSC. In the images it is possible to properly differentiate the location of four Nuclear Pore Complexes. The scale bar in both images corresponds to 150 [nm].

A microfluidic stretchable device for generation of multiaxial deformation patterns

S.M. Giannitelli[1,2], A. Gizzi[1,2], C. Cherubini[1], L. Businaro[2,3], M. Trombetta[1,2], and A. Rainer[1,2]
[1] *Department of Engineering, Università Campus Bio-Medico di Roma, Rome, Italy*
[2] *UCBM-CNR Joint Lab for Nanotechnologies for the Life Sciences (nano4life), Rome 00128, Italy*
[3] *Institute of Photonics and Nanotechnology-CNR, Rome 00156, Italy*

***Abstract*—We present a novel microfluidic device for the induction of complex multiaxial deformation patterns onto a stretchable porous elastic membrane. Here we report mathematically informed design, fabrication and validation of the device, which is currently under investigation for prospective application as a (co-)culture platform for excitable cells.**

***Keywords*—Microfabrication, Multiaxial cell stretching, Biomechanical optimization, Multiphysics *in silico* modelling.**

I. Introduction

In vitro cell/organ-on-a-chip models of biological microenvironments represent an emerging tool to study complex biological systems mimicking *in vivo* conditions [1]. This approach, coupling co-culture protocols, biomechanical engineering optimization and microfluidic technologies, allows to provide a high degree of control over the experimental parameters exploiting the power of modern microscopy tools, often not applicable in *in vivo* experiments [2].

Although microfluidic stretchable devices have been already developed and successfully used to study cell response under different mechanical stimuli [3], [4], a multiaxial dynamic control of cell strain is still under exploitation. In this perspective, a novel multiaxial microfluidic stretchable device is presented, which has been designed and fabricated by soft-lithographic techniques.

Realistic three-dimensional simulations of the device have been conducted via dedicated numerical modeling. The synergistic use of advanced theoretical modeling of cells and tissue electro-mechanics, microfabrication technologies and actuated 3D multilayer cultures allow for a better control of the microenvironment and represent an advanced tool for in *in vitro* research studies.

II. Materials and Methods

A. Chip design

The device consisted of two superimposed 3 x 3 mm^2 chambers separated by a porous membrane. Vacuum-driven actuators were purposely designed for multiaxial stretching of the porous membrane. Chip design also included microfluidic channels for selective perfusion of the upper and lower chambers.

B. Theoretical modelling and numerical simulation

Design optimization was performed by Finite Elements Analysis. Accurate solution of micro-features (up to 10 μm) was ensured via mesh sensitivity analysis performed over three discretization levels. The finest mesh level consisted of $\sim 4 \cdot 10^5$ tetrahedral quadratic elements and $\sim 1.5 \cdot 10^6$ degrees of freedom. The numerical solution was obtained by using Comsol Multiphysics 5.2 (COMSOL Inc., Burlington, MA) on a HP Z-800 multiprocessor workstation (192 GB RAM). The computational time was ~15 min using ~30 GB RAM.

C. Device fabrication

The device was fabricated by replica molding of polydimethylsiloxane (PDMS) starting from a silicon master with the desired relief pattern. Master molds were fabricated with SU8-2075 negative photoresist (Microchem, Newton, MA) following a standard photolithographic process according to the manufacturer's instructions. The two halves of the chip (representing the upper and lower microchannel layers) were individually prepared by casting PDMS (10:1 v/v pre-polymer to curing agent ratio) on the microfabricated mold, followed by thermal curing.

The porous membrane was prepared by a soft-lithographic technique casting PDMS (15:1 v/v ratio) onto a photo-lithographically obtained silicon master containing arrays of circular pillars.

The two chip halves with interposed porous membrane were accurately aligned and bond together by oxygen plasma activation.

D. Device actuation

Actuation of the device was performed by applying controlled vacuum levels (in the 0-600 mbar range at 50 mbar steps) at each actuator inlet using a multichannel programmable pressure controller (Elveflow OB-1 controller).

Membrane stretching was observed under a fully motorized inverted optical microscope (Nikon Ti-E) equipped with a high speed camera (Andor NEO 5.5) and control software (NIS-Elements AR).

Displacement field was calculated by particle tracking algorithm that was applied to the micrograph sequences using membrane pores as an interpolating mesh.

Equibiaxial loading patterns were studied and compared with the results of *in silico* analysis.

III. Results and Discussion

A. Device performance

Figure 1 shows the optimized geometry resulted from in silico analysis (Fig. 1A) and the corresponding microfabricated device (Fig. 1B). Thickness of the porous

membrane (10 μm) and geometry of vacuum actuators were designed as a result of in silico optimization.

Figure 2 reports a representative example of design validation. Figure 2A shows the results of numerical simulations for an applied vacuum level of 600 mbar, while Figure 2B illustrates the experimentally calculated displacement field derived from particle tracking applied to micrograph datasets. Good agreement (less than 5% error) between experimental and in silico data was reported.

The strain field (calculated from displacement datasets) gave a central circular region of ca. 1 mm diameter characterized by a relatively constant strain level (ca. 7%), in agreement with the in silico model.

IV. Conclusion

A novel microfluidic stretchable devise has been designed and successfully fabricated on the base of *in silico* optimization analysis. Good agreement between experimental and finite element analysis results has been achieved in the case of equibiaxial loading patterns.

Acknowledgement

This work is supported by Università Campus Bio-Medico di Roma (Internal Grant Program).

References

[1] A.R. Perestrelo, A.C. Águas, A. Rainer, and G. Forte, " Microfluidic Organ/Body-on-a-Chip Devices at the Convergence of Biology and Microengineering," *Sensors*, vol. 15, pp. 31142-31170, 2015.

[2] S.N. Bhatia, and D.E. Ingber, "Microfluidic organs-on-chips," *Nature biotechnology*, vol. 32, pp. 760-772, 2014.

[3] H.J. Kim, D. Huh, G. Hamilton, and D.E. Ingber, "Human gut-on-a-chip inhabited by microbial flora that experiences intestinal peristalsis-like motions and flow," *Lab on a Chip*, vol. 12, pp. 2165-2174, 2012.

[4] D. Tremblay, S. Chagnon-Lessard, M. Mirzaei, A.E. Pelling, and M. Godin, "A microscale anisotropic biaxial cell stretching device for applications in mechanobiology," *Biotechnology letters*, vol. 36, pp. 657-665, 2014.

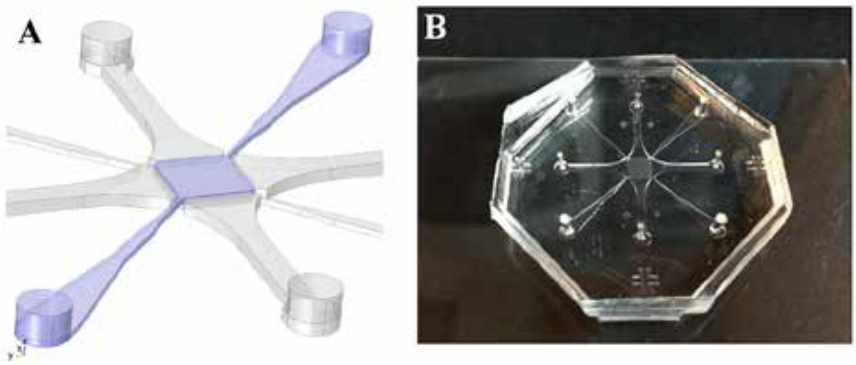

Fig. 1. 3D schematization of chip geometry obtained by in silico optimization (A) and microfabricated PDMS microfluidic devise (B).

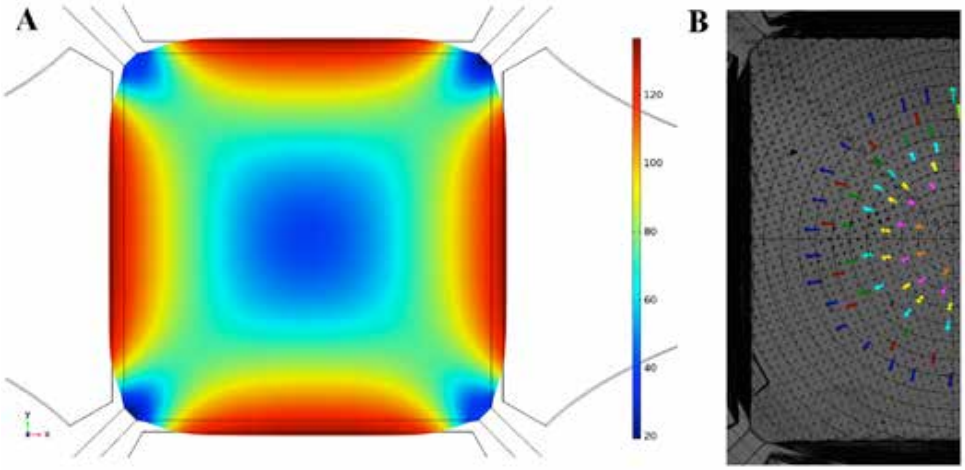

Fig. 2. Color map of membrane displacement for an applied vacuum level of 600 mbar: (A) finite element simulation and (B) experimental results. Displacements are expressed in µm.

Comparison of standard and minimally invasive decompression techniques for lumbar spinal stenosis

C. Ottardi[1], F. Costa[2], A. Ortolina[2], T. Bassani[3], D. Volkheimer[4], H-J.Wilke[4], F. Galbusera[3], T. Villa[1,3]
[1] *LaBS, Department of Chemistry, Materials and Chemical Engineering "G. Natta", Politecnico di Milano, Italy*
[2] *Department of Neurosurgery, Humanitas Clinical and Research Center, Rozzano, Italy*
[3] *IRCCS Istituto Ortopedico Galeazzi, Milano*
[4] *Institute of Orthopedic Research and Biomechanics, Ulm University, Ulm, Germany*

***Abstract* — Lumbar spinal stenosis can be surgically treated with traditional or minimally invasive decompression techniques. This study was focused on the comparison between different techniques, by means of in vitro testing on human spinal specimens. A spine tester was used to apply pure moments along three axis. The range of motion (ROM) and the neutral zone of the intact and decompressed specimens (after each resection step) was calculated. The unilateral laminotomy exhibited only small variations with respect to the intact spine. Also the minimally invasive laminectomy caused only minor changes of the flexibility. Two levels decompression caused greater differences on the ROM and the spinal instrumentation was always effective for the stabilization.**

Both minimally invasive and standard decompression techniques caused minor destabilization at the treated level.

***Keywords* — Spine biomechanics, Lumbar spinal stenosis, laminotomy, flexibility tests.**

I. INTRODUCTION

LUMBAR spinal stenosis (LSS) is usually described as a reduction of the spinal canal volume, which can also trap the nerve roots causing pain and radicular symptoms [Aebi et al. 2008]. This pathology is often caused by disc degenerations and protrusion, osteophytes formation or hypertrophy of the flaval ligament. The clinical options are conservative treatments followed by decompressive techniques when the first strategy fails. Several surgical techniques can be employed (depending on the type of stenosis) in order to enlarge the spinal canal allowing the decompression of the nerve roots.

-Laminectomy: is the traditional technique used to cut the whole lamina, the spinous process and the involved ligament (usually flaval, supraspinous and interspinous);

-Laminotomy: is a minimally invasive technique that consists in the removal of part of the lamina, preserving the supraspinous and interspinous. The flaval ligament normally is removed;

-Facetectomy: this technique is the partial or total removal of the facets.

All the techniques can be performed monolaterally or bilaterally. Even if the rate of success of the surgical procedure is high, clinical studies identified a risk of instability suggesting the instrumentation with spinal fixators problems [Aebi et al. 2008].

The goal of this study was to perform an in vitro characterization of the spine, following minimally invasive or traditional surgical decompression techniques. The flexibility of the intact, destabilized and subsequently instrumented spine was calculated.

II. MATERIAL AND METHODS

Six human specimens of healthy lumbar spines were tested. The study was performed using a spine tester, able to reproduce pure unconstrained moments along three axis in order to simulate flexion-extension, lateral bending and axial rotation. Therefore, 7.5 Nm were applied in all the directions of movement without preload. A motion capture system was used to acquire the movement of each motion segment and consequently calculate range of motion (ROM) and neutral zone (NZ) of each specimen.

Several decompression techniques were reproduced, using an incremental damage approach (Fig. 1). After the two steps, equally performed on all the specimens the samples were divided in two groups:

1- Intact specimen (n=6);
2- Unilateral laminotomy for bilateral decompression at L3-L4 (UNI-1L, n=6);
3a- Minimally invasive laminectomy at L3-L4 (BI-1L, n=3) and spinal fixation at L3-L4;
3b- Unilateral laminotomy for bilateral decompression at L4-L5 (UNI-2L, n=3);
4b- Minimally invasive laminectomy at L4-L5 (BI-2L, n=3) and spinal fixation at L3-L4.

A neurosurgical drill was used to create the decompressions and flexibility tests were performed after each resection.

A statistical analysis was conducted on the steps having 6 samples.

III. RESULTS

Unilateral laminotomy for bilateral decompression (UNI-1L) at L3-L4 had only a slight influence on the ROM, for all the typical movements of the spine (Fig. 2). The statistical analysis showed a not significant 8% increase of the ROM in flexion-extension. Conversely, the variation of the NZ resulted significant, with an increase of about 30%. In addition, the lateral bending showed significant differences

for both ROM and NZ. The axial rotation revealed a significant variation of ROM and NZ only on the left side.
Performing a minimally invasive laminectomy at the same level (BI-1L) did not cause significant changes.
The surgical techniques performed on two level led to higher variations.
The posterior instrumentation with spinal fixators greatly stabilized the spine, increasing the stiffness of the construct.

IV. DISCUSSION

This biomechanical study supported the finding that decompression techniques are able to preserve the physiological stability of the treated levels, considering either ROM or NZ. The limited number of samples did not allow a statistical analysis of all the surgical techniques. However, various interesting clinical findings can be drawn. First, the bilateral decompression obtained following unilateral laminotomy resulted slightly relevant thus, its role in inducing iatrogenic instability is negligible. The minimally invasive laminectomy did not produce a substantial instability. Also in literature the effect of minimally invasive decompressions was judged marginal [Ivanov et al 2007].
Extending the decompressions on the second level (L4-L5) induced higher changes, probably due to the higher flexibility of the lower lumbar segment. Therefore, a decompression performed at this motion segment may be more critical increasing the risk of destabilization.

V. CONCLUSION

The results of the biomechanical testing showed that the unilateral laminotomy for bilateral decompression caused only minor destabilization at the treated level, considering ROM and NZ. Also the minimally invasive technique had a small effect on the biomechanics. Thus, it can be stated that both techniques are safe and equally effective from a biomechanical perspective.

VI. ACKNOWLEDGEMENTS

The work has been funded by the Italian Ministry of Health (project GR-2011-02351464). Pedicle screws and rods have been provided for free by Sintea Plustek Srl (Assago, Italy). The microdrill has been loaned by Tekmed Instruments Spa (Rozzano, Italy).

REFERENCES

[1] M. Aebi, N. Boos and I. Zintel. “Spinal Disorders. Fundamentals of Diagnosis and Treatment”, *Springer*, 2008, pp. 513-533.
[2] A. Ivanov, A. Faizan, K. Sairyo, N. Ebraheim, A. Biyani, VK. Goel, “Minimally invasive decompression for lumbar spinal canal stenosis in younger age patients could lead to higher stresses in the remaining neural arch - a finite element investigation”, *Minim Invasive Neurosurg,* 2007, 50(1):18-22.

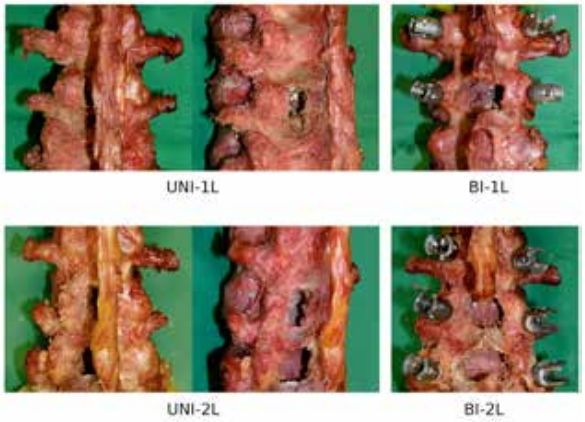

Fig. 1 Decompression and stabilization procedures performed on the specimens: unilateral laminotomy at L3-L4 ("UNI-1L", n=6 specimens); bilateral laminotomy at L3-L4 ("BI-1L", n=3); unilateral laminotomy at L3-L5 ("UNI-2L", n=3); bilateral laminotomy at L3-L5 ("BI-2L", n=3).

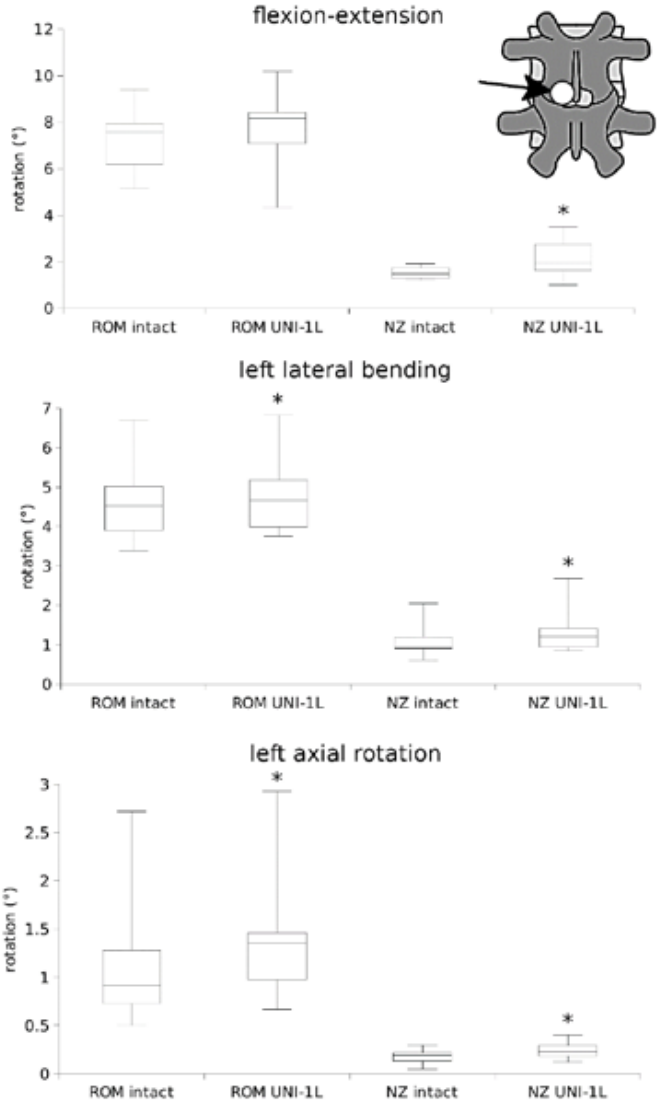

Fig. 2 Statistical comparison of the range of motion (ROM) and of the neutral zone (NZ) between the intact specimens and those subjected to unilateral laminotomy at L3-L4 ("UNI-1L"), in flexion-extension, left lateral bending and left axial rotation. "*" indicates a statistically significant difference ($p<0.05$) between the intact and the decompressed condition (n=6).

The evaluation of strain on spine segments in a contactless way and full-field view

M. Palanca[1], M. Marco[1, 2], K. Ożóg[1, 3], and L. Cristofolini[1]
[1] School of Engineering and Architecture, Alma Mater Studiorum – Università di Bologna, Italy
[2] Department of Mechanical Engineering, University Carlos III of Madrid, Spain
[3] Dept. of Biomedical Eng. Mechatronic and Theory of Mechanisms, Wroclaw Univ. of Technology, Poland

***Abstract*—The strain distribution was never studied in spine segments (vertebrae and intervertebral discs) due to its complex geometry and structure. DIC allowed measuring the displacements and strains on the surface of a specimen in a contactless way and providing full-field view. After a validation to estimate the DIC measurement uncertainties, a speckle pattern was prepared on porcine spine segments and then the spines were tested in a loading machine until failure. DIC measured displacement and strain, simultaneously, on the surface of vertebrae and intervertebral discs. Failure strain on vertebrae around 10000 microstrain and on intervertebral discs around 70000 microstrain, proved the measurement reliability and a new way to test spines and increase the present knowledge.**

***Keywords*—Spine, experimental tests, imaging, Digital Image Correlation**

I. Introduction

SPINE is one of the most complex and vital structure in the human skeletal apparatus [1]. Diseases related to spine could involve in pain and immobility, with a series of complications that reduces the life quality [2]. Due to these reasons, knowing the biomechanics of spine is really important in a society that increases the longevity year after year. Until now, the combination of soft tissues (intervertebral discs) and hard tissues (vertebrae), that composes the spine, made impossible the evaluation of displacements and strains under physiological loading conditions with traditional measurement techniques (e.g. strain gauges). In the last years Digital Image Correlation (DIC) changed the scenario of the traditional measurement techniques in biomechanics [3] allowing the computation of displacements, and through differentiation, strains in a contact-less way and providing a full-field view of the examined surface.

This work want to explain a protocol of validation of DIC system, in order to define the measurement uncertainties, and a strain measurements procedure on multi-vertebrae segment, in a contactless way and full-field view, using DIC.

II. Material and methods

A. The validation and optimization of DIC

A commercial 3D-DIC system (Q400, Dantec Dynamics, Denmark), with two 5Mpix cameras and 35mm lens, was used to measure the strain. Before starting to use DIC as a reliable tool, an estimation of the strain uncertainties was performed. A flat aluminium beam was covered with optimized speckle pattern [4] to allow a univocal identification of the surface. Two images of the beam (resolution of 30 μm/pixel) were acquired by the system in a zero-displacement and zero-strain condition (fixed and unloaded). A region-of-interest (ROI) similar to the frontal projection of a three-multi-vertebrae segments was defined on the beam, in order to have the spatial condition as similar as the spine test. A three-parameters factorial design was implemented to investigate the effect of the key parameters of DIC (facet size, grid spacing and filtering on displacement field) on the strain measurements; in terms of systematic and random error, respectively, the average and standard deviation of the measurement point over ROI, and so as to minimize the strain measurement uncertainties.

B. The preparation of specimens

Segments of three/four vertebrae were extracted from porcine lumbar spines. All the soft tissues and spinal processes of external vertebrae were removed with surgical tools and without damage the specimen. In order to create a speckle pattern in the best way possible on soft (intervertebral discs)[5] and hard (vertebrae) tissues the specimens were stained with methylene-blue-saturated water solution for 6 times every 15 minutes, to prepare the dark background. Instead, the white speckle pattern was created through an airbrush airgun [4, 6] using a water-based paint, to minimize interactions, which could damage the bone tissue (Fig. 1). Finally, to enable mechanical testing in loading machine parallel basis were prepared potting external vertebrae in poly-methyl-methacrylate till half of their height.

C. In vitro loading tests

The spine segments were tested in pure axial loading and in isostatic conditions. In order to avoid transmission of any additional load a homemade setup was built using low-friction linear bearings and ball joint. The load was applied through a loading machine in position control, using a monotonic ramp, running at 1mm/s, until failure. Images of specimens under loading were recorded at 6.8 Hz. Using the optimized parameters setup, the displacements and strains were evaluated on the entire frontal surface of the specimens.

III. Results

A. The optimized DIC parameters

The better compromise between measurement uncertainties and spatial resolution was obtained with a facet size of 33 pixels, a grid spacing of 19 pixels and a filter of displacement over a 5x5 data grid. The resultant systematic and random

errors were, respectively, of 10 microstrain and under 100 microstrain. The above-mentioned key parameters will be used for the strain measurement on spine as well, obtaining an equivalent measurement surface for each measurement point, similar to the one of strain gauge.

B. The results of loading tests

Displacement and strain were evaluated on the entire frontal surface of the multi-vertebrae specimen, in both the tissue (intervertebral discs and vertebra) up to failure. The axial strain (Fig. 2) in the vertebrae, prior to failure, was under 10000 microstrain; while in the intervertebral discs, where started the failure, the strain exceeded 70000 microstrain.

IV. DISCUSSION

The evaluation of the measurement uncertainties guaranteed the setting of the best parameters setup and to know the reliability of the measurement tool before starting to use it on complex specimens, such as biological ones. Strains were evaluated on the entire ROI without any loss of information, showing the suitability of the speckle pattern prepared in a non-conventional way [3]. Moreover, no variations, in terms of measurement uncertainties, were reported respect the traditional speckle pattern [4]. The evaluated failure strains were in agreement with the literature [7, 8] but, according to the authors' best knowledge, no-one performed this kind of measures, strain on soft and hard tissue simultaneously, before.

V. CONCLUSION

This study showed the capability of DIC in strain measurement on complex specimens, in term of material properties and geometry, to study and examine in depth the biomechanics of spine. The assertion of these potentialities could open the way to further application of DIC to study the behaviour of human spines.

ACKNOWLEDGEMENT

The authors wish to thank Remo Antelli for donating the porcine spines.

REFERENCES

1. Fung, Y.C., *Bone and cartilage*, in *Biomechanics - Mechanical properties of living tissues*. 1980, Springer Verlag: New York. p. 383-415.
2. Brandolini, N., L. Cristofolini, and M. Viceconti, *Experimental Method for the Biomechanical Investigation of Human Spine: a Review* Journal Of Mechanics in Medicine and Biology, 2014. **14**(01): p. 1430002.
3. Palanca, M., G. Tozzi, and L. Cristofolini, *The Use Of Digital Image Correlation In The BIomechanical Field: A Review.* Inter Biomech, 2016. **3**(1): p. 1-21.
4. Palanca, M., T.M. Brugo, and L. Cristofolini, *Use of Digital Image Correlation to Understand the Biomechanics of the Vertebra.* Journal Of Mechanics in Medicine and Biology, 2015. **15**(2): p. 1540004-1/1540004-10.
5. Lionello, G., C. Sirieix, and M. Baleani, *An effective procedure to create a speckle pattern on biological soft tissue for digital image correlation measurements.* J Mech Behav Biomed Mater, 2014. **39**: p. 1-8.
6. Lionello, G. and L. Cristofolini, *A practical approach to optimizing the preparation of speckle patterns for digital-image correlation.* Measurement Science and Technology, 2014. **25**(10): p. 107001.
7. Bayraktar, H.H., et al., *Comparison of the elastic and yield properties of human femoral trabecular and cortical bone tissue.* J Biomech, 2004. **37**(1): p. 27-35.
8. Spera, D., K. Genovese, and A. Voloshin, *Application of Stereo-Digital Image Correlation to Full-Field 3-D Deformation Measurement of Intervertebral Disc.* Strain, 2011. **47**: p. e572-e587.

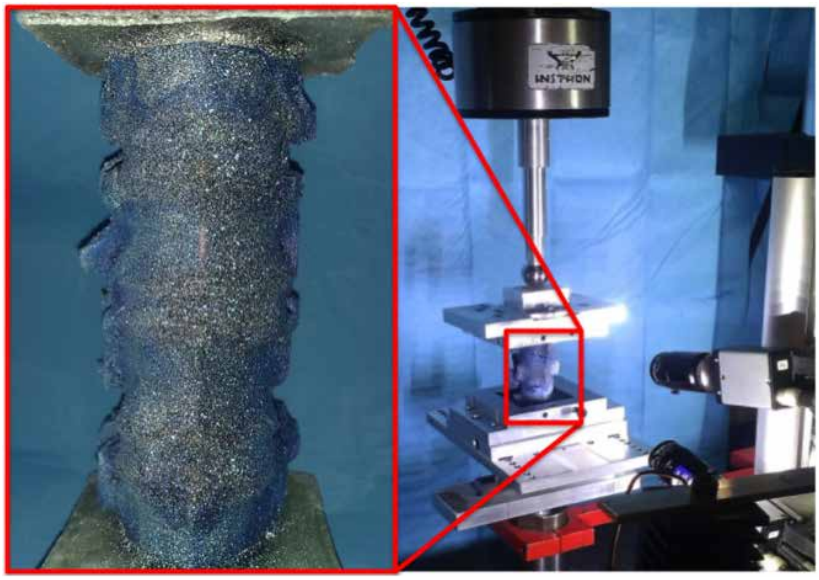

Fig. 1. Left, a three-vertebrae segment spine with white-on-black speckle pattern. Right, overview of the testing setup.

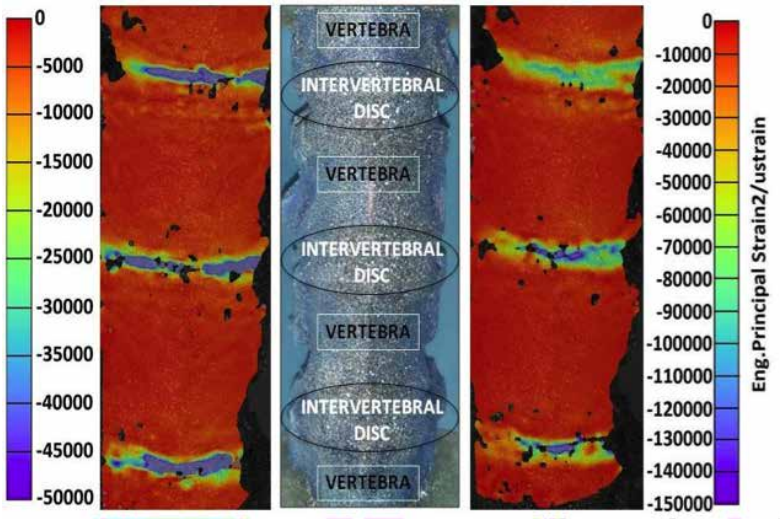

Fig. 2. Axial strain distribution in vertebrae and intervertebral discs. On the left the strain under a load of 1522N and on the right the strain under a load at 3418N, just prior to failure.

Modelling Right Heart Failure in Patients with Pulmonary Hypertension

F. Scardulla[1], P. Mercadante[1], S. Pasta[2,3], D. Bellavia[3] and C. Scardulla[3]
[1] *DICGIM, Universitá di Palermo, Palermo, 90128, Italy*
[2] *Fondazione Ri.MED, Via Bandiera n.11, 90133, Palermo, Italy*
[3] *IRCCS ISMETT, Via Tricomi n.5, 90128, Palermo, Italy*

***Abstract*—Standard of care in precapillary (group I) pulmonary hypertension (PH) includes serial right ventricular (RV) catheterizations in order to monitor RV performance and pulmonary bed pressures, unfortunately with associated costs and side effects related to invasive procedures. Our aim was two-fold: 1) to develop a biventricular finite-element model coupled to a lumped-parameter circulatory system of PH; 2) to assess accuracy of proposed computational model in predicting hemodynamic impairment due to PH and abnormal motion of interventricular septum.**

***Keywords*—finite-element method, lumped-parameter model, pulmonary hypertension.**

I. Introduction

Pulmonary hypertension (PH) is a pathological condition in which the mean pulmonary artery pressure is higher than the normal condition [1]. Specifically, PH is defined when right ventricular (RV) pressure exceeds 25 mmHg at rest [2]. This condition may ultimately lead to right ventricle failure (RVF). Conceptualized hemodynamically, RVF occurs at the point at which cardiac output (CO) and blood pressure drop despite an increased RV end-diastolic pressure (Ref). Although PH can be seen at echocardiography [3], pressure measurements by Swan-Ganz catheterization of right side represent the gold standard for the diagnosis of PH and to assess disease severity [4, 5].

II. Methods

Patient Study Group

We retrospectively identified 10 patients with Group I PH underwent right-sided cardiac catheterization to monitor the progress of pulmonary disease. Standard echocardiography and delayed enhanced (DE) CMR were performed within 2 weeks from RV catheterization in order to collect hemodynamic and morphological data. Specifically, left ventricular (LV), ejection fraction, cardiac output (CO), cardiac index (CI) and pulmonary capillary wedge pressure (PCWP) were collected from standard 2D or Doppler echocardiography. While, RV end-diastolic and end-systolic volume, RV stroke volume, RV cardiac output, RV ejection fraction were measured from DE-CMR.

Lumped-Parameter Modelling of PH

To simulate the hemodynamic impairment due to PH, we used the CircAdapt open-source cardiovascular tool (www.circadapt.org/) as a lumped-parameter model of heart and circulation. The CircAdapt is configured as a network composed of several module types representing myocardial walls, cardiac valves, large blood vessels, and peripheral vasculature to enable real-time simulation of hemodynamic under normal and pathological conditions

Both RV and LV end-diastolic and end-systolic volumes as collected by DE-CMR were used as input parameters in the lumped-parameter model. We interactively adjusted the pulmonary vascular resistance (PVR) and myocardial contractility parameters (i.e. passive stiffness and active contraction) to match both LV and RV ventricular volumes.

For each patient, the model output consisted in the RV and LV pressure-volume loops, which were used as boundary conditions for the biventricular finite-element model. Additionally, standard hemodynamic parameters such as the CO were computed with CircAdapt and then compared to those derived by RV catheterization.

Finite Element (FE) analysis

Numerical simulations were performed according to our previously described biventricular model [6, 7]. The substantial difference with this model was the use of the Holzapfel's constitutive formulation and a thermal-mechanical analog approach to describe active myocardial contraction [8]. This allowed us to avoid numerical issues that are often observed with the Fung's law. LV and RV geometries were obtained *via* parameterized geometric surfaces initialized by morphological measurements collected by DE-CMR. The biventricular model represented the end-systolic ventricular-chamber configuration and then meshed with brick elements in ABAQUS FE code (Simulia, Inc., Providence, RI). Cardiac myofiber angles at epicardium and endocardium were 60° with respect to the circumferential direction of LV wall. We fully constrained the displacement of the ventricular basal line because the mitral valve annulus and aortic valve annulus are much stiffer than the myocardium.

For each patient, RV and LV pressure loading profiles computed with the lumped-parameter simulation of PH were applied to the endocardium using the hydrostatic fluid cavity modeling capabilities of ABAQUS/Standard. Thus, the passive heart behavior was calibrated by iteratively adjusting the material parameters *C* of Holzapfel's law in order to match the measured values of RV and LV end-diastolic volumes. Similarly, the active heart behavior was tuned by scaling the fictitious temperature field. Septal motion was compared to that observed in 4 healthy patients investigated previously [6, 7].

III. Results and Discussion

Linear regression analysis was used to assess associations between catheter- and lumped-derived parameters (see Table 1). Primary dependent (i.e. predicted) variables were CI and PCWP. Hemodynamic parameters predicted by lumped-parameter modeling were comparable to those actually measured in cath-lab ($p<0.05$ for all). Specifically, the lumped-parameter model was able to predict cardiac index with high accuracy (R^2=0.82, p<0.001), although prediction of PCWP was just moderate. It is worthy of consideration that CI is considered as a prognostic indicator to assess the severity of PH [1]. Although a large cohort is needed, the lumped-parameter modeling appears promising to distinguish the less from the most "malignant" PH. Additionally, this tools is based on non-invasive measures as compared to that achieved by catheterization.

TABLE I: Descriptive Statistics of Collected Measurements

Variables	Lumped Model	Outcome: CI (Cath)	Outcome: PCWP (Cath)
Stroke Volume (mL)	54.2±15.2	0.68 (0.01)	0.03 (0.7)
Cardiac Output (Lit./min)	4.1±1.1	0.74 (<0.001)	0.02 (0.72)
Cardiac Index (Lit/min/m^2)	2.4±0.6	0.82 (<0.001)	0.02 (0.72)
RV Systolic Pressure (mmHg)	64.2±12.9	0.01 (0.97)	0.14 (0.36)
Systolic Pulmonary Artery Press. (mmHg)	62.5±12.8	0.01 (0.79)	0.03 (0.71)
Diastolic Pulmonary Artery Pressure (mmHg)	37.1±10.1	0.12 (0.37)	0.52 (0.04)

Numerical simulations revealed that RV experiences severe myocardial stress during cardiac beating (see Figure 1). Specifically, end-systolic myocardial stress was as high as 221 kPa at apex. This pronounced stress is caused by the fact that the RV volumes were markedly high (180.4± 60.1ml) since the increase of intraventricular pressure due to the pulmonary disease leads to an adverse remodeling characterized by ventricular dilatation. Indeed, RV is a compliance chamber that is not able to adequately contrast the high pressure demand. This mechanism ultimately leads to failure of RV chamber. In healthy patients, the mean value of RV end-systolic myocardial stress was 24.3±6 9.7kPa, and this is significantly lower than that shown by patients with PH. Using a similar biventricular finite-element model, Wenk and collaborators [9] found that RV end-systolic myocardial stress in patients with dilated cardiomyopathy was 58.5 kPa, although RV volume was reported as morphologically normal. Similarly, end-diastolic RV myocardial stress in PH was found higher than that showed by healthy patients (150 kPa for PH compared to 13 kPa for normal hearts).

Most importantly the interventricular septum exhibited an abnormal motion throughout cardiac beating. As PH became more severe, the pattern of septal motion was characterized by a normal left-ward shift towards RV during diastolic filling followed by an abnormal right-ward shift towards LV during ejection and isovolumic relaxation phases. This was likely caused by the time courses of simulated ventricular pressures. In simulation of PH, RV pressure exceeded LV pressure during systole, with pressure decay delayed with respect to that of LV. This time course was not observed for healthy patients where interventricular septum did not move over LV. A similar mechanism of abnormal motion for the interventricular septum can be seen clinically in PH [2] and corroborated by Lumens and collaborators [10].

IV. Conclusion

In this study, an approach for modeling the interaction between the heart and the circulatory system was developed by coupling a patient-specific biventricular finite-element model to that of a lumped-parameter that represents the systemic and pulmonic circulatory system. Thus, this approach was adopted to study the mechanism of PH by comparing hemodynamic data to those derived by right side catheterization and by assessing cardiac mechanics. Results showed a good agreement between lumped- and catheter-related hemodynamic measures and the ability of our biventricular model to capture the systolic abnormal motion of interventricular septum observed clinically. This may allow less invasive clinical procedure and rapid computational prediction for the diagnosis of PH. Further studies on large patient cohort are warranted to refine model and confirm results.

Acknowledgement

Mr. F. Scardulla thanks the Italian Ministry of Education, University and Research for supporting his research. The Departments of Radiology at ISMETT have given their support providing clinical cases and offering medical knowledge. This support is gratefully acknowledged.

References

[1] Bourji, K.I. and P.M. Hassoun, *Right ventricle dysfunction in pulmonary hypertension: mechanisms and modes of detection.* Curr Opin Pulm Med, 2015. **21**(5): p. 446-53.

[2] Saggar, R. and O. Sitbon, *Hemodynamics in pulmonary arterial hypertension: current and future perspectives.* Am J Cardiol, 2012. **110**(6 Suppl): p. 9S-15S.

[3] Forfia, P.R. and J.L. Vachiery, *Echocardiography in pulmonary arterial hypertension.* Am J Cardiol, 2012. **110**(6 Suppl): p. 16S-24S.

[4] Kholdani, C.A. and W.H. Fares, *Management of Right Heart Failure in the Intensive Care Unit.* Clin Chest Med, 2015. **36**(3): p. 511-20.

[5] Harjola, V.P., et al., *Contemporary management of acute right ventricular failure: a statement from the Heart Failure Association and the Working Group on Pulmonary Circulation and Right Ventricular Function of the European Society of Cardiology.* Eur J Heart Fail, 2016. **18**(3): p. 226-41.

[6] Scardulla, F., et al., *Mechanics of pericardial effusion: a simulation study.* Proc Inst Mech Eng H, 2015. **229**(3): p. 205-14.

[7] Scardulla, F., et al., *Evaluation of ventricular wall stress and cardiac function in patients with dilated cardiomyopathy.* Proc Inst Mech Eng H, 2016. **230**(1): p. 71-4.

[8] Bagnoli, P., et al., *Computational finite element model of cardiac torsion.* Int J Artif Organs, 2011. **34**(1): p. 44-53.

[9] Wenk, J.F., et al., *A coupled biventricular finite element and lumped-parameter circulatory system model of heart failure.* Comput Methods Biomech Biomed Engin, 2013. **16**(8): p. 807-18.

[10] Lumens, J. and T. Delhaas, *Cardiovascular modeling in pulmonary arterial hypertension: focus on mechanisms and treatment of right heart failure using the CircAdapt model.* Am J Cardiol, 2012. **110**(6 Suppl): p. 39S-48S.

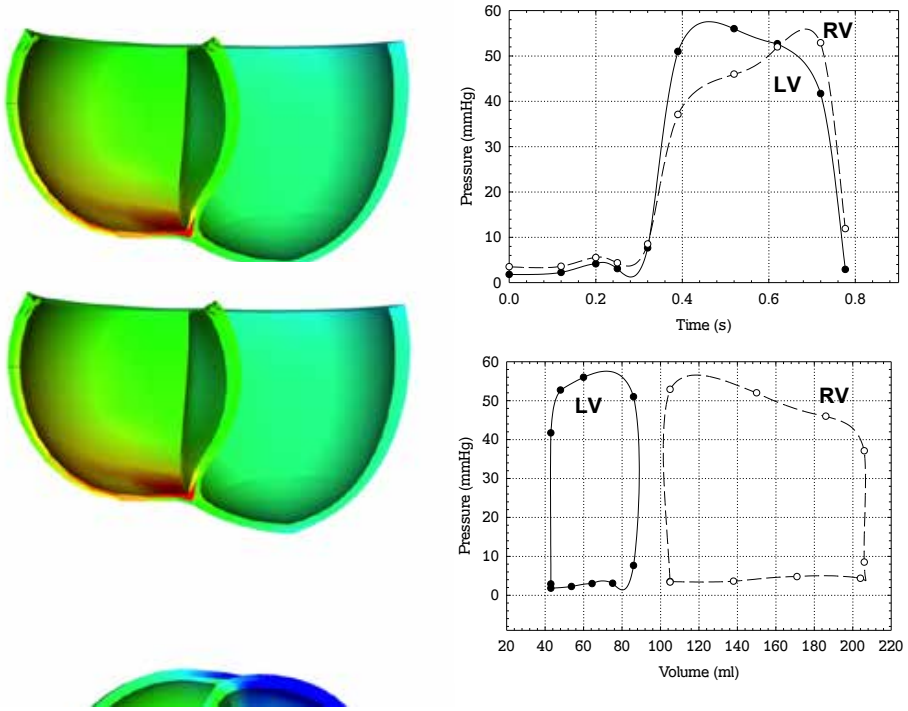

Fig. 1. End-systolic myocardial wall stress showing abnormal motion of interventricular septum (left); pressure-time and pressure-volume loop obtained by the lumped-parameter model (right).

Mechanical characterization of polymeric microspheres through micro-compression testing

G. Serino[1], V. Crognale[2], C. Del Gaudio[2], U. Morbiducci[1], and A. Audenino[1]
[1] *Department of Mechanical and Aerospace Engineering Politecnico di Torino Turin, Italy*
[2] *Department of Enterprise Engineering University of Rome "Tor Vergata"*

***Abstract*— Usage of polymeric microspheres in biomedical applications is dramatically increasing in the last years. Their massive use is promoted by the maturation of methodologies for their preparation, that allow the control of their shape and size. Here we present a study were a test bench is proposed for the characterization of the mechanical properties of polymeric microspheres. In detail, compression tests are performed on three types of gelatine microspheres characterized by three different values of concentration of genipin (0.1%, 0.5%, 1%). Microspheres mechanical properties are evaluated by using nanoindentation and applying the Hertz model, assuming microspheres incompressibility and a Poisson's coefficient equal to 0.5. The values of Young's modulus obtained for the three types of microspheres are 2.56 ±0.95 GPa (0.1% of genipin), 1.87 ±0.91 GPa (0.5% of genipin), and 3.44 ±0.66 GPa (1% of genipin), respectively, confirming that their mechanical behavior depends upon the concentration of the genipin used for their preparation. The obtained results, obtained by applying the Hertz theory, satisfactorily agree with the experimental data, indicating that the Hertz model is adequate to describe the mechanical properties of the investigated microspheres.**

***Keywords*—Nanoindentation, micro-compression, microspheres.**

I. Introduction

POLYMERIC microspheres are largely adopted in biomedical applications as, e.g., embolic agents to treat hyper-vascular tumors [1], or in tissue engineering [2]. The class of polymeric microspheres used for biomedical applications are mainly composed by hydrophilic polymers, because of their biocompatibility. In particular, the injection of gelatin microspheres is very promising, because of their poor antigenic properties and higher absorbability, when compared with other biocompatible polymers as collagen [3].

In this study the mechanical properties of a new design of polymeric microspheres to be used as carriers for local release of drugs and grow factors, are investigated. The rationale of the study is that, since the microspheres have to be injected into the target tissue, the rheological behavior of suspensions or dispersions of such microspheres, and their effectiveness in properly delivering drugs, will depend upon their mechanical properties [3][4]. Technically, nanoindentation is applied on microspheres of size in the range 30-70 μm. To measured load-displacement data, the Hertz model is applied to estimate the Young's modulus. Once fully validated, the protocol here proposed for the mechanical characterization of polymeric microspheres used for drug delivery will allow: (1) to support their design phase and (2) to improve their effectiveness in targeting the release of drugs.

II. Material and methods

The water-in-oil emulsion method was applied to gelatin type A derived from the porcine skin to produce three types of microspheres characterized by a different percentage of genipin (Figure 1), and with an average radius equal to (mean ± SD) 44.12±11.12 μm for group 1, 51.78±10.45 μm for group 2 and 50.88±9.30 μm for group 3. Genipin in three different values of concentration (w/v) %: 0.1% (group 1) ,0.5% (group 2), and 1% (group 3), was used as natural cross-linker (the presence of genipin affects the structural characteristics of the polymer and the degradation kinetics as well).

Nanoindentation combined with the Hertz model was applied to estimate the mechanical properties of the microspheres. In nanoindentation, when the contact between the specimen and the indenter tip is detected, its displacement is measured as the load is applied. From the measured load-displacement curve (Figure 2) it is possible the estimation of the Young's modulus of the specimen.

In detail, the Nanoindenter XP (Agilent/MTS company), characterized by a theoretical force resolution of 50 nN and a theoretical displacement resolution lower than 0.01 nm, was adopted and a specific protocol was developed for characterize the microspheres through a micro-compression test. In detail, here a flat end punch with a diameter of 500 μm was selected for indentation. The compression test is characterized by three steps: loading, hold and unloading. During the loading and unloading phases the velocity of the indenter punch was set at a constant value of 10 nm s^{-1}. The hold phase consisted of a stabilization period along which the maximum value of the load was maintained for a period of 5 s. The maximum value of the load was obtained in correspondence of an indentation depth equal to the 5% of the initial radius of the microsphere. The initial radius of each microsphere was evaluated before the beginning of the test, using the optical system embedded in the Nanoindenter XP. Load and displacement signals were acquired at a sampling rate of 5 Hz.

On measured load-displacement curves as obtained from the compression tests, the Hertz model [5] was applied and the Young's modulus was estimated according to:

$$F = \frac{4\sqrt{R}}{3}\frac{E}{1-\upsilon^2}\sqrt{\left(\frac{H}{2}\right)^3} = \frac{4\sqrt{R}}{3}E^*\sqrt{\left(\frac{H}{2}\right)^3} \quad (1)$$

where F is the load, H is the displacement, E is the Young's modulus, υ is the Poisson's ratio and R is the radius of the microsphere. The value of the Poisson's ratio was assumed to be equal to 0.5 [2][6]. The linear least squares method has been applied to estimate the value of E on the experimental data. By applying the Hertz contact model we implicitly

made the assumptions that: (1) microspheres are spherically shaped; (2) deformation is symmetric; (3) microspheres are made of a purely elastic and isotropic polymer; (4) only small deformations affect indented microspheres.

III. Results

Typical compression load-displacement curves as obtained from nanoindentation are presented in Figure 2. The curves is characterized by an hysteresis loop typically characterizing viscous-elastic materials.

For each group of polymeric microsphere 40 tests were carried out. Outliers have been excluded by applying the modified Thompson's Tau method.

The Young's modulus was estimated by using the Hertz contact model, applied to the linearized experimental data measured along the loading phase. We obtained three average values of Young's modulus equal to 2.56 ±0.95 GPa, 1.87 ±0.91 GPa, and 3.44 ±0.66 GPa (mean ± SD) for group 1, 2 and 3 respectively.

The percentage of genipin influences the mechanical properties of the microspheres. Indeed the analysis of variance (ANOVA) applied to the tests carried out on microspheres shows a correlation ($p<0.05$) between their mechanical properties and the percentage of genipin used during the production of the microspheres. The progressive increase in the percentage of genipin in microspheres composition is not related to a linear increase of the Young's modulus. Load-displacement curves obtained for microspheres belonging to group 1 show a mean peak load value higher than group 2 (Figure 3), indeed the experimental curves obtained for the group 1 are characterized by an higher slope respect the curve belonging to group 2.

Since the level of (imposed) deformation is the same in all the experiments, the estimated Young's Modulus of microspheres of group 2 is lower than group 1.

Individual Young's modulus from single microspheres were used as input variable in the Hertz model and theoretical results were compared with experimental data relative to the sole loading phase of the curve. The explanatory results displayed in **Errore. L'origine riferimento non è stata trovata.** are representative of all the nanoindentation tests performed on single microspheres and indicate that there is a satisfactory agreement between the Hertz model for contact and the experimental data.

IV. Discussion

Application of polymeric microspheres in medicine has increased in the past years thanks to the development of novel methods for their preparation that allow a fine control of their size and shape. The degradation rate of the gelatin microspheres, that regulates the rate of drug delivery, depends strongly on their mechanical properties. Usually, this kind of microspheres are injected in the target tissues by using a solution or an appropriate gel in which they are in suspension. The rheological property of such suspensions of microspheres are affected by the mechanical properties of these microspheres. Hence, from the characterization of the mechanical behavior of polymeric microspheres it is possible to obtain knowledge which is fundamental for improving microspheres design and, ultimately, drug delivery.

As for the analysis here presented, for the three preparations of microspheres the average values of the standard error (and of R^2) with respect to the load-displacement curves estimated by applying the Hertz contact model are equal to 1.55 mN (R^2= 0.98), 1.59 mN (R^2= 0.99), and 2.10 mN (R^2= 0.99) , for group 1 group 2 and group 3, respectively. These data confirm that the selected Hertz model satisfactorily fits the experimental data as obtained from the application of a nanoindentation strategy, making the estimated mechanical properties reliable.

The estimation of a Young's modulus value for microspheres belonging to group 2 lower than group 1 can be explained in terms of the procedure applied for microspheres fabrication. Since it is expected an higher value for the Young's modulus, by increasing the percentage of genipin in fabricated microspheres, the counter-intuitive here presented results could be ascribed to fabrication parameters setting which could influence the ultimate mechanical features of microspheres. In particular, two of this parameters could markedly influence the crosslinking phase of the fabrication process, i.e., the stirring speed and the crosslinking time, because they determine size distribution, independent and individual growth of the microspheres, and the degree of crosslinking. We conjecture that the setting adopted for these parameters in the fabrication of microspheres belonging to group 2 has lead to an impairment of the mechanical properties for this group, also in the presence of an higher percentage of genipin, with respect to group 1. Several limitations could weaken the findings of this study. In particular, the defined deformation at 5% of the initial diameter, which limits the validity of these results only for small deformation. Moreover, nanoindentation tests were carried out in dry condition, while the physiological environment is an aqueous environment. Further analysis is needed to clarify if dry tests can be representative of the in vivo behavior of the microspheres.

In conclusion, the preliminary findings presented here confirm the potential (1) of using nanoindentation and (2) of applying the Hertz model for a mechanical characterization of gelatin microspheres. The presented approach could be easily extended to characterize the mechanical behavior of microspheres obtained using, e.g., chitosan, or blends of gelatin and chitosan.

References

[1] K. Hidaka,M. Nakamura, K. Osuga, H. Miyazaki, S. Wada, "Elastic cherecteristics of microspherical embolicagents used for vascular interventional radiology", *J of the Mechanical Behavior of Biomedical Materials,* 3:497-503, 2010.

[2] C. X. Wang, C. Cowen, Z.Zhang, C.R. Thomas, "High-speed compression of single alginate microspheres", *Chimical Engineering Science*, 60:6649-6657, 2005.

[3] W.J.E.M. Habraken, L.T. de Jonge, J.G.C. Wolke, L. Yubao, A.G. Mikos, J.A. Jansen, "Introduction of gelatin microspheres into an injectable calcium phosphate cement", *J Biomed Mater Res,* 87A:643-655, 2008.

[4] Y. Yan, Z. Zhan, J.R. Stokes, Q. Zhou, G. Ma, et al, "Mechanical characterization of agarose micro-particles with a narrow size distribution" *Powder Technology,* 192:122-130, 2009.

[5] H. Hertz, *On the contact of elastic solids,* 318, 1896.

[6] K Hidaka, L.Moine, G.Collin,D. Labare, J.L. Grossiord, et al,"Elasticity and viscoelasticity of embolization microspheres", *J of the Mechanical Behavior of Biomedical Materials,* 4:2161-2167, 2011.

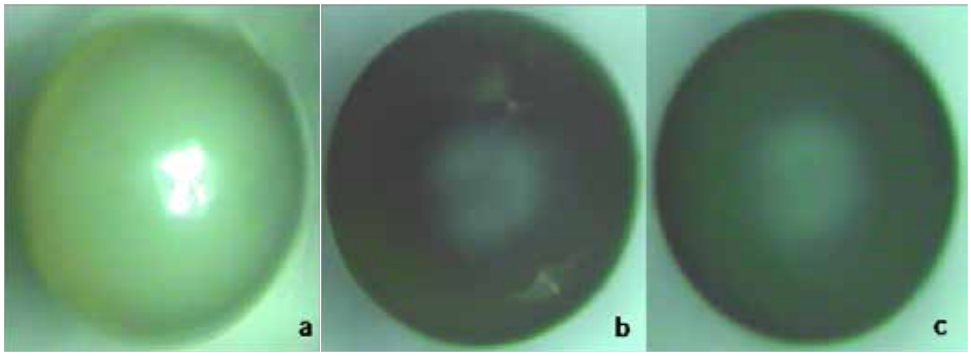

Figure 1: Representative images of group 1 (a) group 2 (b) and group 3 (c), taken by the optical microscope built in the Nanoindenter XP. (Resolution: 0.2 µm/pixel).

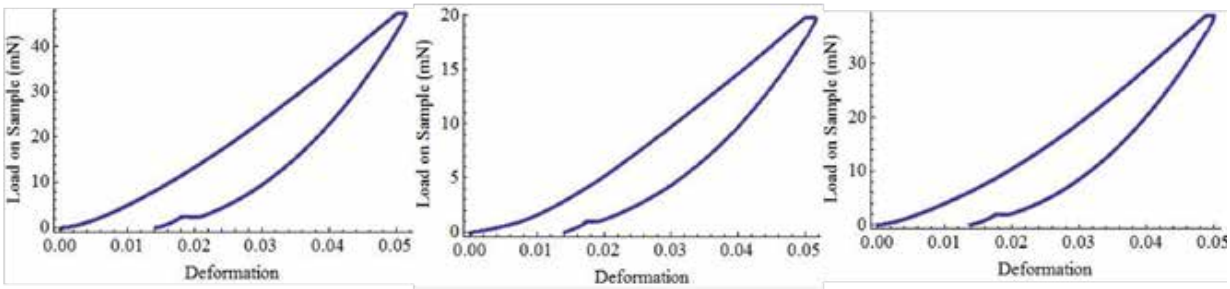

Figure 2: Typical Load-Displacement curve as obtained from nanoindentation tests on gel microspheres of group 1 (a), group 2 (b) and group 3 (c).

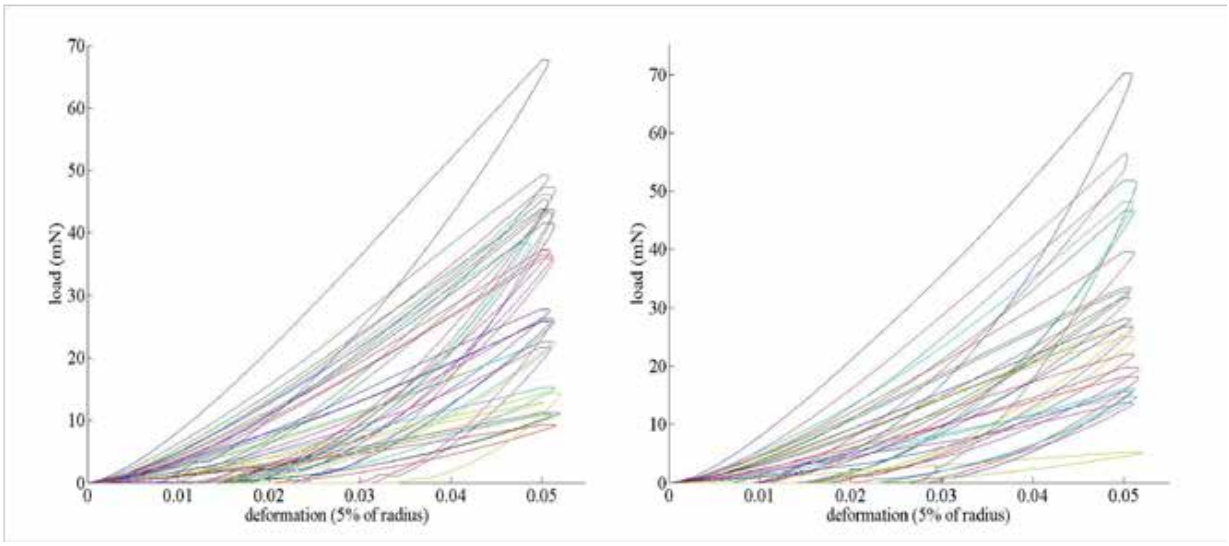

Figure 3: Experimental curves obtained by the microindentation tests. On the left curves obtained for microspheres with 0.1% of genipin. On the right curves obtained for microspheres with 0.5% of genipin

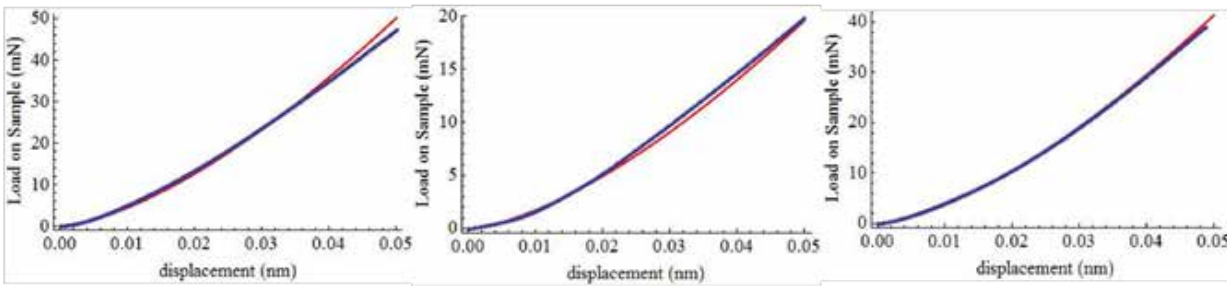

Figure 4: Comparison of the loading phase as obtained from the experimental data (blue curve) and from the Hertz model (red curve), for group 1 (a), group 2 (b), group 3 (c).

Titanium craniofacial prostheses manufacturing using non-conventional forming processes

T. Villa[1], M. V. Caruso[2,3], G. Ambrogio[2], L. De Napoli[2], L. La Barbera[1], G. Palumbo[4], D. Sorgente[4], A. Piccininni[4], P. Guglielmi[4], G. Fragomeni[3]

[1] *Department of Chemistry, Materials and Chemical Engineering, Politecnico di Milano*
[2] *Department of Mechanical, Energetic and Management Engineering (DIMEG), University of Calabria*
[3] *Department of Medical and Surgical Science, University of Catanzaro*
[4] *Department of Mechianics, Mathematics and Management (DMMM), Politecnico di Bari*

***Abstract*—In particular situations, such as in presence of congenital malformations, pathologies or traumas, skull can present bone defects or empties, which can be characterized by complex geometries that vary from case to case. For repairing these defects/empties, patients must undergo cranioplasty procedures, during which a proper prosthesis is anchored to the skull, replacing the missing bone parts. Nowadays, starting from diagnostic images, patient-specific prostheses can be manufactured, made of biocompatible materials. Among metallic materials, titanium alloys are the most suitable for this application.**

The aim of this study is to present a methodology to manufacture craniofacial prostheses in titanium alloy using non-conventional forming processes. In details, the complete procedure starts from the design of both the prosthesis and the anchoring system, choosing the optimal material and the best manufacturing process according to the geometry of the defect, the available time and the cost.

In order to demonstrate the potency of this approach, two case studies were reported.

***Keywords*—craniofacial titanium prostheses, non-conventional forming processes, realization procedure.**

I. Introduction

THE skull is one of the most complex bones and it plays a key role because it protects the brain, the organ that makes us human, and has a strong aesthetic impact [1]. So, it sums both functional and aesthetic aspects. Unfortunately, because of congenital malformations, pathologies or traumas, the skull can present defects or empties, which are repaired with cranioplasty interventions [2]. In particular, during this surgical procedure, a prosthesis made with biocompatible material [2], such as titanium and its alloys [1],[3], is anchored to the skull. Moreover, titanium is chosen as it has excellent mechanical properties [3] and favours osseointegration with the host bone [4].

In order to fulfil the evident aesthetic requirements, such prostheses must be patient customized. In particular, these prostheses can be manufactured using computer-aided-design/computer-aided manufacturing (CAD/CAM) technique [5]: CAD/CAM titanium implants show the lowest rate of complications and have reasonable costs [6]. Regarding the manufacturing different processes, such as the milling [7] or the additive manufacturing [8], can be used even if the optimal one has not yet been established.

The aim of this study was to present a complete procedure for the manufacturing of such titanium prostheses based on the use of non-conventional forming processes.

II. Procedure

The necessary steps to manufacture craniofacial prostheses in titanium by means of the non-conventional processes are illustrated in Figure 1 and described below.

A. Medical scan and DICOM images

Thanks to the research and technological development in imagining techniques, nowadays morphological aspects can be evaluated by means of the computer tomography (CT) and magnetic resonance imaging (MRI), which provide 2D multiplanar images or slices in the DICOM format [9]. So, a 3D visualization is available.

B. Virtual modelling

Starting from diagnostic images of the defected skull, a virtual model can be obtained by means the segmentation process, using different software [10]. For this work, the open source software Invesalius was chosen for the 3D/volumetric reconstruction [11]. Since it provides a STL file, in order to obtain a 3D solid model of skull bone, reverse engineering [12] was used. After that, the prosthesis was designed considering the defect morphology and trying to get an appearance of the resulting treated skull as close as possible to a normal one.

C. Design of anchoring system

In case of titanium customized craniofacial prostheses made with forming processes, they have a greater area and a larger perimeter with respect to the defect [13], but no information regarding the overlap length is available. Furthermore, titanium and skull bone have different elastic modules, reported in [14] and [15] respectively. For these two reasons, a detailed design of the anchoring system is necessary.

To realize it, a hybrid approach was developed (Figure 2). In details, an optimization procedure, based on the ANOVA analysis and the response surface methodology -RSM- [16], was implemented in order to identify the optimal values for the overlap length and the screw shank diameter for a specific defect area, considering the worst accidental compressive load. In this case, the bone that adheres to the prosthesis must resist, so the maximum stress must be evaluated to establish the best anchoring system. Different simulations were carried out using finite-element modeling (FEM) and considering five factors (screw shank diameter, overlap length, load

intensity and its tilt angle and the damaged area) and their values range. Moreover, the stress numerical results were used as input data for the optimization process. Regarding the FEM analyses, they were carried out using Comsol Multiphysics 5.2 (COMSOL Inc, Stockholm, Sweden), whereas for the optimization procedure, Design Expert Software (Stat-Ease, Inc., Minneapolis, USA - trial version) was used.

D. Prosthesis manufacturing

As reported before, in this study non-conventional forming processes were considered to manufacture the prostheses. In details, superplastic forming (SPF) and single-point incremental forming (SPIF) were chosen.

In case of SPF, a sheet is deformed with high temperatures under the action of an in-pressure inert gas, instead, during the SPIF, a rotating tool/punch deforms the sheet with high speeds. Both processes used the CAD/CAM approach, employing an electro-hydraulic machine in the SPF and a 3axis CNC machine in the SPIF. A sketch of the two methodologies are reported in Figure 3. Both technologies allow to create prostheses with very low thicknesses and high mechanical strength. Furthermore, the advantage of SPF is that it can be used to obtain prostheses with complex geometry, whereas the benefit of the SPIF is that prostheses can be made in low times, without employ moulds.

E. Biocompatibility check

The most important property of the bone substitutive materials is the biocompatibility. Even if the titanium alloys normally show this feature, the manufacturing process could have been altered this property, and, consequently, biocompatibility of the final prosthesis must be verified through citotoxicity tests.

III. VALIDATION

To demonstrate the procedure feasibility and to validate it, two different defects were considered and the relative prostheses were made applying the methodology (Figure 4).

In details, the prosthesis relative to the frontal damage was made with the SPF because of the complex geometry, whereas the prosthesis relative to the lateral defect was realized using the SPIF in order to obtain it in very low times. Regarding the SPF manufacturing, the undeformed sheet was heated up to 850°C and then subjected to argon in pressure. Instead, in the SPIF, a hemispheric punch (diameter of 15 mm) deformed the sheet with a continuous movement (constant tool depth step of 0.1 mm and a tool feed rate of about 2000 mm/min), following the trajectory generated by the CAD/CAM program. Nano-indentation tests were also performed in order to measure hardness and elastic modulus variation deriving from the manufacturing process. Results highlighted that no significant changes are generated by the processes. The two realized prostheses are reported in Fig. 4.

IV. CONCLUSION

This work presented a procedure to realize craniofacial prostheses in titanium with non-conventional forming processes, the superplastic forming and the single-point incremental forming. Both these two technologies have proved to be suitable for this application, with the advantage of obtaining both extremely thin and, at the same time, resistant prostheses. The necessary aesthetic and biocompatibility requirements have also been demonstrated that can be fulfilled by the usage of the two technologies.

ACKNOWLEDGEMENT

This research is funded by the Italian Ministry of University and Research within the project PRIN "Bioforming".

REFERENCES

[1] M. C. Goiato, R. B.Anchieta,, M. S. Pita, D. M. dos Santos, "Reconstruction of skull defects: currently available materials", *Journal of Craniofacial Surgery*, vol. 20(5), pp.1512-1518, 2009.

[2] P. Solaro, E. Pierangeli, C. Pizzoni, P. Boffi and G. Scalese, "From computerized tomography data processing to rapid manufacturing of custom-made prostheses for cranioplasty", *Journal of neurosurgical sciences*, vol. 52(4), pp.113, 2008.

[3] M. A. H Gepreel, M. Niinomi, "Biocompatibility of Ti-alloys for long-term implantation", *Journal of the mechanical behavior of biomedical materials*, vol. 20, pp. 407-415, 2013.

[4] T. Albrektsson, P. I., Brånemark, H. A. Hansson, J. Lindström, "Osseointegrated titanium implants: requirements for ensuring a long-lasting, direct bone-to-implant anchorage in man", *Acta Orthopaedica*, vol. 52(2), pp. 155-170, 1981.

[5] L. C. Hieu, E. Bohez, J. Vander Sloten, H. N.Phien, E.Vatcharaporn, P. H Binh, ... P. Oris, "Design for medical rapid prototyping of cranioplasty implants", *Rapid Prototyping Journal*, vol. 9(3), pp.175-186, 2003.

[6] M. Cabraja, M. Klein, T. N Lehmann, "Long-term results following titanium cranioplasty of large skull defects", *Neurosurgical focus*, vol. 26(6), pp. E10, June 2009.

[7] M.Wehmöller, S.Weihe, C. Rasche, P. Scherer, H. Eufinger, "CAD/CAM-prefabricated titanium implants for large skull defects-clinical experience with 166 patients from 1994 to 2000", In *International Congress Series*, vol. 1268, pp. 667-672, June 2004.

[8] A. L. Jardini, M. A. Larosa, C. A. de Carvalho Zavaglia, L. F. Bernardes, C. S. Lambert, P. Kharmandayan ... R. Maciel Filho, "Customised titanium implant fabricated in additive manufacturing for craniomaxillofacial surgery: This paper discusses the design and fabrication of a metallic implant for the reconstruction of a large cranial defect", *Virtual and Physical Prototyping*, vol. 9(2), pp. 115-125, 2014.

[9] P. Mildenberger, M. Eichelberg, E. Martin, "Introduction to the DICOM standard", *European radiology*, vol. 12(4), pp. 920-927, 2002

[10] G. L. Presti, M. Carbone, D. Ciriaci, D. Aramini, M. Ferrari, V. Ferrari, "Assessment of DICOM viewers capable of loading patient-specific 3D models obtained by different segmentation platforms in the operating room", *Journal of digital imaging*, vol. 28(5), pp. 518-527, 2015

[11] T.F. de Moraes, P.H. Amorim, F.S. Azevedo, J.V. da Silva, "InVesalius-An open-source imaging application. Computational Vision and Medical Image Processing", in *VipIMAGE 2011*, vol. 405. 2011.

[12] E. Maravelakis, K. David, A. Antoniadis, A. Manios, N. Bilalis, Y. Papaharilaou, "Reverse engineering techniques for cranioplasty: a case study", *Journal of medical engineering & technology*, vol. 32(2), pp. 115-121, 2008

[13] B. Lu, D.K. Xu, R.Z Liu., H. Ou, H. Long, J. Chen, "Cranial reconstruction using double side incremental forming". *Key Engineering Materials*, vol. 639, pp. 535-542, 2015.

[14] M. Vosough, F. Schultheiss, M. Agmell, J.E. Stahl,"A method for identification of geometrical tool changes during machining of titanium alloy Ti6Al4V", *The International Journal of Advanced Manufacturing Technology*, vol. 67(1-4), pp. 339-348, 2013

[15] J.S. Raul, D. Baumgartner, R. Willinger, B. Ludes, "Finite element modelling of human head injuries caused by a fall". *International Journal of Legal Medicine*, vol. 120(4), pp. 212-218, 2006.

[16] İ. Asiltürk, S. Neşeli, M. A. İnce, "Optimisation of parameters affecting surface roughness of Co28Cr6Mo medical material during CNC lathe machining by using the Taguchi and RSM methods". *Measurement*, vol. 78, pp. 120-128, 2016

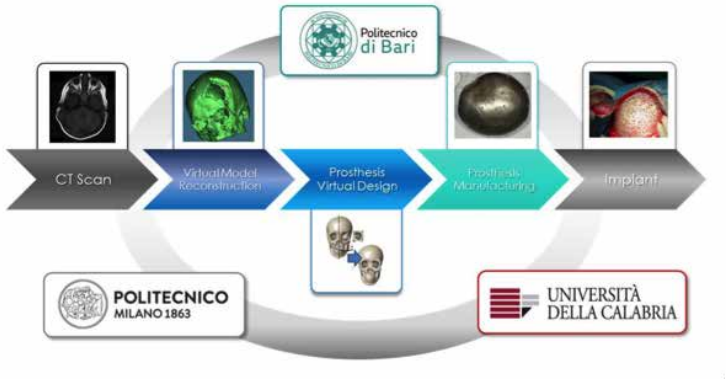

Fig. 1. Steps of presented procedure for the realization of craniofacial prostheses in titanium by means of non-conventional processes

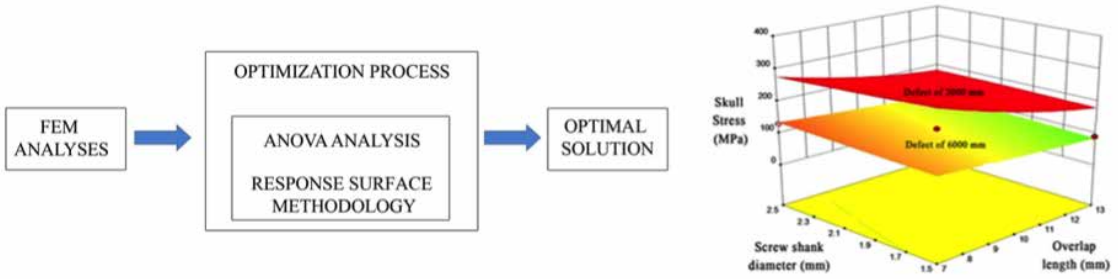

Fig. 2. Steps of the procedure used to design the optimal anchoring system (left) and results of the optimization of (right)

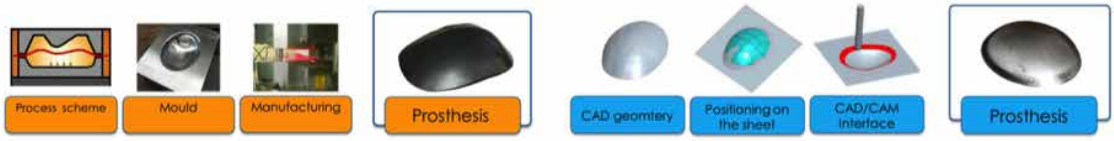

Fig. 3. Non-conventional forming procedures: superplastic forming (SPF, left) and single-point incremental forming (SPIF, right)

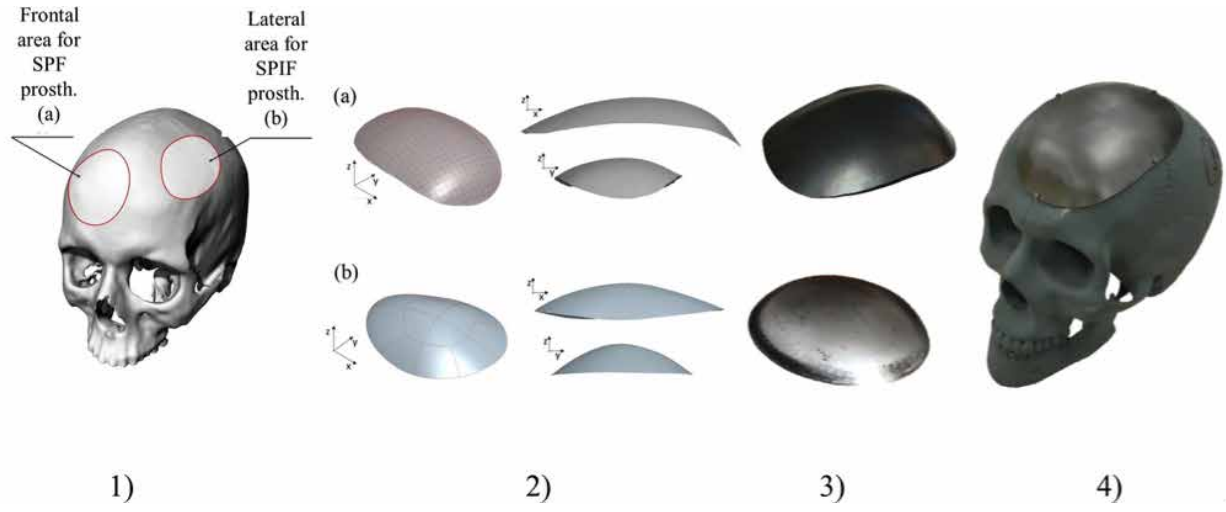

Fig. 4. (1) Skull defects areas (2) relative CAD models of the prostheses (3) manufactured prostheses (4) SPF prosthesis mounted on the skull model